

REPORT DOCUMENTATION PAGE				Form Approved OMB NO. 0704-0188	
<p>The public reporting burden for this collection of information is estimated to average 1 hour per response, including the time for reviewing instructions, searching existing data sources, gathering and maintaining the data needed, and completing and reviewing the collection of information. Send comments regarding this burden estimate or any other aspect of this collection of information, including suggestions for reducing this burden, to Washington Headquarters Services, Directorate for Information Operations and Reports, 1215 Jefferson Davis Highway, Suite 1204, Arlington VA, 22202-4302. Respondents should be aware that notwithstanding any other provision of law, no person shall be subject to any penalty for failing to comply with a collection of information if it does not display a currently valid OMB control number.</p> <p>PLEASE DO NOT RETURN YOUR FORM TO THE ABOVE ADDRESS.</p>					
1. REPORT DATE (DD-MM-YYYY) 18-08-2013		2. REPORT TYPE Final Report		3. DATES COVERED (From - To) 15-May-2010 - 14-May-2013	
4. TITLE AND SUBTITLE SOOT FORMATION AND DESTRUCTION IN HIGH-PRESSURE FLAMES WITH REAL FUELS				5a. CONTRACT NUMBER W911NF-10-1-0118	
				5b. GRANT NUMBER	
				5c. PROGRAM ELEMENT NUMBER 611102	
6. AUTHORS William L. Roberts, Tiegang Fang				5d. PROJECT NUMBER	
				5e. TASK NUMBER	
				5f. WORK UNIT NUMBER	
7. PERFORMING ORGANIZATION NAMES AND ADDRESSES North Carolina State University Research Administration 2701 Sullivan Drive, Suite 240 Raleigh, NC 27695 -7514				8. PERFORMING ORGANIZATION REPORT NUMBER	
9. SPONSORING/MONITORING AGENCY NAME(S) AND ADDRESS(ES) U.S. Army Research Office P.O. Box 12211 Research Triangle Park, NC 27709-2211				10. SPONSOR/MONITOR'S ACRONYM(S) ARO	
				11. SPONSOR/MONITOR'S REPORT NUMBER(S) 57461-EG.11	
12. DISTRIBUTION AVAILABILITY STATEMENT Approved for Public Release; Distribution Unlimited					
13. SUPPLEMENTARY NOTES The views, opinions and/or findings contained in this report are those of the author(s) and should not be construed as an official Department of the Army position, policy or decision, unless so designated by other documentation.					
14. ABSTRACT The overall objective of this project was to increase the understanding of the effects of pressure on soot formation and destruction in laminar diffusion flames burning both simple hydrocarbon and complex real fuels. A more complete understanding of the soot formation processes at elevated pressure (e.g., 30 atm) will enable the design of more efficient diesel engines. Higher efficiency will help reduce the logistical demand transportation fuels place on the entire DoD and thus increase the 'tooth to tail' ratio, enhancing force sustainability. By reducing soot					
15. SUBJECT TERMS Soot process, soot formation, soot oxidation, laminar diffusion flame, high pressure					
16. SECURITY CLASSIFICATION OF:			17. LIMITATION OF ABSTRACT UU	15. NUMBER OF PAGES	19a. NAME OF RESPONSIBLE PERSON William Roberts
a. REPORT UU	b. ABSTRACT UU	c. THIS PAGE UU			19b. TELEPHONE NUMBER 919-515-5294

Report Title

SOOT FORMATION AND DESTRUCTION IN HIGH-PRESSURE FLAMES WITH REAL FUELS

ABSTRACT

The overall objective of this project was to increase the understanding of the effects of pressure on soot formation and destruction in laminar diffusion flames burning both simple hydrocarbon and complex real fuels. A more complete understanding of the soot formation processes at elevated pressure (e.g., 30 atm) will enable the design of more efficient diesel engines. Higher efficiency will help reduce the logistical demand transportation fuels place on the entire DoD and thus increase the 'tooth to tail' ratio, enhancing force sustainability. By reducing soot emissions, survivability of assets will be increased by reducing the vehicle's IR signature. First, experiments were conducted for ethylene flames with different diluents. Quantification of hydrocarbon species was done by extraction of samples using a quartz micro probe along the centerline of the flame and analyzing them using both a GC-MS/FID and a TCD to calculate the mole fraction of the various species in the sample volume. The flame temperature was measured by both thermocouples and two-color pyrometry. Soot volume fraction, primary particle size, and number density were also measured by line of sight attenuation. The pressure effects on the measured quantities are investigated. Second, laminar flames of pre-vaporized liquid fuels are being measured with the aid of a custom built electrospray vaporizer.

Enter List of papers submitted or published that acknowledge ARO support from the start of the project to the date of this printing. List the papers, including journal references, in the following categories:

(a) Papers published in peer-reviewed journals (N/A for none)

<u>Received</u>	<u>Paper</u>
07/31/2013	4.00 Ranjith Kumar Abhinavam Kailasanathan, Tiffany L.B. Yelverton, Tiegang Fang, William L. Roberts. Effect of diluents on soot precursor formation and temperature in ethylene laminar diffusion flames, Combustion and Flame, (03 2013): 0. doi: 10.1016/j.combustflame.2012.11.004
07/31/2013	5.00 Ranjith Kumar Abhinavam Kailasanathan, Emily K. Book, Tiegang Fang, William L. Roberts. Hydrocarbon species concentrations in nitrogen diluted ethylene-air laminar jet diffusion flames at elevated pressures, Proceedings of the Combustion Institute, (01 2013): 0. doi: 10.1016/j.proci.2012.06.148
TOTAL:	2

Number of Papers published in peer-reviewed journals:

(b) Papers published in non-peer-reviewed journals (N/A for none)

<u>Received</u>	<u>Paper</u>
-----------------	--------------

TOTAL:

Number of Papers published in non peer-reviewed journals:

(c) Presentations

Number of Presentations: 0.00

Non Peer-Reviewed Conference Proceeding publications (other than abstracts):

Received Paper

TOTAL:

Number of Non Peer-Reviewed Conference Proceeding publications (other than abstracts):

Peer-Reviewed Conference Proceeding publications (other than abstracts):

Received Paper

07/31/2013	6.00	Scott A. Steinmetz, Tiegang Fang, William L. Roberts. Soot Measurements in Diluted High Pressure Laminar Ethylene Co-flow Flames, 9th Asia-Pacific Conference on Combustion. 2013/05/19 00:00:00, . : ,
07/31/2013	7.00	Tiegang Fang, William L. Roberts, Scott A. Steinmetz. Soot Measurements in High Pressure Diffusion Flames, European Combustion Meeting 2013. 2013/06/25 00:00:00, . : ,
07/31/2013	8.00	Wei Jing, William L. Roberts, Tiegang Fang. Effects of Temperature and Oxygen on Spray and Combustion Characteristics of Diesel and Jet-A in a Constant Volume Combustion Vessel, ILASS Americas, 25th Annual Conference on Liquid Atomization and Spray Systems. 2013/05/05 00:00:00, . : ,

TOTAL: 3

Number of Peer-Reviewed Conference Proceeding publications (other than abstracts):

(d) Manuscripts

Received Paper

07/15/2012	1.00	Ranjith Kumar Abhinavam Kailasanathan, Emily K. Book, Tiegang Fang, William L. Roberts. HYDROCARBON SPECIES CONCENTRATIONS IN NITROGEN DILUTED ETHYLENE-AIR LAMINAR JET DIFFUSION FLAMES AT ELEVATED PRESSURES, Proceedings of the Combustion Institute (01 2012)
07/15/2012	2.00	Ranjith Kumar Abhinavam Kailasanathan, Tiffany L.B. Yelverton, Tiegang Fang, William L. Roberts. Effect of Diluents on Soot Precursor Formation and Temperature at Elevated Pressures in Laminar Diffusion Flames, Combustion and Flame (07 2012)
07/31/2013	9.00	Wei Jing, William L. Roberts, Tiegang Fang. Effects of Ambient Temperature and Oxygen Concentration on Diesel Spray Combustion Using a Single-Nozzle Injector in a Constant Volume Combustion Chamber, Combustion Science and Technology (05 2013)
07/31/2013	10.00	Ranjith Kumar Abhinavam Kailasanathan, Ji Zhang, Tiegang Fang, William L. Roberts. Effects of diluents on soot surface temperatures and soot volume fractions in diluted ethylene diffusion flames, Combustion Science and Technology (02 2013)
TOTAL:	4	

Number of Manuscripts:

Books

Received Paper

TOTAL:

Patents Submitted

Patents Awarded

Awards

Graduate Students

<u>NAME</u>	<u>PERCENT SUPPORTED</u>	Discipline
Ranjith Kumar Abhinavam Kailasanath	1.00	
Emily Book	0.20	
Wei Jing	0.50	
FTE Equivalent:	1.70	
Total Number:	3	

Names of Post Doctorates

<u>NAME</u>	<u>PERCENT SUPPORTED</u>
FTE Equivalent:	
Total Number:	

Names of Faculty Supported

<u>NAME</u>	<u>PERCENT SUPPORTED</u>	National Academy Member
William L. Roberts	0.02	
Tiegang Fang	0.13	
FTE Equivalent:	0.15	
Total Number:	2	

Names of Under Graduate students supported

<u>NAME</u>	<u>PERCENT SUPPORTED</u>
FTE Equivalent:	
Total Number:	

Student Metrics

This section only applies to graduating undergraduates supported by this agreement in this reporting period

- The number of undergraduates funded by this agreement who graduated during this period: 0.00
- The number of undergraduates funded by this agreement who graduated during this period with a degree in science, mathematics, engineering, or technology fields:..... 0.00
- The number of undergraduates funded by your agreement who graduated during this period and will continue to pursue a graduate or Ph.D. degree in science, mathematics, engineering, or technology fields:..... 0.00
- Number of graduating undergraduates who achieved a 3.5 GPA to 4.0 (4.0 max scale):..... 0.00
- Number of graduating undergraduates funded by a DoD funded Center of Excellence grant for Education, Research and Engineering:..... 0.00
- The number of undergraduates funded by your agreement who graduated during this period and intend to work for the Department of Defense 0.00
- The number of undergraduates funded by your agreement who graduated during this period and will receive scholarships or fellowships for further studies in science, mathematics, engineering or technology fields:..... 0.00

Names of Personnel receiving masters degrees

<u>NAME</u>
Total Number:

Names of personnel receiving PhDs

NAME

Ranjith Kumar Abhinavam Kailasanathan

Total Number:

1

Names of other research staff

NAME

PERCENT SUPPORTED

FTE Equivalent:

Total Number:

Sub Contractors (DD882)

Inventions (DD882)

Scientific Progress

See Attachment

Technology Transfer

SOOT FORMATION AND DESTRUCTION IN HIGH-PRESSURE FLAMES WITH REAL FUELS

Final Report

Project period: 15 MAY 10 – 14 MAY 13

PIs: William Roberts and Tiegang Fang,

Dept of Mech & Aero Eng, NC State University

Grant # W911NF-10-1-0118

Proposal # 57461-EG

Foreword:

The overall objective of this project was to increase the understanding of the effects of pressure on soot formation and destruction in laminar diffusion flames burning both simple hydrocarbon and complex real fuels. A more complete understanding of the soot formation processes at elevated pressure (e.g., 30 atm) will enable the design of more efficient diesel engines. Higher efficiency will help reduce the logistical demand transportation fuels place on the entire DoD and thus increase the 'tooth to tail' ratio, enhancing force sustainability. By reducing soot emissions, survivability of assets will be increased by reducing the vehicle's IR signature. First, experiments were conducted for ethylene flames with different diluents. Quantification of hydrocarbon species was done by extraction of samples using a quartz micro probe along the centerline of the flame and analyzing them using both a GCMS/FID and a TCD to calculate the mole fraction of the various species in the sample volume. The flame temperature was measured by both thermocouples and two-color pyrometry. Soot volume fraction, primary particle size, and number density were also measured by line of sight attenuation. The pressure effects on the measured quantities are investigated. Second, laminar flames of pre-vaporized liquid fuels are being measured with the aid of a custom built electrospray vaporizer.

Table of Contents

Table of Contents	2
List of Appendixes, Illustrations and Tables.....	4
1. Statement of Problem Studied	6
2. Experiment Setup	7
2.1 Experimental Apparatus	7
2.1.1 Pressure Vessel.....	7
2.1.2 Flange Translation	9
2.1.3 Burner Translation Stage.....	9
2.1.4 Fuel and Air Delivery System.....	10
2.1.5 Pressure Building and Metering.....	11
2.1.6 Diffusion Flame Burner Setup	11
2.1.7 Liquid Fuel Prevaporizer	13
2.2 Flame Shape.....	14
3. Experimental Methodology.....	16
3.1 Sampling	16
3.1.1 Microprobe.....	16
3.1.2 Sample Collection.....	17
3.1.3 Validation of Sample Collection System.....	18
3.1.4 Calibration for C ₂ -C ₇ species.....	19
3.1.5 Sample Collection Setup for PAH	21
3.1.6 Calibration for PAH.....	21
3.1.7 Sample Collection and Calibration for Permanent Gases	22
3.2 Flame Temperature Measurement using Thermocouple	23
3.2.1 Thermocouple and Extension Arm.....	23
3.2.2 Radiation Correction	23
3.3 Two-Color Pyrometry	24
3.3.1 Soot Surface Temperature	24
3.3.2 Soot Volume Fraction.....	25
3.4 Line of Sight Attenuation and Laser Scattering	26
3.4.1 Soot Volume Fraction.....	26
3.4.2 Average Particle Diameter	27
3.4.3 Number Density	28
4. Summary of Most Important Results.....	28
4.1 Hydrocarbon Species Concentrations in Nitrogen-diluted Ethylene Flame	28
4.1.1 C ₂ -C ₇ Hydrocarbons	29
4.1.2 Polycyclic Aromatic Hydrocarbons.....	33
4.2 Soot Precursor Formation and Temperature in Ethylene Flames with Different Diluents	36
4.2.1 Flame Temperature.....	36
4.2.2 C ₂ -C ₇ Hydrocarbon Species.....	37
4.3 Soot Surface Temperatures and Soot Volume Fractions in Ethylene Flames with Different Diluents with Two-color Pyrometry	51
4.4 Results of Laser Extinction and Scattering	58

4.4.1. Soot Volume Fraction.....	58
4.4.2 Average Particle Diameter	62
4.4.3 Number Density	64
4.5 Results of Real Fuels	65
5. Summary of Conclusions	65
5.1 Hydrocarbon Species Concentrations in Nitrogen-diluted Ethylene Flame	65
5.2 Soot Precursor Formation and Temperature in Ethylene Flames with Different Diluents	66
5.3 Soot Surface Temperatures and Soot Volume Fractions in Ethylene Flames with Different Diluents with Two-color Pyrometry	66
5.4 Laser Extinction and Scattering Measurements	67
5.5 Prevaporized Liquid Fuels	67
Bibliography.....	68

List of Appendixes, Illustrations and Tables

Figure 2.1: Pressure Vessel.....	8
Figure 2.2: The riser section under the table with the base flange raised.....	9
Figure 2.3: The riser section under the table with the base flange	9
Figure 2.4: Linear stepper motor translation stage	10
Figure 2.5: Layout of gas delivery system.....	11
Figure 2.6: Metal foams with 100 ppi and diameters 50 mm, 40 mm and 25 mm.....	12
Figure 2.7: Laminar diffusion flame burner with metal insert and metal foam.....	12
Figure 2.8. Electrospray atomizer	14
Figure 2.9: The sequence of images clockwise from left shows	15
effects of buoyancy induced instabilities at 12 atm.....	15
Figure 3.1.1 : The design iterations of the quartz sampling probe and the Y- Section.....	17
Figure 3.1.2: The final quartz micro probe design affixed using RTV on a threaded bolt	17
Figure 3.1.3: Layout of sampling setup for atmospheric pressure experiments	18
Figure 3.1.4: Layout of sampling setup for experiments above 1 atmosphere	18
Figure 3.1.5: Concentrations of ethylene and toluene over a single run lasting 6.5 hrs	19
Figure 3.1.7: Concentrations of ethylene and propane in calibration mix B	21
Figure 3.3.1: Two-color pyrometry workflow. Raw image acquisition followed by pixelmatching and cropping with final result yielding a temperature profile.....	25
Figure 3.4.1: Optical setup for LOSA (A – aperture, IS – integrating sphere, L – lens, M – mirror, ND – neutral density Filter, NL – negative lens, P – polarizer, PD – photodiode, PH – pinhole, PMT – photo-multiplier tube, S – beam sampler)	27
Figure 4.1.1: Centerline concentrations of ethylene (ppm) in 82.5% diluted flame.....	30
Figure 4.1.2: Centerline concentrations of acetylene (ppm) in 82.5% diluted flame	30
Figure 4.1.3: Centerline concentrations of C ₃ species (ppm) in 82.5% diluted flame.....	31
Figure 4.1.4: Centerline concentrations of 1,3 butadiene (ppm) in 82.5% diluted flame.....	32
Figure 4.1.5: Centerline concentrations of diacetylene (ppm) in 82.5% diluted flame	32
Figure 4.1.6: Centerline concentrations of benzene (ppm) in 82.5% diluted flame	33
Figure 4.1.7: Centerline concentrations of toluene (ppm) in 82.5% diluted flame	33
Figure 4.1.8: Centerline concentrations of five PAH species (ppm) in 82.5% diluted flame	35
Figure 4.1.9: Ratio of maximum concentration measured at a given pressure to the concentration at 1 atmosphere plotted against pressure on a log-log scale.	35
Figure 4.2.1. Temperature contours of four diluted flames at 1 atm	42
Figure 4.2.2. Temperature contours of four diluted flames at 2 atm	42
Figure 4.2.3. Temperature contours of four diluted flames at 4 atm	42
(a): Temperature profiles at one atmosphere	43
(b): Temperature profiles at two atmosphere.....	43
(c): Temperature profiles at four atmosphere	43
Figure 4.2.4. Temperature profiles along two radial sections along the flame.....	43
Figure 4.2.5. Mole fraction of ethylene as a function of pressure	44
Figure 4.2.6. Mole fraction of ethylene as a function of diluent	44
Figure 4.2.7. Concentrations of acetylene as a function of pressure	45
Figure 4.2.8. Concentrations of acetylene as a function of diluent.....	45
Figure 4.2.9. Concentrations of ethane as a function of pressure	46
Figure 4.2.10. Concentrations of propane as a function of pressure.....	46

Figure 4.2.11. Concentrations of propene as a function of pressure.....	47
Figure 4.2.12. Concentrations of propadiene as a function of pressure.....	47
Figure 4.2.13. Concentrations of propyne as a function of pressure	48
Figure 4.2.14. Concentrations of 1-butene as a function of pressure	48
Figure 4.2.15. Concentrations of 1,3-butadiene as a function of pressure.....	49
Figure 4.2.16. Concentrations of 1,3-butadiyne as a function of pressure	49
Figure 4.2.17. Concentrations of benzene as a function of pressure	50
Figure 4.2.18. Concentrations of toluene as a function of pressure.....	50
Figure 4.3.1: Two color temperature profiles for nitrogen diluted flames	54
Figure 4.3.2: Two color temperature profiles for argon diluted flames	54
Figure 4.3.3: Two color temperature profiles for helium diluted flames	54
Figure 4.3.4: Two color temperature profiles for carbon dioxide diluted flames.....	55
Figure 4.3.5: Peak soot surface temperatures as a function of pressure	55
Figure 4.3.6: Peak soot surface temperatures plotted against transport properties.....	56
Figure 4.3.7: Soot volume fraction (ppm) profiles for nitrogen diluted flames	56
Figure 4.3.8: Soot volume fraction (ppm) profiles for argon diluted flames.....	56
Figure 4.3.9: Soot volume fraction (ppm) profiles for helium diluted flames.....	57
Figure 4.3.10: Soot volume fraction (ppm) profiles for carbon dioxide diluted flames.....	57
Figure 4.3.11: Peak soot volume fraction (ppm) versus pressure.....	57
Figure 4.4.1: Transmissivity of left and right halves of flames at 4, 6, and 8 atm	58
Figure 4.4.2: Extinction in flames at 4, 6, and 8 atm.....	59
Figure 4.4.3: Integrated f_v at 4, 6, and 8 atm.....	59
Figure 4.4.4: Local f_v contours at 4, 6, and 8 atm	60
Figure 4.4.5: Local f_v profiles at 4, 6, and 8 atm.....	61
Figure 4.4.6: Percent of fuel carbon converted to soot.....	61
Figure 4.4.7: Q_{vv} contours at 2, 4, 6, and 8 atm	62
Figure 4.4.8: Q_{vv} profiles at 2, 4, 6, and 8 atm.....	63
Figure 4.4.9: D_{63} profiles at 4, 6, and 8 atm.....	63
Figure 4.4.10: Peak average particle diameter (D_{63}).....	64
Figure 4.4.11: Number density of primary particles at 4, 6, and 8 atm	65
Table 3.1.1: Concentrations of non-fuel hydrocarbons in the calibration mixture	20
Table 3.1.2: Concentrations of polycyclic aromatic hydrocarbons in the liquid standard	22
Table 3.2.1: Emissivities of thermocouple junction at different temperatures [53]	24
Table 4.1.1: Pressure exponents for the measured species	36

1. Statement of Problem Studied

The current research focuses on soot formation and oxidation processes in laminar jet diffusion flames at atmospheric as well as elevated pressure conditions. Of particular interest for the Army is the mitigation of soot emissions from diesel engines burning liquid fuels including diesel and jet fuels. Of fundamental interest is the ability to predict soot mechanisms in real combustion devices (*i.e.*, high pressure) with multi-component liquid fuels based on information gathered in atmospheric-pressure, laminar, gaseous jet diffusion flames. There is growing interest in measuring soot and soot precursors in high-pressure flames, but it is still limited to very few groups throughout North America and Europe. There are significant experimental challenges to operating at elevated pressures, and from previous ARO sponsored programs, the PIs have developed the capability to measure soot and soot precursors in gaseous jet diffusion flames up to 30 atm.

Hydrocarbon species concentrations, flame temperatures were measured in a laminar jet diffusion flame at elevated pressures. The objective is to better understand soot production and oxidation, which will ultimately help reduce soot emissions from engines. Quantification of hydrocarbon species was done by extraction of samples along the centerline of the flame using a quartz micro probe and analyzing them using both a GC-MS/FID and a TCD to calculate the mole fraction of the various species in the sample volume. The flame temperature was measured by both thermocouples and two-color pyrometry. The pressure effects on the measured quantities are investigated. The presence of benzene and acetylene suggests soot formation and growth, and two trends were observed with respect to hydrocarbon species concentrations. The first trend shows an increase in peak concentrations of stable hydrocarbon species, specifically benzene and acetylene, with increase in pressure. The second trend is the migration of the occurrence of the peak concentration towards flame base as the pressure increased. With respect to temperature, an increase in peak flame temperature along with reduction in the reaction zone thickness was observed as the pressures increased.

Physical and chemical effects of addition of diluents to the fuel stream (He, CO₂, N₂ and Ar) are also investigated. The measured hydrocarbon species concentrations are dramatically different among the diluted flames with the helium and carbon dioxide diluted flame yielding the largest and smallest amounts of soot precursors, respectively. The peak flame temperatures varied with diluents tested, with helium diluted flames being the hottest and carbon dioxide diluted flames the coolest. Soot surface temperatures and soot volume fractions were investigated using two-color pyrometry. Addition of the diluents to the fuel stream had a pronounced effect on both the soot surface temperatures and soot volume fractions, with helium diluted flames and carbon dioxide flames yielding the maximum and minimum soot surface temperatures and soot volume fractions respectively. At low pressures peak soot volume fractions exist at the tip of the flame, with increase in pressure the location of peak soot volume fractions shift to the center of flame wings.

Soot volume fraction, average particle diameter, and particle number density were measured by line of sight attenuation (LOSA) and laser scattering. Measurements were done in nitrogen-diluted ethylene flames at 4, 6, and 8 atm. LOSA measurements were not possible below 4 atm, as the short optical path resulted in overall extinctions of less than 1%, which is too low to resolve from noise levels. LOSA and scattering measurements of liquid-fuel flames are in

progress. The LOSA results show the same pressure dependent trends of soot volume fraction that are seen from two-color pyrometry. Scattering results show two major trends in average particle diameter. The first is a shift in location of peak average particle diameter from the flame tip to the flame wings as pressure is increased, much like soot volume fraction. The other trend is that peak particle diameter along the flame centerline is insensitive to pressure, but peak diameter in the flame wings increases with pressure.

A key aspect of this project is studying the soot properties of real fuels. To achieve this goal, a custom electrospray vaporizer was constructed capable of vaporizing multi-component liquid fuels at high pressure. Multi-component fuel vaporization in these experiments poses several challenges related to the low vapor pressures of liquid fuels, especially problematic at elevated pressure, the low fuel flow rates, and the tendency of laminar flames to become unstable at elevated pressure. Experiments with liquids fuels are ongoing.

2. Experiment Setup

2.1 Experimental Apparatus

2.1.1 Pressure Vessel

The high-pressure vessel seen in Fig. 2.1, originally designed by Li (2001), capable of reaching 30 atm, is the primary component of the setup. The pressure vessel includes a water cooling jacket, though the vessel does not get hot enough in these experiments to necessitate cooling. The pressure vessel is roughly a meter tall and has four circular flanges extending beyond its circular body. Three of the four flanges enable optical access and are fitted with BK-7 glass windows (diameter of 7.6 cm and thickness of 2.5 cm). The windows are used for alignment, viewing, and non-intrusive diagnostics. The fourth flange houses fittings for a pressure gauge connection and provision for sample extraction.

During this project, the pressure vessel system was significantly upgraded. In the original design, the burner was translated using a threaded rod which passed through an 8 in 400 blind flange on the bottom. An 8 in 400 intermediate slip-on flange was placed between the blind flange and the pressure vessel to increase working height. Whenever the burner needed cleaning or other maintenance, the pressure vessel was hoisted using a crane to expose the burner. The primary problem with this design was that the threaded rod did not provide a consistent seal at higher pressures, especially during translation of the burner. Moreover, any maintenance using the crane required assistance of another individual to retrieve the quartz chimney before complete removal of the pressure vessel.

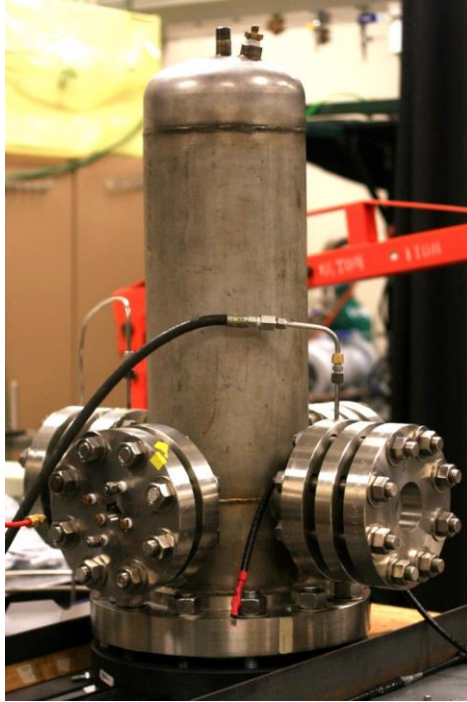


Figure 2.1: Pressure Vessel

The first step in solving the sealing problem was to design a collar that not only stabilized but also reduced the wobble in the threaded rod. Even with the installation of the collar there was a limit on the maximum pressure that could be attained due to mass leakage through the thread interface. A more permanent solution was to eliminate the use of threaded rod to translate the burner and instead use a stepper motor for accurate and precise translation of burner. There were many challenges that had to be solved to incorporate the stepper motor design. Since the main cylindrical section of the vessel was made of 6 in schedule 80 pipe, it did not provide enough room to accommodate the proposed linear translation stage replacing the threaded rod. An intermediate section (riser) was built with larger diameter pipe and flanges, providing the required room. The riser section was made by welding two 8 in 400 lb slip on flanges on to an 8 in schedule 40 pipe section. This riser increased the height of the overall setup by 6 in, which meant that the hoist could no longer be used. It was limited by the maximum height to lift the pressure vessel.

The new experimental setup was designed around a heavy-duty workbench measuring 36 in \times 30 in \times 36 in, reinforced with two 3 in angle irons, over which the “riser” section would rest, supporting the pressure vessel. The “riser” section extends below the surface of the table as seen in Fig. 2.2. Access to the burner for maintenance is now done by lowering the base flange, which has the linear translation stage-burner assembly on it.

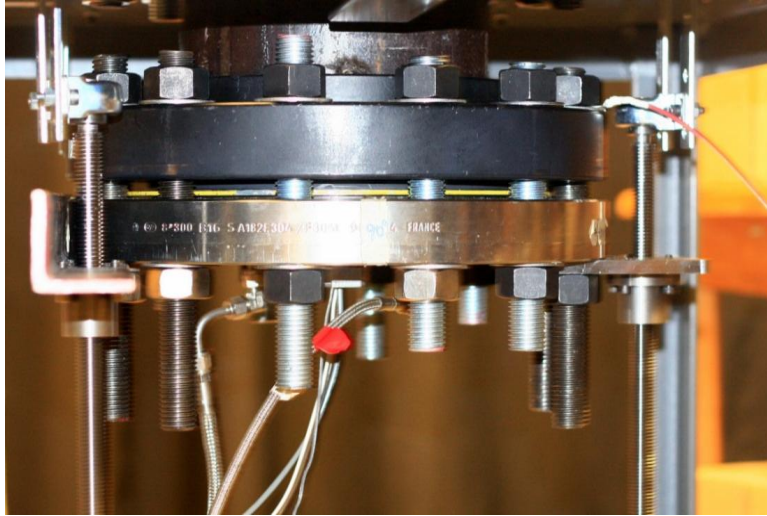


Figure 2.2: The riser section under the table with the base flange raised

2.1.2 Flange Translation

The base flange was translated by a threaded rod assembly driven by an ANSI #40 chain powered by a DC gearmotor (1/17 hp, 62 rpm) (Fig. 2.3). Three threaded rods (Precision Acme Threaded Rods: 3/4 in-10, 36 in long) were used to support the base flange. The base flange was cradled on two sides by a 2 in angle iron and a custom plate. The angle iron had two threaded rods passing through while the custom plate had the third threaded rod. The threaded rod was supported by a tapered bearing on the bottom and a pillow block bearing on the top.

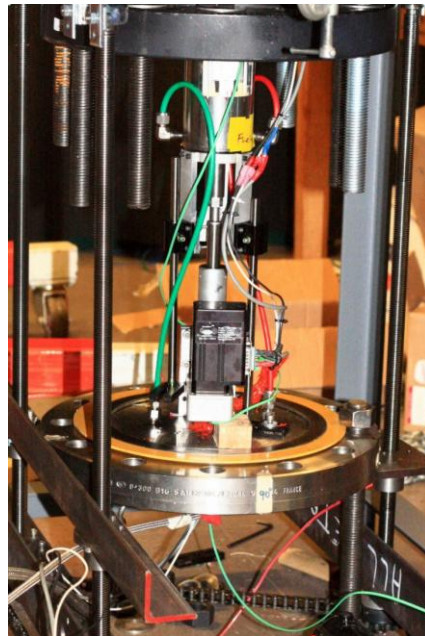


Figure 2.3: The riser section under the table with the base flange

2.1.3 Burner Translation Stage

The burner translation stage consists of a stepper motor (SmartMotor: SM1720M) driving a linear translation stage (Ultra Motion: 125-SM17-1.2-1-B/4). The linear translation stage has

the ability to translate the burner 50 mm vertically in steps of 0.05 mm. The belt-drive connecting the motor to the translation stage produces an encoder resolution corresponding to 1890 counts/mm. The stepper linear translation stage is connected to the base of the burner by custom made unions. The unions had to be designed to a particular length so that the fuel tube tip, when at the starting position, lined up with the probe sampling port access on the flange. The stepper motor is bolted to a 1/2 in mount which rests on the flange. To minimize lateral movement of the burner a linear bearing assembly was built. The burner is supported by three linear bearings translating on rods. This linear bearing setup is affixed to the flange. The burner assembly with the translation stage is shown in Fig. 2.4.



Figure 2.4: Linear stepper motor translation stage

2.1.4 Fuel and Air Delivery System

The reactant mixture and co-flow air is supplied to the burner through two stainless steel fittings that are welded to the base of the flange. The stainless steel fittings are attached to braided steel tubes outside the chamber, which carry both the reactant mixture and co-flow air. The co-flow air was initially supplied from four 310 CF cylinders connected in series. An air compressor system capable of providing 170 SLPM of air at 330 bar was installed to replace the cylinder system. Co-flow air enters a mass flow controller (Brooks 5851E) and flow values are set using a Brooks 0152 read out. The fuel and diluents were delivered by TeleDyne Hastings mass flow meters (HFM-200), the two mass flow meters were powered by a TeleDyne Hastings power supply (Model 40). This power supply was also used to set the fuel and diluent flow rates. Before every run a BIOS DC-2 flow calibrator was used to ensure accurate flow rates. The fuel and diluent were mixed thoroughly in a mixing chamber after it left the flow meters before it entered the burner. The layout of the gas delivery system is shown in Fig. 2.5.

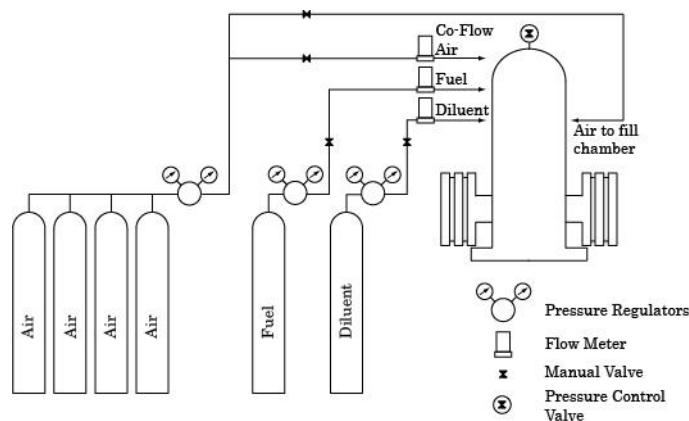


Figure 2.5: Layout of gas delivery system

2.1.5 Pressure Building and Metering

Building pressure is time consuming and very sensitive. It is accomplished by regulating the difference between entry mass flux and exit mass flux. This was initially controlled by using a ball valve connected to the exit of the exhaust port. By slowly closing the valve the exit mass flux is reduced creating a pressure differential building pressure. The valve is very sensitive, if it is closed completely or by a significant amount the flame will be extinguished. To reach higher pressures (12 atmospheres and 16 atmospheres), a secondary line is employed to supply excess air to the chamber as shown in the gas delivery system schematic Fig. 2.5. A new method of pressure regulation has been implemented. The dome pressure of a backpressure regulator is controlled by an electronic pressure regulator. The backpressure regulator prevents exhaust flow until the vessel pressure matches the control pressure. To use this system, a method of ignition while at pressure is necessary. This is accomplished with a custom sealed igniter consisting of a nickel-chromium resistance wire that heats up as electrical current passes through it. The pressure in the chamber is monitored by an external pressure gauge which has a range of 0-1000 psig. The flame is susceptible to disturbances, especially at high pressures, so flow restrictors in the fuel and co-flow lines are necessary to dampen out any fluctuations.

2.1.6 Diffusion Flame Burner Setup

The diffusion flame burner is designed based on the classic over-ventilated Burke-Schumann laminar diffusion flame. The burner has an overall height of 104 mm and the flame is established on a fuel tube 4.0 mm in diameter. Varying co-flow cross-section areas were used depending on the experiment. The fuel tube tip has a sharp 15 degree knife edge machined to it to reduce heat transfer to fuel tube and minimize turbulent eddies in the air and fuel flow. The fuel tube was packed with 0000 gage stainless steel wool to achieve a plug velocity flow of the reactant mixture and remained consistent throughout all the experiments.

Extensive modification was done to the co-flow to ensure uniform and top hat velocity profile. The initial designs incorporated ceramic honeycomb and 4 mm glass beads to straighten co-flow. The ceramic honeycomb used in the co-flow did not form a good sealing surface around the fuel tube; high velocity jets ensued as a result and caused instabilities in the flame, especially at high pressures. In the current setup the co-flow was straightened by using a combination of 2 mm glass beads and metal foam. The metal foam (DUOCEL Aluminum foam, supplied by ERG) was 100 ppi (pores/inch) and 0.8 in thick. It not only ensured even flow, but also created a good

seal around the fuel tube eliminating any high velocity jets around the fuel tube. Three different foams were made with diameters 50 mm, 40 mm, and 25 mm as shown in Fig. 2.6. Three different inserts to hold the metal foams were also machined out of aluminum.

Ethylene, although a simple hydrocarbon fuel, has a high propensity to soot, and the fact that the pressures tested encompass a wide range, it was difficult to obtain a stable flame at pressures higher than 8 atmospheres with the flows being velocity matched. This will be covered in detail in the following section. Therefore to obtain stable flames at higher pressures, the co-flow velocity had to be increased. Since a single flow meter was used throughout, larger flow rates were not possible for cases above 8 atmospheres. To obtain higher velocities in the co-flow, smaller co-flow cross sections were designed. Using a hot wire anemometer (DANTEC P-16), the velocity profile was checked over all the co-flow sections and the velocity distribution was found to vary less than 1% of the total flow over the entire cross-section. The schematic of the diffusion flame burner is shown in Fig. 2.7.



Figure 2.6: Metal foams with 100 ppi and diameters 50 mm, 40 mm and 25 mm

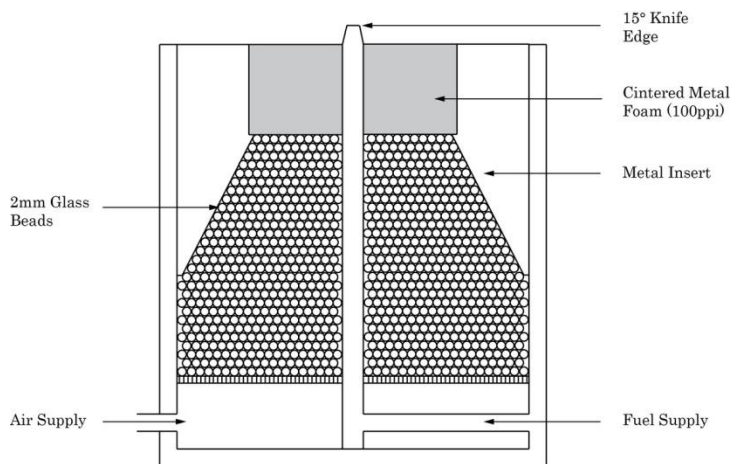


Figure 2.7: Laminar diffusion flame burner with metal insert and metal foam

A Quartz chimney (71 mm O.D, 3 mm wall thickness and 70 mm height) enclosed the burner, and was used at all times. It was necessary to avoid perturbations in the flame. The chimney was modified to incorporate smooth sliding of the sleeve, which included an access hole for both the sampling probe and thermocouple, during translation of the burner.

2.1.7 Liquid Fuel Prevaporizer

One of the objectives of this project is to understand soot formation in real fuels and their surrogates at high pressure, particularly differences between JP-8 and DF #2. To remove the complexity of multi-phase combustion, these fuels will be pre-vaporized. To prevent speciation of these multi-component fuels, fine droplets will be evaporated in a heated nitrogen stream. Due to the low fuel mass fluxes of these small laminar flames, the atomizer must be capable of producing small droplets at low flow rates. The vaporizer also needs to be rated for the pressures investigated in the experiments. An electrospray atomizer is the best choice for meeting this criterion. Unlike a pressure-atomizing spray nozzle, an electrospray can generate continuous and small particle spray. This allows fine control of the fuel flow rate with a syringe pump.

A custom electrospray atomizer, shown in Fig. 2.8, has been built to provide prevaporized multi-component liquid fuels. The principle of operation of an electrospray is as follows: A large difference in electric potential between a capillary nozzle and a downstream electrode continuously pulls small drops of fuel from the liquid meniscus at the nozzle tip. Due to the high charge in the droplets, they are self-dispersing, and a heated nitrogen carrier stream evaporates the small droplets. To increase the electrical conductivity of the fuel, an antistatic additive present in many jet fuels (Stadis 450) is doped in at 0.05% by volume. In order to meet pressure needs, and for flexibility in design and maintenance, ASME 2 in class 600 flanges were used as the housing. The capillary nozzle is attached to a copper plate with a positive voltage from 7-10 kV. The downstream ground electrode is a metal mesh screen. A 3 mm thick Teflon insert insulates the charged fuel stream from the grounded flanges between the nozzle and the mesh. The required nozzle voltage and carrier temperature are functions of the fuel and fuel flowrate. At elevated pressures, prevaporized liquid fuel flames with dilution levels similar to those of ethylene flames may not be possible, and prevaporized liquid fuels may instead be doped into diluted methane or ethylene flames.

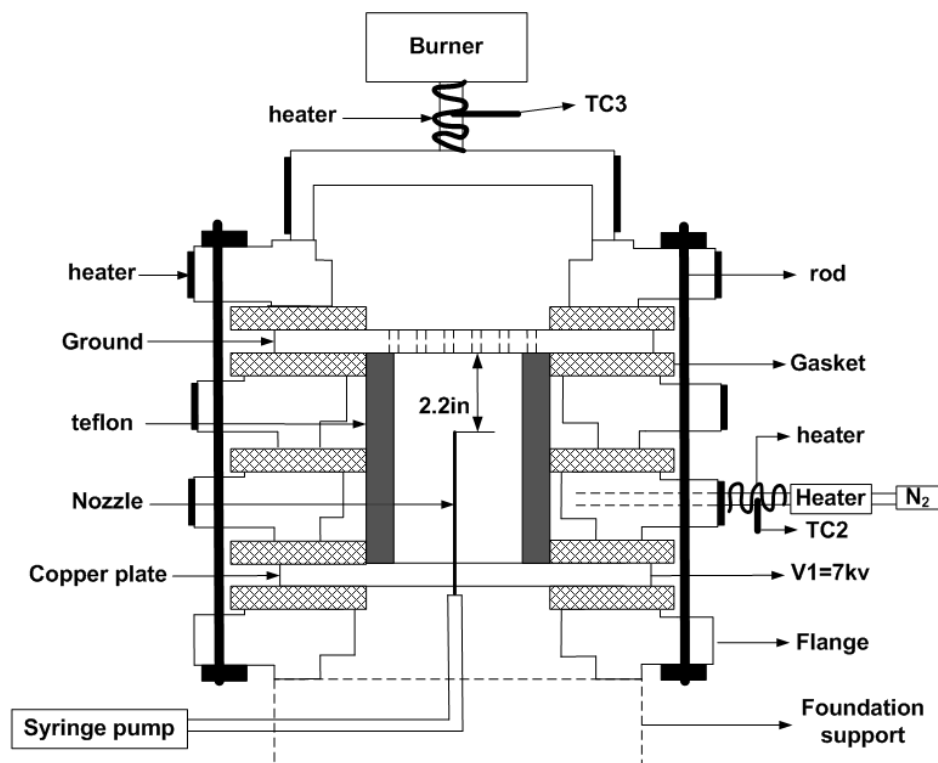


Figure 2.8. Electrospray atomizer

2.2 Flame Shape

The initial stages of the experiments were done on a ~4 cm tall flame. The flow rates were 0.1 SLPM (100 sccm) of ethylene and 0.4 SLPM (400 sccm) of Nitrogen (80% dilution by volume), with a co-flow of 76 SLPM. The flames were velocity matched up to 8 atmospheres. The mixing region existed without any shearing forces and all diffusion could be assumed to occur in the radial direction with no axial component. The 4 cm tall flame provided abundant resolution along the flame axis for extractive sampling. The flame maintained a conventional convex shape at 1 atmosphere and 2 atmospheres and begins to thin as pressure increased (McCrain and Roberts, 2005). But as the pressure increased beyond 8 atmospheres, it became significantly difficult to maintain a stable velocity matched flame as the flame front significantly contorted and flickered due to increase in buoyancy induced, even though the flame was not a sooting flame (Berry and Roberts, 2006). This highly unstable distorted flame was not desirable for any measurements. The series of pictures in Fig. 2.9 show the behavior.



Figure 2.9: The sequence of images clockwise from left shows effects of buoyancy induced instabilities at 12 atm

Although there is a dearth of extractive sampling data at elevated pressures, extensive non-intrusive studies have been done on laminar diffusion flames at elevated pressures, especially the work of Flower & Bowman (1988) and Miller & Maahs (1977) who conducted experiments on ethylene-air laminar diffusion flames up to 10 atmospheres. Flower and Bowman used fuel flow rates ranging from 0.102 to 0.294 SLPM, with an air flow rate of 252 SLPM at 1 atm (Flower and Bowman, 1988) to achieve stable flames at pressures higher than 2 atm. The air co-flow rates are significantly greater in Flower & Bowman's (1988) case when compared to the previously described flow rates. Flower & Bowman (1988) described their flame as being “greatly over-ventilated” and stated that “this air flow is 60 times the stoichiometric requirement for the highest fuel flows studied”. It was theorized that this over ventilation helped to maintain a stable flame structure, but unfortunately, with the air flow meters (which are calibrated to 100 SLPM) and air supply system (4 compressed air tanks in series) initially used in this work such high air flow rates were not achievable and also would not have been possible with the amount of air that would have been consumed, particularly at higher pressures. In experiments conducted by Miller and Maahs (1977) on a laminar methane-air diffusion flame at pressures up to 50 atm, they used a burner whose fuel tube diameter and air co-flow diameter were 3 mm and 20.5 mm respectively, with 0.0418 SLPM fuel and 2.45 SLPM air co-flow rate. By looking at the burner geometry and the co-flow air velocities it can be seen that the flows were not velocity matched. With these values as a starting point and also looking at McCrain and Roberts’ (2005) ethylene

values, it was determined by trial and error that the required air co-flow rate to maintain a stable non flickering flame at pressures higher than 8 atm was actually 4.33 times the co-flow for velocity matched flame. As mentioned before it was not possible to achieve such flow rates. Two changes were made, first the fuel flow rate was reduced to .07 SLPM, which reduced the flame height from 38 mm to ~27 mm and a smaller co-flow cross section was used enabling the 4.33 times required velocity matched co-flow of 23 SLPM with the smallest co-flow section. The new flow conditions that produced a stable non-sooting flame at 16 atmospheres were 0.07 SLPM fuel with 82.5% nitrogen making nitrogen flow 0.33 SLPM. The 82.5% dilution was chosen so that a stable non-lifted flame could be attained at atmospheric pressure and a non-smoking flame at 16 atmospheres. Although it could have been possible to go to higher pressures by reducing the fuel flow rate further, there would be a sacrifice of axial resolution as the flame height would reduce further. Therefore this experiment is limited to 16 atm.

3. Experimental Methodology

3.1 Sampling

3.1.1 Microprobe

The probe design was the first step and it was the most important step in the centerline hydrocarbon concentration measurements. The design had to be very specific, requiring a probe tip that has minimum perturbation and provide enough aerodynamic quenching to freeze chemistry and maintain an unclogged, soot free probe tip.

The probe material was chosen as quartz, as used by other researchers who have extracted samples from atmospheric flames (McEnally and Pfefferle, 1999, Kennedy *et. al.*, 1996), to avoid chemical reactions within the probe. Several iterations were made to arrive at a probe which provided the right balance for atmospheric pressure and elevated pressure sampling. The First prototype was designed using the previous researcher's (Berry and Roberts, 2006) probe. Their final probe design consisted of a y-shaped end, one arm had a sapphire rod to vibrate soot particles off the tip and the other arm was used to extract samples. While experiments were conducted with this first design, it proved to be almost impossible to maintain a perfect seal in the arm containing the sapphire rod. This would result in air being drawn in when sampling at atmospheric or cause samples to escape when sampling at elevated pressures. This ultimately resulted in lower concentration values. The first design eliminated the y-shaped end. Since the probe incorporated a stub nosed probe tip and a larger tip id, it was not possible to extract samples from the flames, especially high-pressure flames without causing significant perturbation to the flame. A smaller tip ID along with an increasing taper was introduced in the second design, as it turns out the tip ID was very small, even though purging during sampling to clear clogging of the tip, it would almost immediately clog at high soot concentration regions of the flame. When the probe is introduced into the flame, the flame should not respond to the sudden pressure drop especially at high pressures, this would result in bad sampling. None of the probes used before had a solution to this, therefore it was decided to design a probe which would cause the required pressure drop, thereby enabling sampling without disturbing the flame. Fig.3.1.1 shows the various probes designed for species sampling.



Figure 3.1.1 : The design iterations of the quartz sampling probe and the Y- Section

The third probe introduced an area ratio change from 200 μm to 1 mm then onto 4 mm ID tube. This reduced the pressure differential the flame saw at high pressures, even though it proved to be effective in causing minimum perturbations during sampling, it was almost impossible to clean the 1 mm section thoroughly, and this section deteriorated overtime due to soot on the surface. The fourth design used orifice diameter of 250 μm , designed based on McEnally and Pfefferle's (1999) probe. This design caused minimal perturbations and the probe did not clog completely. The final tip design had an increased tip ID of 300 μm , as the probe would be used at much higher soot concentration regions than before. The length of the taper section was significantly increased to 2 cm. To solve the issue with pressure drop, a separate sampling system was designed for both atmospheric and elevated pressure experiments.

The probe was sealed using RTV silicone on to a nut which could be used to precisely position the probe in the flame. The open end of the probe was connected to sampling lines by employing Teflon ferrules. The final probe design and RTV seal is seen in Fig. 3.1.2.

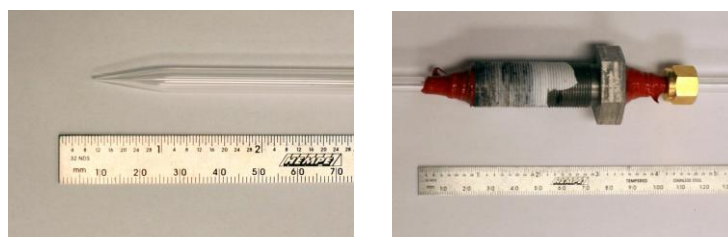


Figure 3.1.2: The final quartz micro probe design a affixed using RTV on a threaded bolt

3.1.2 Sample Collection

The samples were collected onto a 16 port multi position valve in ST configuration (Valco Part No: E2ST16MWE) with 1 mL stainless steel sample loops (Part No: SL1KSTP). This facilitated collection of multiple samples for each run, and can be connected directly to the GC-MS for analysis. To ensure accurate sample collections, two separate setups for sample collection was used, one for atmospheric pressure and the other for all other cases above atmospheric pressure. Positioning of the burner relative to the probe for sampling species was done using a Labview routine.

Fig.3.3 shows the sampling arrangement for atmospheric pressure experiments. The probe is connected to the multi-port valve using copper lines and connected to a vacuum gauge and vacuum pump. A flow meter is also used in the sample collection line to ensure consistent sample flow rate volumes and also used to check for probe clogging. Fig. 3.1.4 shows the sample

collection system used for high-pressure experiments. The only difference is that the vacuum pump/vacuum gauge is replaced by a valve and pressure gauge. The pressure gauge was used to ensure constant pressure drop with all the cases. Maintaining a constant volume flow rate through the probe ensured consistent sample collection.

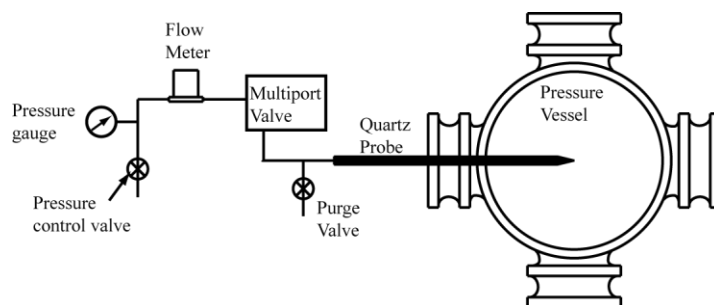


Figure 3.1.3: Layout of sampling setup for atmospheric pressure experiments

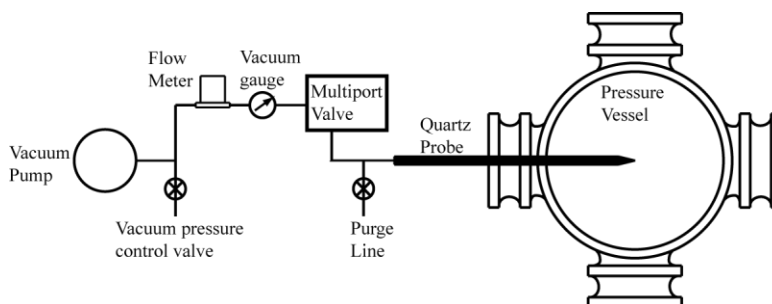


Figure 3.1.4: Layout of sampling setup for experiments above 1 atmosphere

3.1.3 Validation of Sample Collection System

To ensure consistent and repeatable sample collections several tests were conducted to validate the sampling system. The first fundamental test was checking sample volume collection. This was done by extracting samples at both atmospheric pressure and elevated pressure at the fuel tube exit without the flame. For an 80% diluted flame, the ethylene concentration values had to be 200000 ppm. The sample volume flow rate and pressure drop values were noted for the setting which gave the expected ethylene concentrations, these settings were used for all cases.

It was also observed that the samples that were collected into the loops had to be vented to atmospheric pressure before being passed into the GC. The calibration gases were also vented to atmospheric pressure within the sample loop before passing into the GC. The reason for this is to maintain a consistent sample volume to provide a uniform response factor as the samples in the loops expand in the GC carrier lines.

The longevity of the samples collected and stored in the loops was checked to determine if they deteriorated over time. For example, the GC took 26 minutes to analyze one sample (with the method used for C₂-C₇ species). So if there are 15 samples to analyze from one run, the total analysis time is 6.5 hours. Samples were collected from a single location in the flame to fill all the sample loops with identical samples and were checked to see if any samples happened to deteriorate. In Fig. 3.1.5 the concentrations of ethylene & toluene are plotted (lowest and highest measured species in terms of concentrations). There is almost negligible variation in the

concentration over time with standard error over the mean (SEM) of 86.33 ppm for ethylene and 0.0144 ppm for toluene.

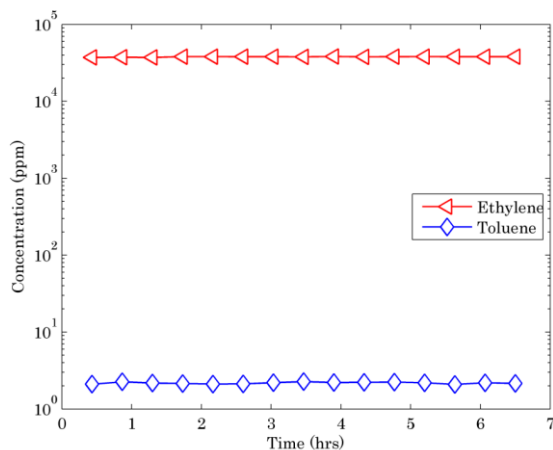


Figure 3.1.5: Concentrations of ethylene and toluene over a single run lasting 6.5 hrs

3.1.4 Calibration for C_2 - C_7 species

A Shimadzu GC-MS/FID QP2010 was used for all gas chromatography analysis of hydrocarbon species. For C_2 to C_7 species the FID was used with a RT-QSPLOT column (30 m, 0.32 mm ID, 0.25 μ m film thickness). The method developed for this analysis starts at 40 C, steps to 140 C @ 25 C/min reaching a final temperature of 250 C. The total run time was 25 min. Samples were injected at 250 C with a detector temperature of 60 C. The first calibration mixture, referred as Mix A, custom made by Air Liquide, had 100 ppm of each sample that was quantified. Since measured concentrations are many orders of magnitude different from the standard mixture, there are inherent errors in quantification due to extrapolating and interpolating too far when only using this one calibration mixture. A second mixture, referred as Mix B was then made with the same gas components whose concentrations were chosen based on the values obtained using Mix A. The specifics of the calibration mixture are listed in Table 3.1.1. Using a GC-MS the samples were analyzed for other detectable species in the flames besides the 10 that were in the calibration mixture. Five other species were identified, three C_3 (propene, propyne and propadiene) species and two C_4 (1,2 butadiene and Diacetylene) species. The peaks appeared beside other species which were present in the mixture, whose concentrations were known. So assuming similar response factors for the peaks with same number of carbon atoms to the species in the mixture, over a short retention time, the 5 species were quantified.

The software used with the GC-FID provided 3 options which could be used to fit the two calibration standards. The three options were linear, exponential and mean response factor (RF). An experiment was designed with the two calibration mixture to arrive at the best fit method. A total of 5 different fit methods were used with the two mixtures A and B. they are listed as follows: 1 Point Mix A, 1 Point Mix B, 2 Point Mean RF, 2 Point Linear, and 2 Point Exponential. Using 1 point meant a single concentration value for calibration and 2 point meant the use of concentration values of both Mix A and Mix B. With the 5 methods, the two standard mixtures (Mix A and B) were analyzed as unknowns, in doing so the fitting methods can be validated for accuracy by comparing the calculated concentration to the actual concentration. To

illustrate this, two species will be looked at in detail, with all the above mentioned fits, such that they encompass the maximum and minimum concentrations in the both the mixtures.

Table 3.1.1: Concentrations of non-fuel hydrocarbons in the calibration mixture

Species	Mixture A (ppm)	Mixture B (ppm)
Ethylene	100	100000
Acetylene	95	10000
Ethane	100	31.8
Propane	100	5
1 Butene	100	10
1,3 Butadiene	100	2000
Cyclopentane	101	4.89
n Hexane	101	5.1
Benzene	101	1020
Toluene	100	10.5

Fig. 3.1.6 and Fig.3.1.7 show the results of the five fits in calculating the concentration of ethylene and propane in the standard mixtures. It can be seen that the respective 1 point calibration technique works for the corresponding mix (either A or B depending on whether 1 point A or 1 point B is used). Although 2 point linear calibration technique seems to yield better results upon closer inspection, the 2 point exponential fit yields the most accurate results. With these results all the samples were quantified using a 2 point exponential fit if two standards are used.

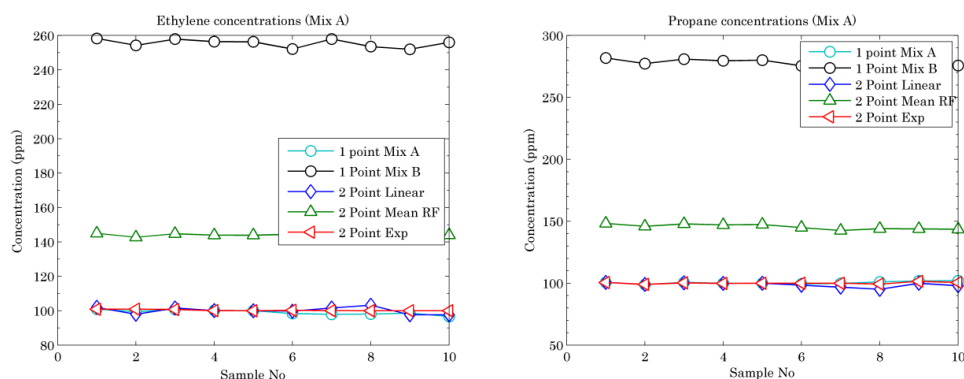


Figure 3.1.6: Concentrations of ethylene and propane in calibration mix A

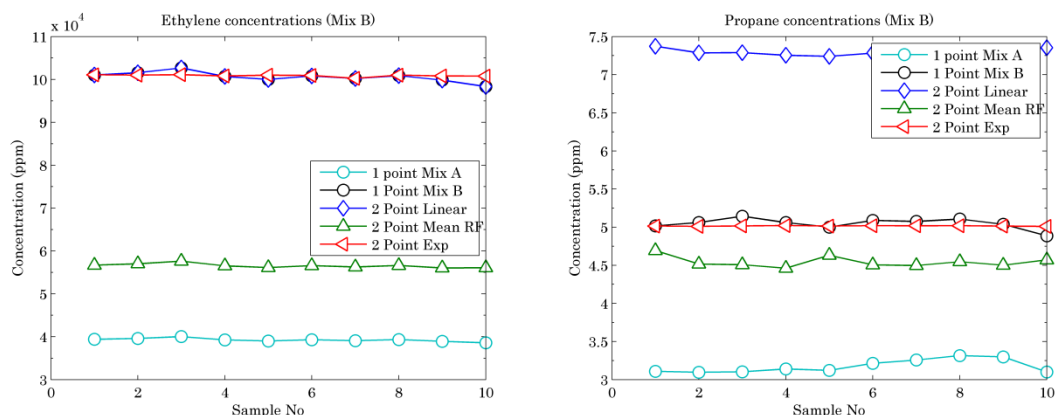


Figure 3.1.7: Concentrations of ethylene and propane in calibration mix B

3.1.5 Sample Collection Setup for PAH

The sampling system for PAH involved the sampling setup employed for C₂-C₇ species, the only difference being that all the lines including the probe, sample loops, copper tubing and GC transfer lines had to be heated to prevent adsorption of products on to walls. The sample loops and the transfer lines were heated by flexible heating element and the flange was heated by a heater strip. The probe, flange and sample line was controlled by one controller whereas the loop and the GC transfer lines were controlled by a second temperature controller. McEnally and Pfefferle (1999) measured species up to C₁₂ in a co-flow diffusion flame at atmospheric pressure and Olten and Senkan (1999) conducted PAH measurements in a counter flow diffusion flame while maintaining all transfer lines at 300 C. A temperature of 300 C was not possible with the current setup due to the effect the heating element had when it came in contact with the RTV on the probe. Even though the sealant was rated for higher temperature, the element temperature was higher than the set temperature and this caused deterioration in the RTV material in the contact surfaces between the heating element and RTV. A constant temperature of 160 C was maintained to prevent adsorption of compounds on to the walls of the tubes. The maximum weight of the detected species is limited to anthracene C₁₄H₁₀, whose amounts are ascertained based on comparison of measured concentration values to Olten and Senkan (1999). Even though other heavier compounds were detected in trace amounts, they are adsorbed on to the walls of the tubing. The setup was heated for an hour to reach a steady equilibrium temperature before sample collection and as soon as the samples were collected, the loops were quickly transferred to the GC for analysis. The GC transfer lines and the loops were kept hot throughout the analysis process.

3.1.6 Calibration for PAH

The Shimadzu GC-MS/FID QP2010 was used with an Rtx-5 column (30 m, 0.32 mm ID, 0.25 µm film thickness). The injection temperature was 280 C with helium as carrier gas. The detector was at 330 C. The GC method began with 60 C held for 1 min, to 300 C at 12 C/min to 330 C at 6 C/min and hold for 2 min. A 1 µl standard sample was injected using a syringe and held for 1.0 min before analysis. The measurement of PAH samples involved use of liquid standards, as opposed to gas phase unknown samples. To incorporate phase change errors a correction factor was incorporated during data analysis whenever liquid sample injection is used.

to compare with gas sample injections. This is crucial because the liquid sample when injected expands in the injection port to a larger volume, if this volume is not taken into account when comparing 1 ml of gas sample gas, incorrect results will be produced. The correction is done by calculating the vapor volume (Agilent Technologies). Since manual injection was performed, the calibration method was developed after averaging multiple injections. Using the above specified formula we can calculate accurately the sample volume, which was 471 μL . With the calculated sample volume, and using a factor of 0.471, all the PAH species are quantified. The standard mixture used for quantifying PAH species was purchased from Accustandard (AE-00025) consisting of the following components dissolved in Acetonitrile, Table 3.1.2.

Table 3.1.2: Concentrations of polycyclic aromatic hydrocarbons in the liquid standard

Species	Concentration ($\mu\text{g}=\text{mL}$)
Acenaphthene	25.14
Acenaphthylene	25.02
Anthracene	25.16
Benz(a)anthracene	10.12
Benzo(b)fluoranthene	25.18
Benzo(k)fluoranthene	10.14
Benzo(g,h,i)perylene	25.18
Benzo(a)pyrene	20.16
Chrysene	20.10
Dibenzo(a,h)anthracene	20.16
Fluoranthene	40.16
Fluorene	41.22
Indeno(1,2,3-cd)pyrene	25.08
Naphthalene	50.20
Phenanthrene	30.20
Pyrene	41.20

3.1.7 Sample Collection and Calibration for Permanent Gases

An agilent GC system with TCD was used to measure carbon monoxide, carbon dioxide and methane. Sampling was identical to the methods and set up used for $\text{C}_2\text{-C}_7$ hydrocarbon species. Calibration was performed by employing a mixture which contained 10% of the three species (10000 ppm). A ShinCarbon ST micropacked column was used for analysis. The column was 2 m long, 2 mm ID and 1/8 in OD. Samples were injected at 100 C with a flow rate of 10 mL/min. The detector was set at 200 C. The column oven temperature began at 40 C, held for 3 min, and then reached 250 C at 8 C/min. The method was stopped after CO_2 eluted. To avoid saturation of the detector when measuring CO_2 two different methods were used. The TCD detector sensitivity was different for the two methods, which enabled detection of large quantities of CO_2 without detector saturation.

3.2 Flame Temperature Measurement using Thermocouple

3.2.1 Thermocouple and Extension Arm

The flame temperature measurements were conducted with the aid of an uncoated, 75 μm pre-welded type R (Pt-Pt/13% Rh) thermocouple. The thermocouples were not coated since the catalytic effects were expected to be small in a non-premixed flame which has small radical concentrations (McEnally *et al.*, 1997; Miller *et al.*, 1993). The thermocouple was translated in the radial direction by a stepper motor (SmartMotor: SM1720M) driving a linear translation stage (Ultra Motion: 125-SM17-1.2-1-B/4), which was identical to the motor translating the burner. The side with the sampling probe access was to be used for thermocouple access. In order to accommodate the stepper motor and be able to operate at elevated pressures, an extension arm was built which would bolt onto one of the arms of the pressure vessel. The extension section composed of one 3 in 400 slip on flange and one 8 in 400 lb slip on flange welded onto ends of an 8 in schedule 40 pipe section. The stepper motor was mounted onto the face of an 8 in 400 lb blind flange which was guided by rods to position the thermocouple in the access hole of the chimney at its starting position. The thermocouple wire was enclosed in a ceramic tube, and to prevent any sag in the thermocouple a mount and holder assembly was designed to provide rigidity and thereby ensure accurate positioning of the thermocouple. A LabView program was used for controlling thermocouple positions and data acquisition.

3.2.2 Radiation Correction

The temperature measured by the thermocouple is the junction temperature, which does not reflect the accurate gas temperature. In order to measure gas temperatures accurately the temperature values have to be corrected for radiation losses. For a small filament in the cross flow the rate of heat transfer by axial conduction is negligible compared to that of convection and radiation (McEnally *et al.*, 1997). The energy balance equation for the junction is given by the expression

$$\epsilon_t \sigma T_j^4 = \frac{k_g Nu_j}{2d_j} (T_g^2 - T_j^2) \quad (1)$$

where

T_g = gas temperature

T_j = junction temperature

ϵ_t = junction emissivity

σ = Stefan-Boltzman constant

Nu_j = junction Nusselt number

d_j = junction diameter

$k_{g0} = k_g/T_g$, where k_g is gas thermal conductivity

The left hand side of Eq. 1 is the radiation heat loss per unit area and the right hand side is convection heat gain per unit area (Holman, 1983). The junction diameter d_j is 75 μm , and ϵ_t values are obtained from temperature-dependent data measured by Bradley and Entwistle (D'Anna and Kent, 2003; Bradley and Entwistle, 1968) for S type thermocouples. Since the compositions of S and R are similar the emissivity values can be used. Table 3.2.1 lists the emissivity values and corresponding temperatures from D'Anna and Kent (2003). From Holman (1983) and McEnally and Pfefferle (1997) $k_{g0} = 6.54 \times 10^{-5} \text{ W/mK}^2$. Nu_j was calculated from expansion for spheres from Acrivos and Taylor (1962). With all the known values in Eq. 1, gas temperature (T_g) was calculated.

Table 3.2.1: Emissivities of thermocouple junction at different temperatures [53]

Temperature (C)	Emissivity ε
600	0.1287
700	0.1450
800	0.1559
900	0.1723
1000	0.1837
1100	0.1937
1200	0.2032
1300	0.2122
1400	0.2206
1450	0.2243

3.3 Two-Color Pyrometry

3.3.1 Soot Surface Temperature

The soot surface temperatures were measured by employing Two-color wavelength emission technique. The ratio of the intensity is calculated using plank's equation. The intensity of radiation from a black body varies with wavelength and it also depends on the temperature of the black body. This is described mathematically by Planck's equation (Zhao and Ladommatos, 1998)

$$E_{b,\lambda}(T) = \frac{C_1}{\lambda^5 \left[e^{\left(\frac{C_2}{\lambda T}\right)} - 1 \right]} \quad (2)$$

where $E_{b,\lambda}(T)$ is the monochromatic emissive power of a black body, C_1 and C_2 are first and second Planck's constants. Two images were obtained for the same flame at two wavelength, 550 nm and 650 nm, and a source with known temperature is used to obtain a known intensity ratio at the same wavelengths (550 nm and 650 nm). With the intensity ratio of the known temperature source at the two wavelengths calculated, the unknown flame temperature can be inferred by measuring the intensity ratio of the flame at 550 nm and 650 nm and comparing it to the known emissivity ratio. A MatLab code written by Zhang *et al.* (2013), was used to calculate soot surface temperatures. A Phantom V4.3 non-intensified high speed camera coupled with a Nikkor 105 mm lens was used to capture the flame images and a tungsten halogen light source (Ocean LS-1-LL, 2800 K lamp) coupled with different ND filters was used for calibration.

The procedure for obtaining the 2D temperature profiles, as shown in Fig. 3.12, involved acquiring a raw image from the camera, which contained the images of both the flames, split by a stereoscope which had 550 nm and 650 nm filters. The two images from the raw file are cropped and matched at the pixel level. The matched images are then used to calculate the intensity ratios and thereby determine temperature.

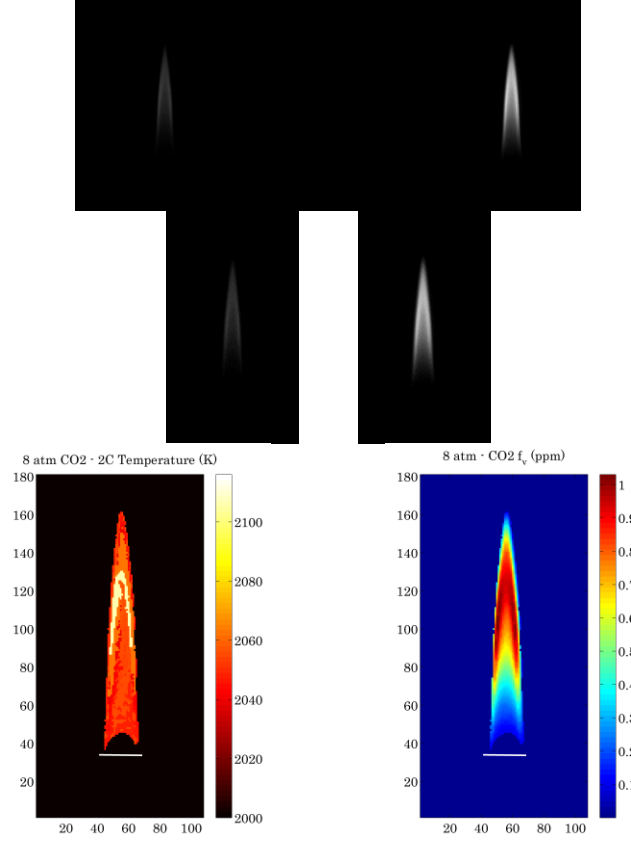


Figure 3.3.1: Two-color pyrometry workflow. Raw image acquisition followed by pixelmatching and cropping with final result yielding a temperature profile

3.3.2 Soot Volume Fraction

Soot volume fractions are measured based on the technique used by De Luiis *et al.* (1998) and Cignoli *et al.* (2001). Cignoli *et al.* (2001) and coworkers extended on two color pyrometry technique used to measure soot surface temperature and used mathematical equations to solve for soot volume fractions based on temperature and spectral properties of soot (Manta, et al., 2001). Using the temperatures obtained from the two-color method, a new code was written using the equations from De Luiis *et al.* (1998) and Cignoli *et al.* (2001). The soot volume fraction f_v is given by the expression

$$f_v = \frac{l_{abs}}{L} \ln \left[1 - 0.99 \frac{E_{s\lambda}}{E_{l\lambda}} \exp\left(\frac{-c}{\lambda} \left(\frac{1}{T_L} - \frac{1}{T_s}\right)\right) \right] \quad (3)$$

where, l_{abs} is the natural length of absorption at a given wavelengths (550 nm or 650 nm) with respect to soot spectral properties (calculated), L is the width of the flame under consideration (measured), $E_{s\lambda}$ is the measured intensity of the flame (measured), $E_{l\lambda}$ is the intensity of the calibrated lamp emission (calculated), c is the Planck's constant, λ is the wavelength of the filter, T_L is the temperature of the lamp source, T_s is the soot surface temperature. The method used for soot volume fraction differed from temperature measurement in the sense that it is possible to calculate soot volume fraction (f_v) for each of the two images at 550 nm and 650 nm. Only the 650 nm image was used as it was the brightest image of the two.

3.4 Line of Sight Attenuation and Laser Scattering

3.4.1 Soot Volume Fraction

Soot volume fraction was also measured by line of sight attenuation (LOSA). LOSA is a widely used technique based on the extinction of light as it passes through an absorbing medium, in this case, soot laden regions of a flame. As light passes through the medium, it can be absorbed, reflected, scattered, or transmitted, with reflections usually negligible. The relative amount of scattering is dependent on particle diameter, d , concentration, refractive index, and the wavelength, λ , of incident light. If particles are in the Rayleigh regime such that

$$\frac{\pi d}{\lambda} < 0.3$$

scattering can be neglected. This is a good approximation in parts of a flame where soot particles are less developed and of a smaller size, but becomes a larger source of error as particle size increases. Beer's law relates the transmissivity of the light at a given wavelength, τ_λ , which is the ratio of transmitted light (I_λ) to incident light ($I_{\lambda,0}$), to the path integral of the local absorption coefficient, $K_\lambda^{(e)}$ (Thomson, 2004).

$$\tau_\lambda = \frac{I_\lambda}{I_{\lambda,0}} = \exp \left(\int_{-\infty}^{\infty} K_\lambda^{(e)} ds \right)$$

This equation relates the measured light intensities to the integrated extinction coefficient. In order to determine the local extinction coefficient in a non-uniform absorbing medium, some additional knowledge of the extinction field is required. For axis-symmetric fields, such as this co-flow diffusion flame, a tomographic inversion of integrated path measurements yields the local value. There are several numerical methods for performing the inversion, including Abel inversion, onion peeling, and filtered back projection (Dasch, 1992). The method used in this work is the 3-point Abel inversion. The local absorption coefficient can be related to soot volume fraction, f_v , using Rayleigh-Debye-Gans theory

$$f_v = \frac{K_\lambda^{(e)} \lambda}{6\pi(1 + \rho_{sa,\lambda})E(m)_\lambda}$$

Where $E(m)_\lambda$ is the imaginary soot refractive index function given by

$$E(m)_\lambda = -\text{Im} \left(\frac{m^2 - 1}{m^2 + 2} \right)$$

and $\rho_{sa,\lambda}$ is the ratio of scattering and absorption coefficients. This ratio can be estimated with knowledge of several parameters of the soot morphology. As these parameters are at this time under investigation, this value is assumed to be zero, as is often done for particles in the Rayleigh regime previously described. The choice of refractive index of soot can be a source of great uncertainty, and several values can be found in literature. An index of refraction appropriate for the wavelength of the laser used, $m = 1.99 + 0.89i$, was chosen (Krishnan *et. al.*, 2000).

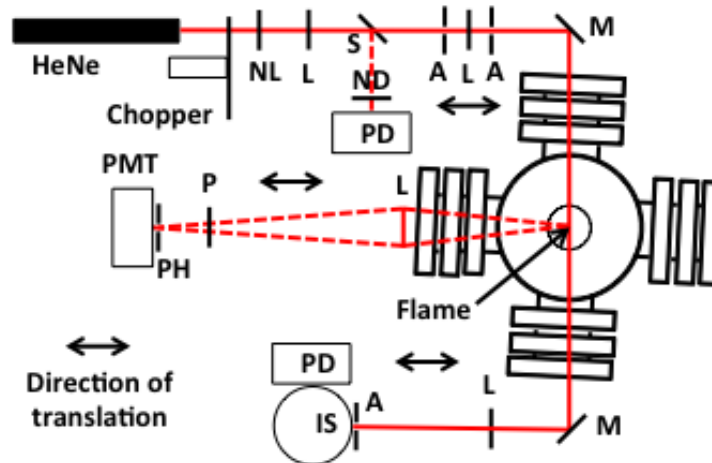


Figure 3.4.1: Optical setup for LOSA (A – aperture, IS – integrating sphere, L – lens, M – mirror, ND – neutral density Filter, NL – negative lens, P – polarizer, PD – photodiode, PH – pinhole, PMT – photomultiplier tube, S – beam sampler)

A layout of the optics is shown in Fig. 3.4.1. The light source was a 21 mW HeNe laser which produced a beam at 632.8 nm with vertical polarization. The beam was chopped at 550 Hz, and this frequency was referenced by three lock-in amplifiers which measured the signal from two photodiodes and one photomultiplier tube (PMT). The 0.7 mm beam was first directed through an $f = -25$ mm plano-concave lens, and then collimated by passing through an $f = 150$ mm plano-convex lens to a diameter of 4 mm. Expanding and collimating the beam before focusing into the vessel is done for two reasons. First, this reduces the minimum waist size of the beam at the focal point to 100 μm . Second, since the beam is larger as it passes through the vessel windows, variations in local transmission have less of an impact. A portion of the beam was sampled and directed through a neutral density filter of O.D. 1.0 to a photodiode to provide a constant reference of instantaneous beam intensity, as it was seen to change by several percent over time. A quartz diffuser plate was placed in front of the photodiode detector surface to limit the effect of spatial variation in detection. The main beam was focused by a 25.4 mm plano-convex lens of $f = 500$ mm onto an aluminum mirror, and reflected 90° through the pressure vessel. All optics and detectors were mounted on two motorized Newport linear translation stages, which allowed the beam to be translated relative to the flame position. The pressure vessel was angled slightly relative to the incoming beam to reduce the effect of window reflections. After passing through the vessel, the beam was reflected towards a 50 mm diameter $f = 300$ mm bi-convex lens which was used to reduce the effect of beam steering. The lens focused the beam through an aperture into a 50 mm diameter integrating sphere. The integrating sphere was found to be very important in obtaining good transmission measurements as the beam is translated through the flame. A photodiode mounted to the integrating sphere measures the transmission intensity. In order to relate the measured reference laser intensity to the local intensity in the pressure vessel, a point-by-point transmission measurement was made at each horizontal position of each window.

3.4.2 Average Particle Diameter

If the Rayleigh regime assumption holds, the average particle diameter can be found from the sixth to third moment ratio of particle probability functions (Santoro *et. al.*, 1983) and is given by

$$D_{63} = \lambda \left(\frac{4E(m)_\lambda Q_{vv}}{\pi^2 F(m)_\lambda K_\lambda^{(e)}} \right)$$

Where $F(m)_\lambda$ is given by

$$F(m)_\lambda = \left(\frac{m^2 - 1}{m^2 + 2} \right)^2$$

If the local absorption coefficient is already known, the vertically polarized scattering cross section Q_{vv} can be used to determine average particle diameter. Since the scattering cross section is proportional to the incident intensity of light on the scatterer, attenuation of light from extinction must be accounted for in determining the local incident intensity. However, if the field of local extinction coefficients is known, this can be accomplished.

As seen in Fig. 3.4.1, a 50 mm diameter $f = 300$ bi-convex lens placed as close as possible to the vessel was used to collect light scattered 90° relative to the beam. By virtue of containing the burner in a pressure vessel, there was an inherent limitation on solid angle available for scattering collection. However, the 85×10^{-3} sr collection angle was found to provide more than adequate signal. The scattered light was focused through a polarizer onto a $150 \mu\text{m}$ pinhole mounted on a Hamamatsu PMT. A line filter ($632.8 \pm 0.2 \text{ nm}$) was also placed between the pinhole and PMT. The PMT was mounted to a 3-axis manual translation stage to allow for precise positioning. To align the PMT, a small conical pin was placed in the fuel tube to provide a good scattering surface. This allowed the focal point of the lens to be precisely located. Due to window and vessel reflections, there is some signal noise. The scattering signal was correlated to Q_{vv} by using the Rayleigh scattering of two gases with known scattering cross-section, propane and nitrogen. The known ratio of scattering cross sections was compared to the measured ratio of signals to determine the level of noise, and relate the measured signal to scattering cross section.

3.4.3 Number Density

Once f_v and D_{63} are known, if one assumes an exponential approximation of the self-preserving distribution function, the number density of particles can be found from (Santoro *et al.*, 1983)

$$N = \frac{12f_v}{\pi D_{63}^3}$$

4. Summary of Most Important Results

4.1 Hydrocarbon Species Concentrations in Nitrogen-diluted Ethylene Flame

The nitrogen diluted ethylene-air flame at atmospheric pressure appeared bulbous and flame emission was dominated by chemiluminescence from CH^* due to the very high dilution level. As the pressure increased, thermal emissions from the sooting region became more important and expanded into progressively larger fractions of the flame. At the highest pressures investigated, the soot emission region extended all the way down to the nozzle lip. The definition of the flame height used for all pressures is the visible flame height based on soot incandescence, and there was sufficient soot incandescence at all pressures to measure this flame height. As the pressure increased from 1 to 8 atmospheres, the cross-sectional area of the flame decreased linearly with pressure as observed by (McCrain and Roberts, 2005; Bento *et al.*, 2006;

Miller and Maahsm 1977; Flower and Bowman, 1986) and the luminosity of the flame increased significantly due to the power dependence of soot volume fraction on pressure. The flame height is very insensitive to pressure. With increasing pressure the decrease in velocity is compensated by an increase in buoyancy, resulting in a constant flame height at all pressures as observed by (McCrain and Roberts, 2005; Roper and Smith, 1977; Thomson *et. al.*, 2005; Joo and Gülder, 2011), despite different fuels or dilution levels. In the figures to follow, the axial sampling locations are normalized by the visible flame height measured for each case, and reported as a percentage of the flame height. The following sections will discuss in detail the observed trends in species centerline mole fractions (ppmv), axial location of the peak concentration, and the effect of increasing pressure on the same. The presented data is an average over multiple runs with uncertainties represented as peak standard deviation value for each profile. The standard deviation is the highest for the propane with $\pm 12\%$, followed by toluene with $\pm 9\%$ and the other C_3 species with $\pm 6\%$. All other species have standard deviations $< \pm 3\%$ and are not plotted.

4.1.1 C_2 - C_7 Hydrocarbons

The centerline concentration profiles of ethylene for the 82.5% nitrogen diluted flame at various pressures are shown in Fig. 4.1.1. As expected, the concentrations of ethylene decrease along the axis of the flame from the base to tip, and reaches nearly zero at approximately 80% flame height at atmospheric pressure. The concentration measured at the base of the flame was 174,700 ppm, which is very close to the expected concentration of 175,000 ppm (corresponding to 82.5 % dilution). As the pressure increases from 1 to 8 atmosphere, the rate of ethylene consumption (i.e., slope of the concentration profile) becomes more negative, and the location at which ethylene is completely consumed shifts closer to the base of the flame, where almost all ethylene is consumed by 50% flame height at 8 atm. Kim *et al.* (2008) measured hydrocarbon species concentrations at elevated pressures up to 8 atmospheres in ethylene laminar diffusion flames and found decomposition of ethylene produced abundant acetylene. The observed behavior in the atmospheric flame is consistent with atmospheric pressure measurements conducted by McEnally and Pfefferle (1999) and Hamins *et al.* (1988) in a less diluted flame. All non-fuel hydrocarbon concentrations that have been measured show a common behavior; they are negligible near the burner surface (although increasing species transport, as a consequence of steeper gradients and decrease in radial distance, with pressure causes higher concentrations of non-fuel hydrocarbons in the lower regions of the flame) then increase along the centerline and reach a maximum concentration at some height before dropping to zero at a location below the tip of the flame.

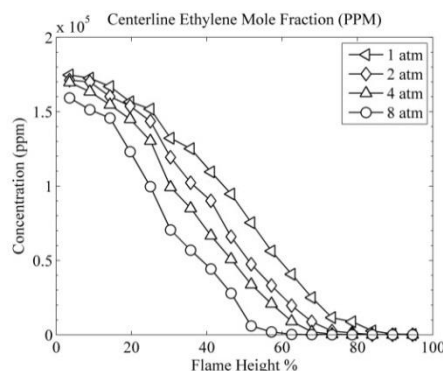


Figure 4.1.1: Centerline concentrations of ethylene (ppm) in 82.5% diluted flame

Figure 4.1.2 shows centerline concentration profiles of acetylene, an important species in the formation and growth of aromatics necessary for soot formation through the Hydrogen-abstraction- C_2H_2 -addition (HACA) Mechanism (Frenklach, 2002). This mechanism proposes a process involving two reaction steps; the first step being the removal of a hydrogen atom from the reacting hydrocarbon by a gaseous hydrogen atom, followed by the addition of a gaseous acetylene molecule to the radical site formed. From this standpoint, acetylene concentrations are directly related to the rates of soot production. Fuels with a high propensity to soot (such as ethylene) have a favorable thermal decomposition pathway to acetylene (Frenklach, 2002; McEnally and Pfefferle, 2000). As seen in Fig. 4.1.2, acetylene concentrations at 1 atmosphere increase to a maximum value at roughly 80% flame height and then proceed to decrease. As the pressure increases, the peak concentration of acetylene decreases and the location of the peak concentration shift closer to the base of the flame down to 22% at 8 atmosphere, indicating rapid pyrolysis of the fuel to acetylene and followed by conversion of acetylene to heavier soot precursors. As discussed in McEnally and Pfefferle (2000) and Castaldi *et al.* (1996), acetylene is formed by successive removal of H atoms from ethylene. As there is a direct correlation between the amount of acetylene formed and amount of ethylene from this reaction mechanism, one should expect lower acetylene concentrations as the ethylene concentration decreases with pressure and is evident in Fig. 4.1.2, as the overall peak concentration of acetylene drops with increase in pressure.

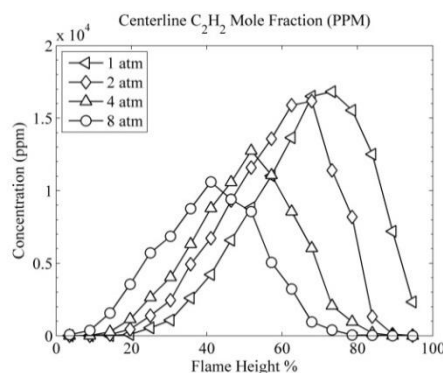


Figure 4.1.2: Centerline concentrations of acetylene (ppm) in 82.5% diluted flame

C_3 species are of importance as they are believed to form the propargyl radical whose self-reaction forms benzene (Castaldi *et al.*, 1996; Wang and Frenklach, 1997; McEnally *et al.*, 2006). Four different C_3 species were quantified and their concentration profiles are shown in Fig. 4.1.3. The peak concentration of propane (4.1.3a) is seen to dramatically decrease with

pressure. The other three C₃ species, propene (Fig. 4.1.3b), propadiene (Fig. 4.1.3c) and propyne (Fig. 4.1.3d) all have similar concentration profiles, where the peak concentration increases with pressure and the location of peak concentration migrates towards the base of the flame. The behavior of these unsaturated three-carbon species is very different than the three-carbon alkane. Hamins *et al.* (1988) also measured these C₃ species in an ethylene diffusion flame diluted 79% with nitrogen at 1 atmosphere and noted the concentration of propadiene to be half of propyne, with propene falling between the two. Obviously the absolute concentrations will be different, but the ratios between these three species are preserved in this very dilute flame, with propyne peaking at 41.6 ppm, propadiene peaking at 19.9 ppm and propene peaking at 31 ppm at one atm.

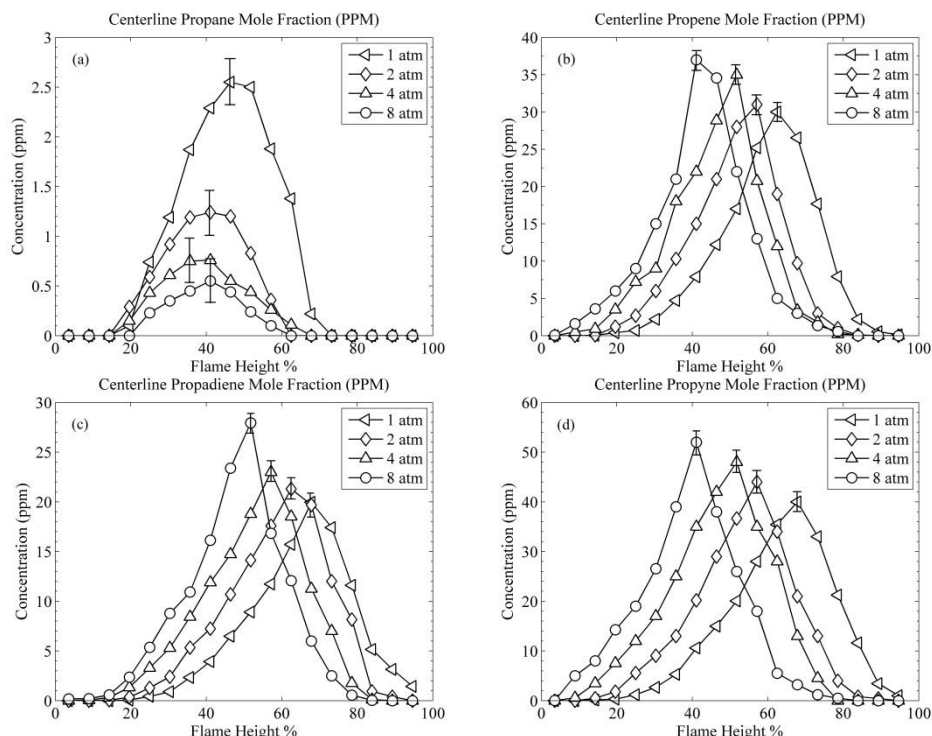


Figure 4.1.3: Centerline concentrations of C₃ species (ppm) in 82.5% diluted flame

Large concentrations of C₄ were measured in the ethylene diffusion flames, and two in particular are reported here: 1,3 butadiene and diacetylene. The concentrations of 1,3 butadiene, shown in Fig. 4.1.4, were the largest measured among the C₄ species with peak concentrations reaching 1310 ppm at 8 atm. C₄ radicals have been suggested as possible aromatic ring precursors, by reaction with acetylene to form phenyl radical and benzene (McEnally and Pfefferle, 1999; Frenklach, 2002; Castaldi *et al.* 1996).



Comparing the profiles of diacetylene (1, 3 butadiyne), shown in Fig. 4.1.5, to that of 1,3 butadiene, it is clear that they behave very differently, with concentrations of diacetylene decreasing monotonically with pressure while 1,3 butadiene increases with pressure. The diacetylene behavior is observed in the concentration profiles of acetylene. This suggests that the formation reactions for diacetylene are completely different from 1,3 butadiene and that its concentration profiles follow a similar trend to acetylene's. 1,3 butadiene is believed to be

formed by reaction mechanisms which involve C_2H_3 and C_2H_4 . Diacetylene is formed by dehydrogenation of vinyl acetylene which is formed by a direct reaction involving C_2H_3 and C_2H_2 (McEnally and Pfefferle, 2000; Castaldi *et al.* 1996).

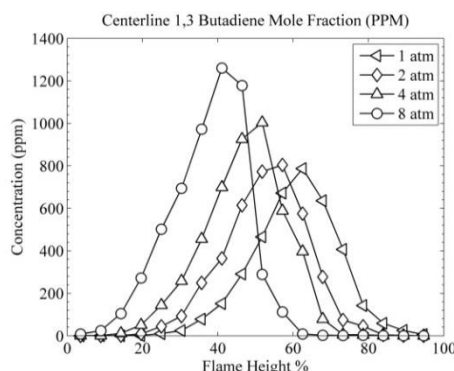


Figure 4.1.4: Centerline concentrations of 1,3 butadiene (ppm) in 82.5% diluted flame

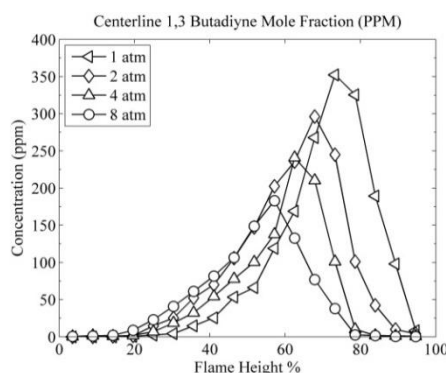
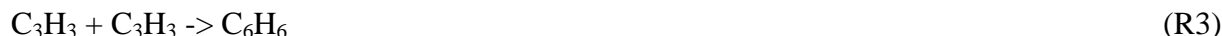


Figure 4.1.5: Centerline concentrations of diacetylene (ppm) in 82.5% diluted flame

The concentrations of benzene are of interest because C_6H_6 rings recombine to form polycyclic aromatic hydrocarbons, the building blocks of the soot primary particle. It has been shown that the formation of benzene can follow at least two reaction pathways (McEnally and Pfefferle, 1999; Frenklach, 2002; Castaldi *et al.* 1996, Wang and Frenklach, 1997).



The concentration profiles of benzene are shown in Fig. 4.1.6, where the concentration of benzene increases from the base of the flame and reaches its maximum concentration at 70% of the flame height. The peak concentration of benzene increases with pressure, indicating sustained formation of benzene throughout all the pressures. McEnally and Pfefferle (1999) measured C_6H_6 concentrations and found that the concentrations of acetylene were roughly 100 times higher than that of measured benzene concentrations, which is consistent with the measurements in this highly diluted ethylene flame.

The heaviest species measured using the unheated collection system and FID with PLOT column was toluene. Peak concentrations of toluene also increase with pressure and the location of peak concentration moves closer to the base of the flame, as shown in Fig 4.1.7. This behavior was observed in most species.

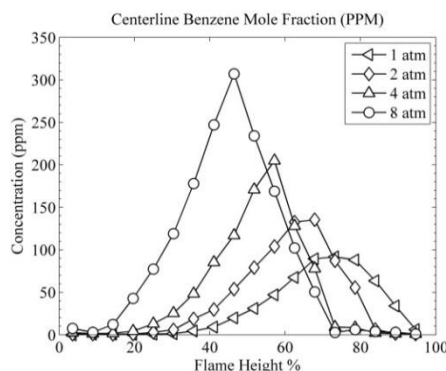


Figure 4.1.6: Centerline concentrations of benzene (ppm) in 82.5% diluted flame

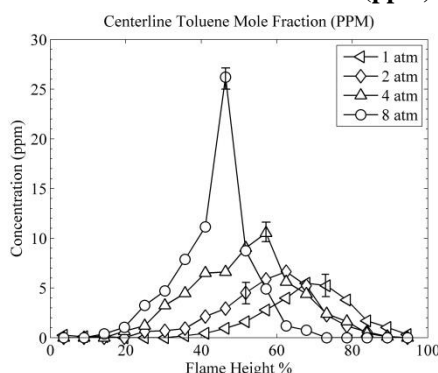


Figure 4.1.7: Centerline concentrations of toluene (ppm) in 82.5% diluted flame

Another interesting trend to note is that the portion of the flame length over which appreciable concentrations can be measured is longer at 1 atmosphere and becomes shorter with pressure. High concentrations of non-fuel hydrocarbons are present lower in the flame at higher pressures atmospheres for most of the species measured, due to an increase in the transport of the measured species with increase in pressure.

4.1.2 Polycyclic Aromatic Hydrocarbons

The most abundant PAH measured in the flame at all pressures was naphthalene, shown in Fig. 4.1.8a, with a peak concentration of 202 ppm at 8 atm. The concentration profile of naphthalene at 1 atmosphere is quite interesting as significant concentrations exist much higher in the flame when compared to 1 atmosphere data from McEanlly and Pfefferle (1999). The lower concentration of PAH occurring lower in the flame studied here is consistent with the appearance of the flame, where there is very little soot incandescence low in the flame, whereas McEnally and Pfefferle (1999) reported a highly luminous flame, beginning to soot at approximately 56% flame height which roughly coincides to their reported peak concentration of naphthalene, which is also higher due to higher fuel flow rates. Soot incandescence appears at roughly 80% flame height, which corresponds to the peak naphthalene concentration. A common pathway to the formation of naphthalene is through the formation of naphthyl radical by acetylene addition to 2-ethylphenyl radical, which is formed by H-atom abstraction from phenyl acetylene (Wang and Frenklach, 1997). The parent compound required to form the precursors required for PAH formation are identical to the ones involved in formation of the C_4 and C_6 species.

Acenaphthalene, shown in Fig. 4.1.8b, is the next most abundant PAH, which is formed by direct reaction of the $C_{10}H_7$ radical and acetylene, and peak concentrations of acenaphthalene are 182 ppm at 8 atm. McEnally and Pfefferle (1999) measured 37 ppm in a co-flow diffusion flame atmospheric pressure. The current study yields a comparable 32 ppm at 1 atmosphere. Acenaphthene (Fig. 4.1.8c), an ethylene substituted species on naphthalene, concentrations are 3 ppm and 50 ppm at 1 and 8 atmosphere respectively. Phenanthrene (Fig. 4.1.8d) and anthracene (Fig. 4.1.8e) are the two 3-ring PAH species that were measured. Phenanthracene can be produced by acetylene addition at alpha and beta positions of naphthalene followed by ring closure. Anthracene is formed by acetylene addition to the adjacent beta site. Since alpha addition is more thermo-chemically favorable (Olten and Senkan, 1999), this could explain higher concentrations of phenanthrene than anthracene. All PAH species disappear by 80% flame height at the highest pressure (8 atmosphere). Although other heavier PAH species were detected, including 4 ring pyrene in all the cases, the calculated concentrations did not compare to published data, which leads us to believe that species above anthracene were adsorbed onto the sample tube walls.

In order to further understand the dependence of the concentrations of the various species on pressure, the maximum concentration measured at each pressure, normalized by the concentration at 1 atmosphere, are plotted against pressure on a log-log scale for all the quantified species. A linear fitting is then applied to understand the pressure dependence of the various measured hydrocarbon species, and to relate to the pressure exponent scaling observed in soot volume fraction measurements. Figure 4.1.9 illustrates the pressure dependence of the measured hydrocarbon species and Table 4.1.1 lists the pressure exponents and R-square value of the fit for all the species. Positive pressure exponents indicate enhanced production with pressure whereas negative exponents indicate disappearance of the corresponding species. Ethylene concentrations peaked at the base of the flame due to lack of chemistry, and is not significantly affected by pressure, which results in very weak pressure dependence as expected. Peak concentration of acetylene decreases with an increase in pressure as it is converted into heavier compounds more effectively, resulting in a negative pressure exponent of -0.2. Looking at the four C_3 species, we see that with the exception of propane, which has a negative pressure exponent of -0.78, the concentrations have a mildly positive pressure exponent of 0.09-0.14, indicating pressure dependence. Among the C_4 species, diacetylene has a negative pressure exponent (-0.29) similar to acetylene, whereas 1,3 butadiene and 1 butene have a positive pressure dependence, with pressure exponents 0.19 and 0.21 respectively. Looking at benzene and toluene, we begin to see stronger pressure dependence with pressure exponents increasing to 0.57 and 0.63 respectively. The PAH have the strongest pressure dependence, with pressure exponents between 0.8 and 1.47. Soot volume fraction studies conducted on high-pressure ethylene flames yield a pressure exponent of 1.1-1.26 (McCrain and Roberts, 2005; Flower and Bowman, 1986; Thomson *et. al.*, 2005; Joo and Gülder, 2011). The trends in pressure exponents show that the dependence of peak concentrations on pressure increases with the increase in molecular weight of the species, with PAH having the strongest pressure dependence.

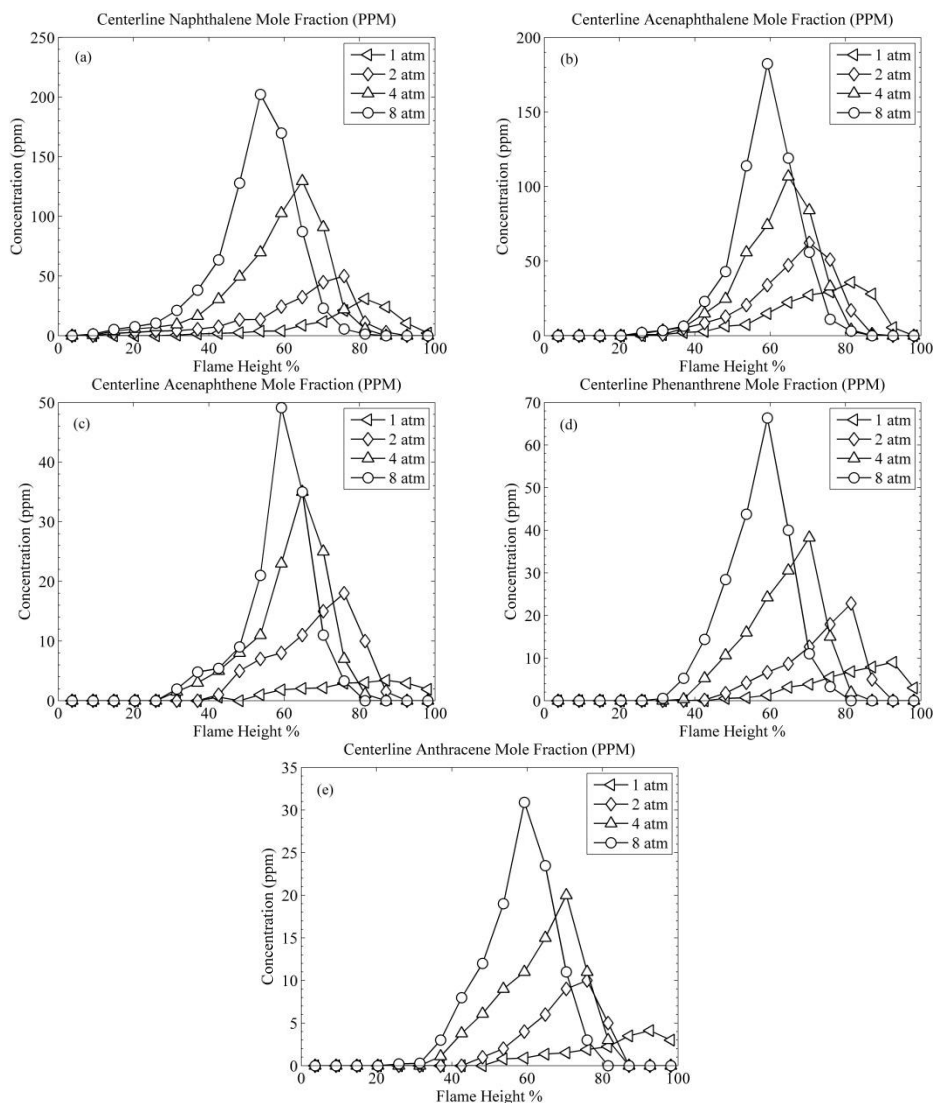


Figure 4.1.8: Centerline concentrations of five PAH species (ppm) in 82.5% diluted flame

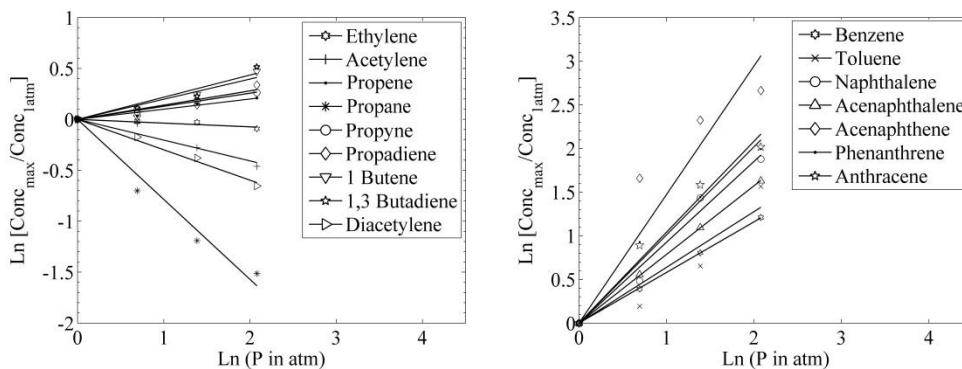


Figure 4.1.9: Ratio of maximum concentration measured at a given pressure to the concentration at 1 atmosphere plotted against pressure on a log-log scale.

Table 4.1.1: Pressure exponents for the measured species

Species	Pressure Exponent	R ²
Ethylene	-0.03	.854
Acetylene	-0.20	.940
Propane	-0.78	.972
Propene	0.09	.955
Propyne	0.12	.998
Propadiene	0.14	.925
1,3 Butadiene	0.19	.914
1 Butene	0.21	.946
Diacetylene	-0.29	.988
Benzene	0.57	.999
Toluene	0.63	.910
Naphthalene	0.92	.978
Acenaphthalene	0.8	.999
Acenaphthene	1.47	.891
Phenanthrene	1.00	.979
Anthracene	1.04	.977

4.2 Soot Precursor Formation and Temperature in Ethylene Flames with Different Diluents

4.2.1 Flame Temperature

Figures 4.2.1, 4.2.2 and 4.2.3 show the in-flame 2D temperature contour data collected using an R-type (Pt-Pt/13% Rh) thermocouple with the four diluents up to four atmospheres. The data are plotted as a function of the physical distances in the radial and axial directions. The color scales are uniform for all the four flames to easily ascertain the effects of the type of diluent and pressure on flame temperature. It should be noted that the fuel mass flux and the dilution level (82.5 % by volume) were kept constant for three flames (helium, argon and nitrogen). Whereas, the dilution was reduced to 78% by volume with carbon dioxide flame at all pressures to achieve a flame at one atmosphere. CET (Chemical Equilibrium with Transport properties) code (Gordon and McBride, 1971) was used to compare the adiabatic flame temperature at one atmosphere for 82.5% and 78% dilution cases. Adiabatic flame temperatures from CET for a CO₂ flame at one atmosphere yielded 1900 K and 2000 K at 82.5% dilution and 78% dilution respectively. Whereas adiabatic flame temperatures for helium flame yielded 2200 K and 2260 K at 82.5% dilution and 78% dilution respectively. There is a 100 K difference in the CO₂ diluted flame between the two dilution levels, possibly due to the equilibrium between CO₂ and CO+O₂, whereas only a 50 K difference in the helium diluted flame. The measured flame temperatures yielded 1760 K for the CO₂ flame and 2140 K for the helium diluted flame, with a difference of 380 K. The difference in the CET temperature values are 201 K, which is primarily due to dilution effects as CET does not take into account the radiative losses from soot. Therefore the difference in flame temperature at one atmosphere between CO₂ and helium is a combination of both soot loading and the type of diluent. CET yields no difference between the adiabatic flame temperatures of helium and

argon (both chemically inert and monoatomic & 2233 K at 1 atmosphere). Whereas, a difference of 170 K is observed in measured temperature and are likely explained by the differences in thermal diffusivities between argon and helium. Guo *et al.* (2002) numerically investigated the effects of inert addition to the fuel stream of an atmospheric pressure ethylene diffusion flame and observed higher temperatures with helium dilution than argon dilution, caused by differences in thermal diffusivities. Nitrogen (being diatomic) has a peak flame temperature of 1930 K, which is comparable to argon which has 1980 K. This could be explained by their similarity in thermal diffusivities. The flame cross-section area reduces with increase in pressure, evident looking at four atmosphere case in Fig. 4.2.3. Flame heights were measured accurately during the major hydrocarbon species concentration measurements, and when comparing the physical flame height to the height at which maximum flame temperature is observed, it agrees relatively well, thus confirming the findings of McEnally and Pfefferle (2000). The peak flame temperatures increase for all four flames with increases in pressure. The ‘squiggles’ in the temperature profiles are not real, and are a function of the limited spatial resolution of a physical probe.

The radial distribution of temperature at two axial locations, 7 mm (in red) and 23 mm (in blue), are plotted as a function of pressure in Fig. 4.2.4. Figure 4.2.4a shows the radial temperature profiles at these two locations at one atmosphere. The helium-diluted flame at 7 mm has the lowest temperature along the centerline; this is due to the helium flame being lifted at one atmosphere. When comparing argon and nitrogen, the temperature profiles for argon are slightly higher than that of nitrogen due to the relatively higher thermal diffusivity of argon. Figure 4.2.4b shows the radial temperature profiles at two atmospheres, where the reduction of the flame cross sectional area is clearly evident by the radial locations of the peak temperature. Since the helium-diluted flame is also lifted at 2 atmospheres, although the lift-off length reduces by 40% in going from one to two atm pressure, the helium diluted flame still has the lowest temperature at the centerline at 7 mm. The helium-diluted flame temperature profiles at 23 mm show increased soot loading along the outer edges of the flame. The radiation loss results in temperature reduction along the outer edge and a nearly flat temperature profile. The other three diluents have much lower soot loadings, and thus have lower radiative heat loss along the outer reaction zone, resulting in higher temperatures along the edge of the flame compared with the centerline. The radial temperature profiles at four atmospheres (Fig. 4.2.4c), measured at 23 mm, show that, due to the strong dependence of soot volume fraction on pressure, all the flames, regardless of diluent, have sufficient soot radiative losses to generate a nearly flat temperature profile. The carbon dioxide-diluted flame yields the lowest peak flame temperature, which clearly indicated the chemical effect of CO₂ due to its high heat capacity and the radiative heat losses with CO₂.

4.2.2 C₂-C₇ Hydrocarbon Species

All measured non-fuel hydrocarbon concentrations show a common behavior; they are negligible near the burner surface (although increase in species transport with increase pressure causes higher concentrations of non-fuel hydrocarbons in the lower regions of the flame) then increase along the centerline and reach a maximum concentration at some height before dropping to zero at a location below the tip of the flame (Abhinavam Kailasanathan, 2013a).

Ethylene concentrations as a function of pressure and flame height are plotted for the four diluents in Fig. 4.2.5. The definition of the flame height used for all pressures is the

visible flame height based on soot incandescence, and there was sufficient soot incandescence at all pressures to measure this flame height. The ethylene concentration with helium dilution is of most interest, as the flame is lifted. Given the fact that the binary diffusion coefficient of helium is the largest among the four diluents tested, the helium added to the fuel stream diffuses away rapidly (due to its higher mobility) as the mixture exits the fuel tube leaving relatively high concentrations of ethylene in the lifted region, leading to higher than expected concentration of ethylene. Ethylene concentrations begin to drop upon entering the flame region where it is consumed. With increase in pressure, the lift-off height decreases and the region of initial increase in ethylene concentrations narrows. As pressure is increased from one to eight atmospheres, the ethylene concentrations diminish while being consumed completely by 60% of the flame height at eight atmospheres. The argon-diluted flame shows a gradual consumption of ethylene, particularly in the lower 20% of the flame. Although the flame is not lifted, the relatively high binary diffusion coefficient of argon leads to higher concentration values and it is not actually due to decreased consumption rate. With increasing pressure there is a notable difference in the rate of consumption of ethylene similar to that observed in the helium diluted flame. With carbon dioxide dilution, a significant difference in the slope of ethylene specifically at eight atmospheres was found, which could be due to CO₂ increasing the consumption rate of ethylene at elevated pressures. Liu *et al.* (2001) lists the various possible reactions involving CO₂ (R1-R7):



As shown through Liu *et al.*'s (2001) potential reactions, there are several ways carbon dioxide can take part in the physical reaction promoting further reactions with C₂H₄, which could explain the rapid consumption of fuel. In the nitrogen-diluted flame, the rates of consumption of ethylene are similar from one to eight atmospheres with the magnitudes of initial and final concentrations changing with change in pressure. This can be attributed to the increase in rates of reactions and species transport with increase in pressure.

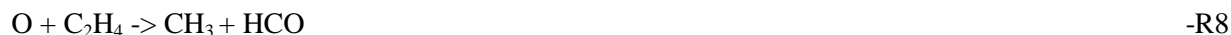
Figure 4.2.6 shows the effects of different diluents on ethylene concentrations at a given pressure. For a given pressure, the effect of each diluent varies. This is most evident in the one atmosphere case, where the concentration profiles are driven by diluent binary diffusion coefficients. It should be noted that a CO₂ diluted flame at one atmosphere was not possible; hence the absence of one atmosphere CO₂ concentration profiles. In all cases ethylene concentration diminishes most rapidly with helium dilution, whereas the opposite is true for carbon dioxide dilution. With increases in pressure, the concentration profiles become steeper and appear closer together, indicating the dominance of chemistry over transport at higher pressures.

Figures 4.2.7 and 4.2.8 show the concentrations of acetylene (C₂H₂) plotted for all cases as a function of pressure and diluent. The highest concentrations of acetylene occurred at

the lowest pressure tested (one atmosphere for helium, argon and nitrogen; two atmosphere for carbon dioxide) with helium and carbon dioxide flame producing 31000 ppm and 9200 ppm, respectively. Although nitrogen and argon share similar physical properties, the concentrations of acetylene are greater and occur lower in the flame for the argon diluted flame, resulting in more soot production. This could potentially be explained by comparing the mobility of argon to nitrogen. Argon diffuses away from the centerline to the periphery of the flame leaving a larger concentration of fuel, and thus larger concentration of acetylene. On the contrary, there is negligible diffusion of nitrogen from centerline to periphery due to absence of a nitrogen concentration gradient. Acetylene is formed by successive removal of H-atoms from ethylene (McEnally and Pfefferle, 2000). The abundance of ethylene in the helium-diluted flame is responsible for the acetylene concentrations observed.

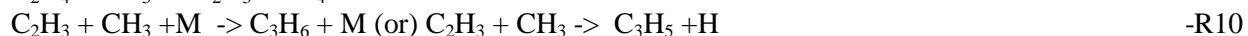
Figure 4.2.9 shows the concentrations of ethane (C_2H_6) plotted for each diluted flame as a function of pressure. Ethane could be a combustion intermediate formed by direct reaction of ethylene with hydrogen, which is clearly evident in the various concentration profiles. Ethane concentrations are significantly higher in the helium-diluted flame, resulting from the abundance of ethylene due to diffusion of helium from the centerline to the periphery of the flame. There is a consistent increase in the amount of ethane (although physical properties of the diluents governed the differences in the concentration values) with increase in pressure from one to eight atmospheres. It is interesting to note that in the carbon dioxide-diluted flame, higher levels of ethane are produced due to reactions involving CO_2 generating an abundance of H-radicals.

The concentrations of propane (C_3H_8), the largest alkane measured, are plotted for all the cases as a function of pressure and the diluent and shown in Fig. 4.2.10. Propane concentration profiles vary dramatically with helium addition as opposed to the other three diluents (nitrogen, argon and carbon dioxide). Comparing flames with diluents other than helium, argon had the lowest concentration of propane at 2.3 ppm, followed by nitrogen with 2.6 ppm and CO_2 with the highest concentration at 5.8 ppm. A possible explanation for higher propane concentrations measured in the carbon dioxide-diluted flame could be the reaction of oxygen atom from CO_2 promoting reactions and an increase in species with odd number of carbon atoms (McEnally and Pfefferle, 2000)



The abundance of ethylene in the lifted helium flame is coupled with the premixing and results in CH_3 radicals formed through R8. This leads to significant increases in concentrations of C_3H_8 .

The above-mentioned steps hold true for the other measured C_3 species: propene, propyne and propadiene, shown in Figs. 4.2.11, 4.2.12 and 4.2.13 respectively. The concentrations of these C_3 species in the helium flames are significantly higher than in the other three flames, possibly due to the following reactions:



Allyl and propyl radicals are formed, in abundance, through R9 and recombine to form the three C_3 species. Both premixing and the abundance of ethylene in the helium-diluted flame promote formation of the parent molecules required for formation of the C_3 species. When comparing argon- and nitrogen-diluted flames, the C_3 concentrations are similar. CO_2 -

diluted flames produce marginally higher C₃ species concentrations, likely due to availability of oxygen radical promoting R8 reaction. Propane concentrations in the helium-diluted flames stand out as they are seen to increase with increase in pressure, explained by the partial premixing.

Measurements of 1-butene, 1,3-butadiene, 1,2-butadiene, and diacetylene represent the C₄ class of compounds. The behavior observed for concentrations of 1-butene stands out as a unique trend when comparing all diluents. The concentrations of 1-butene, shown in Fig. 14, are the highest for helium-diluted flames with 30 ppm and 91 ppm at one atmosphere and eight atmospheres, respectively. Following helium was carbon dioxide flame with 8 ppm and 12 ppm at two atmospheres and eight atmospheres, respectively. This abundance of 1-butene, particularly in the helium flame, could be attributed to the abundance of CH₃ radical formed by R8, which reacts with acetylene in the following reaction steps:



The presence of oxygen radicals in the CO₂ diluted flame results in CH₃ radicals through R8, explaining the higher 1-butene concentrations, when compared to the argon- and nitrogen-diluted flames. Although the acetylene concentrations between the argon- and nitrogen-diluted flames are different, there is very little change in concentrations of 1-butene between argon- and nitrogen-diluted flames. The peak concentration values of 1-butene are 3.0 ppm and 4.3 ppm at one atmosphere and eight atmospheres in argon, whereas in the nitrogen diluted flame it is 5.0 ppm and 8.0 ppm at one and eight atmospheres, respectively.

The concentrations of 1,3-butadiene, Fig. 4.2.15, is of great interest as it is a crucial step in formation of the phenyl radical, which directly relates to benzene formation. As expected, the concentrations of 1,3-butadiene are greatest in the helium-diluted flame (the sootiest of the four flames) with 2300 ppm at one atmosphere and peaking at 2900 ppm at two atmospheres. The 1,3-butadiene concentration then drops with further increase in pressure from four to eight atmospheres, signifying acceleration of the reactions which form benzene/phenyl radical, and thus PAHs and soot. Simply worded, rapid recombination of 1,3-butadiene into parent molecules to form soot is more evident in the helium-diluted flame. Carbon dioxide-diluted flames have the least amount of 1,3 butadiene at the respective pressures, which signifies less soot precursor formation. When comparing argon- and nitrogen-diluted flames, it is clear that argon produces marginally higher concentrations of 1,3 butadiene, with 950 ppm in argon and 800 ppm in nitrogen flames at one atmosphere. In most instances, the concentrations of 1,3-butadiene increase with increases in pressure. However the concentrations in argon-diluted flame from four to eight atmospheres does not show an increase, but rather a plateau. This indicates that in heavily sooting flames, less 1,3 butadiene is observed at elevated pressures. 1,2-butadiene, a structural isomer of 1,3 butadiene, was also detected but in trace amounts and similar trends were observed.

The last of the C₄ species measured is 1,3-butadiyne or diacetylene (Fig. 4.2.16). It is formed by reaction of vinyl radicals and acetylene and is proportional to acetylene concentrations. Thus, helium is expected to have the maximum 1,3-butadiyne concentration followed by argon and nitrogen. Peak concentrations were 1000 ppm at one atmosphere and 360 ppm at eight atmospheres in the helium-diluted flame. Carbon dioxide is of interest as the concentrations of 1,3-butadiyne do not seem to decrease as observed with the three other

diluents; however the differences in the concentration values at two and eight atmospheres are small when compared to the other three diluents. Overall the concentrations of 1,3-butadiyne decrease with increase in pressure for three of the four diluents, which further confirms claim made in Abhinavam *et al.* (2013a): the reactions involved in the formation of 1,3-butadiyne (diacetylene) are completely different from that of 1,3-butadiene, and the concentrations are proportional to the trends observed with concentrations of acetylene.

Benzene (C_6H_6) is the fundamental building block all PAH and is of primary importance. Figure 4.2.17 shows the concentrations of benzene plotted for all four flames as a function of pressure. Again, the helium-diluted flame produced the highest concentration of benzene with 400 ppm and 630 ppm at one atmosphere and eight atmospheres, respectively. Whereas the carbon dioxide-diluted flame produced the lowest concentration with 70 ppm and 170 ppm at one atmosphere and eight atmospheres respectively. McEnally and Pfefferle (2000) investigated the effects of partial premixing in an ethylene-air diffusion flame and noticed that premixing had a positive effect on the amount of soot and precursor produced, due to the reactions with oxygen radical breaking the double and triple bonds in the hydrocarbons (McEnally and Pfefferle, 2000). This reaction involving O and O_2 could explain the significant amount of benzene produced in the helium-diluted flame, which was lifted and had a premixing region. Argon and nitrogen diluted flames, though not lifted, shared similar trends with those observed with the other hydrocarbon species measured, where argon producing marginally higher concentrations compared with the nitrogen diluted flames.

The heaviest of all the non-fuel hydrocarbons measured for this study was toluene (shown in Fig. 4.2.18). Toluene is a methyl substituted aromatic compound and an important soot precursor. The key compounds involved in the formation are benzene and acetylene. Because of this, it would be expected that the flame with the highest concentrations of benzene and acetylene would produce the most toluene. Measurements confirm this expectation, as the helium-diluted flame produced the most toluene with 18 ppm and 45 ppm at one atmosphere and eight atmospheres, respectively. In addition, as seen with the other hydrocarbons measured, CO_2 had the lowest concentration of toluene with argon and nitrogen falling in between.

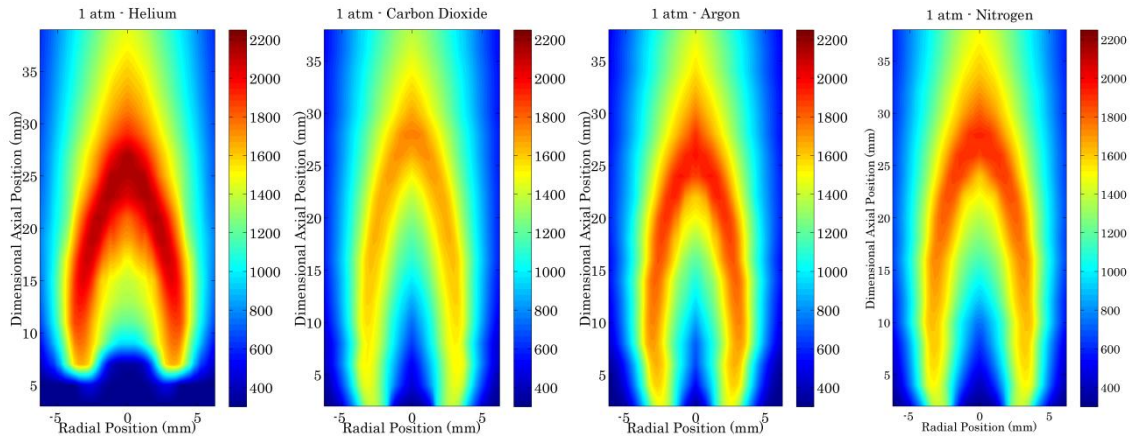


Figure 4.2.1. Temperature contours of four diluted flames at 1 atm

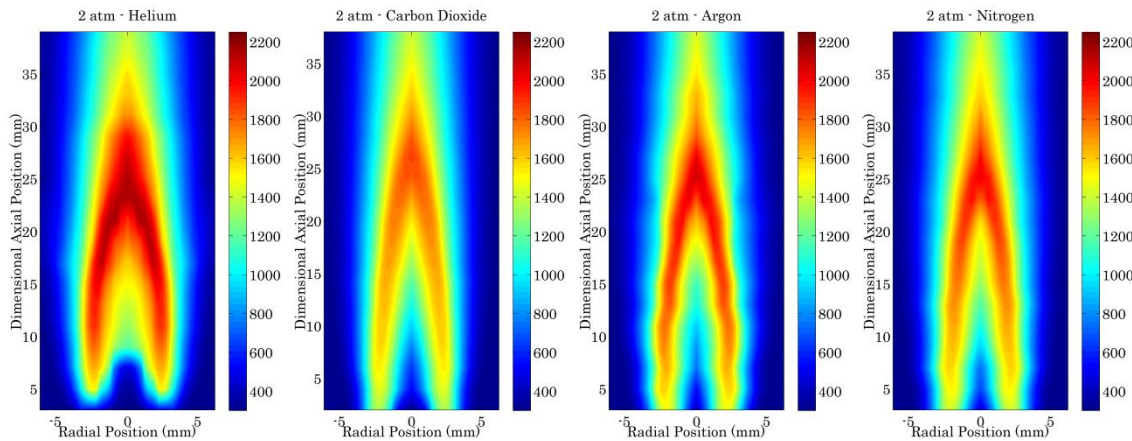


Figure 4.2.2. Temperature contours of four diluted flames at 2 atm

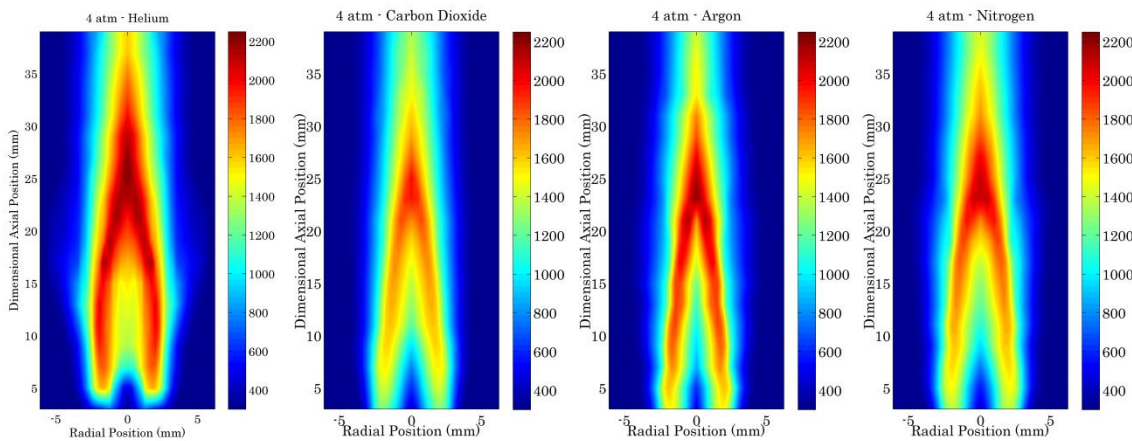
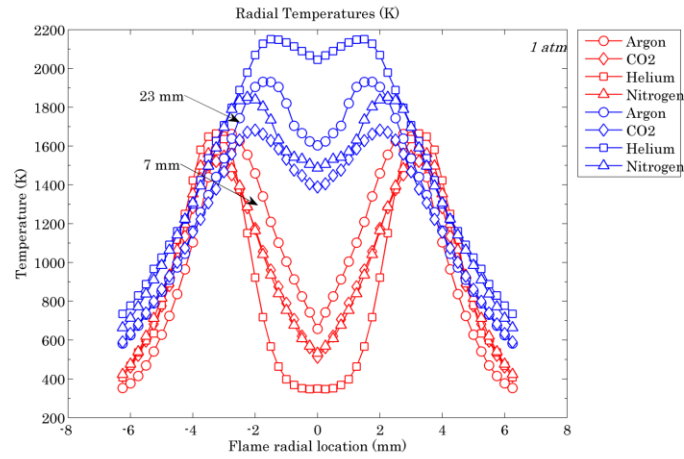
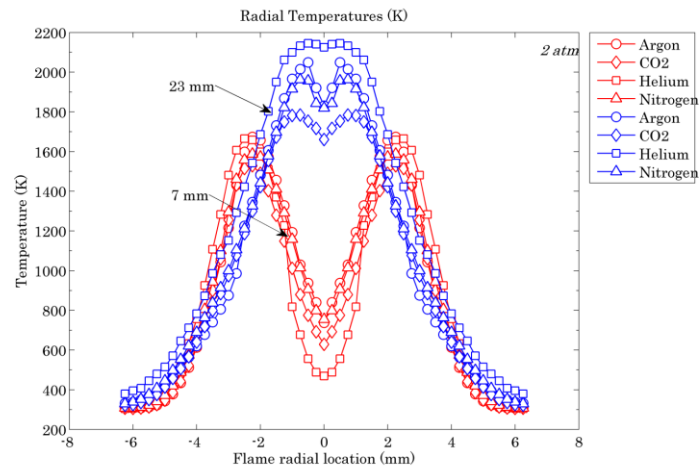


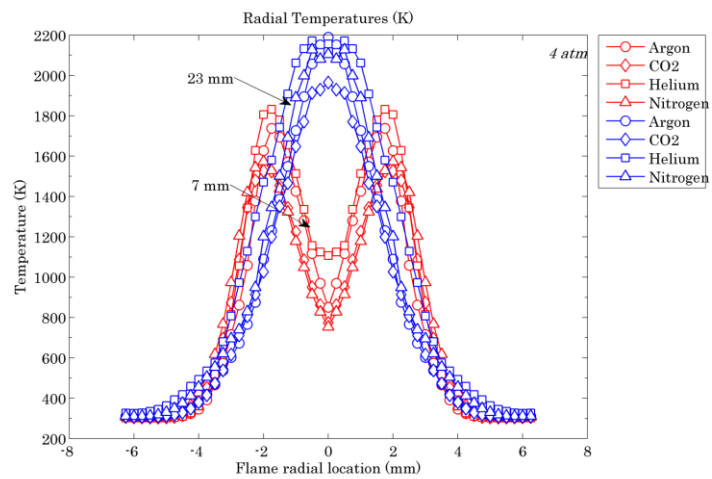
Figure 4.2.3. Temperature contours of four diluted flames at 4 atm



(a): Temperature profiles at one atmosphere



(b): Temperature profiles at two atmosphere



(c): Temperature profiles at four atmosphere

Figure 4.2.4. Temperature profiles along two radial sections along the flame

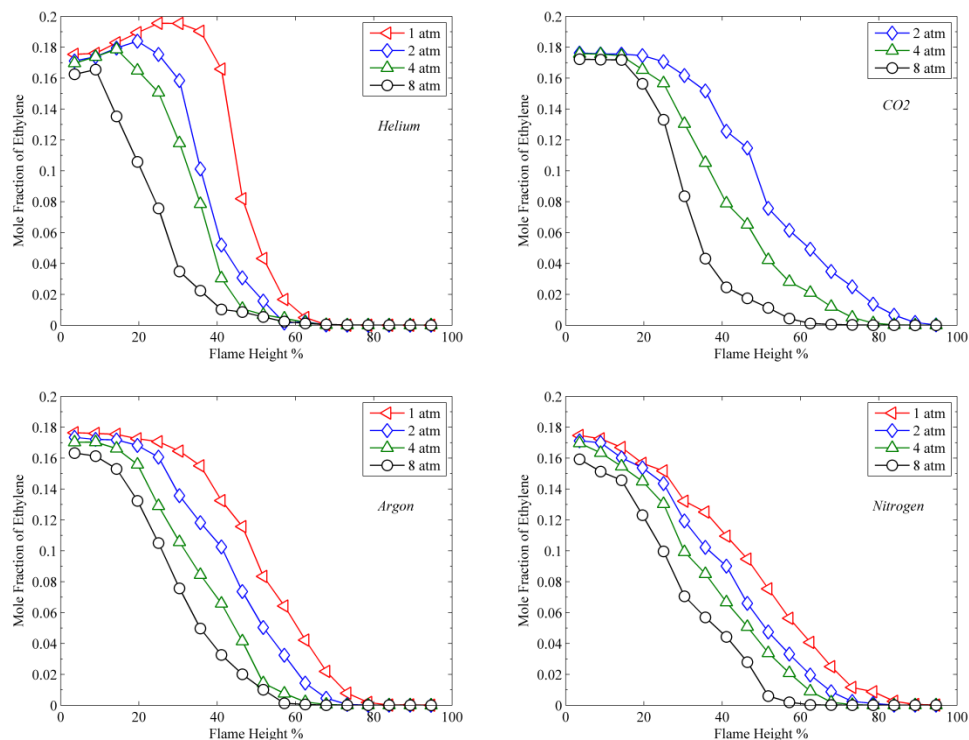


Figure 4.2.5. Mole fraction of ethylene as a function of pressure

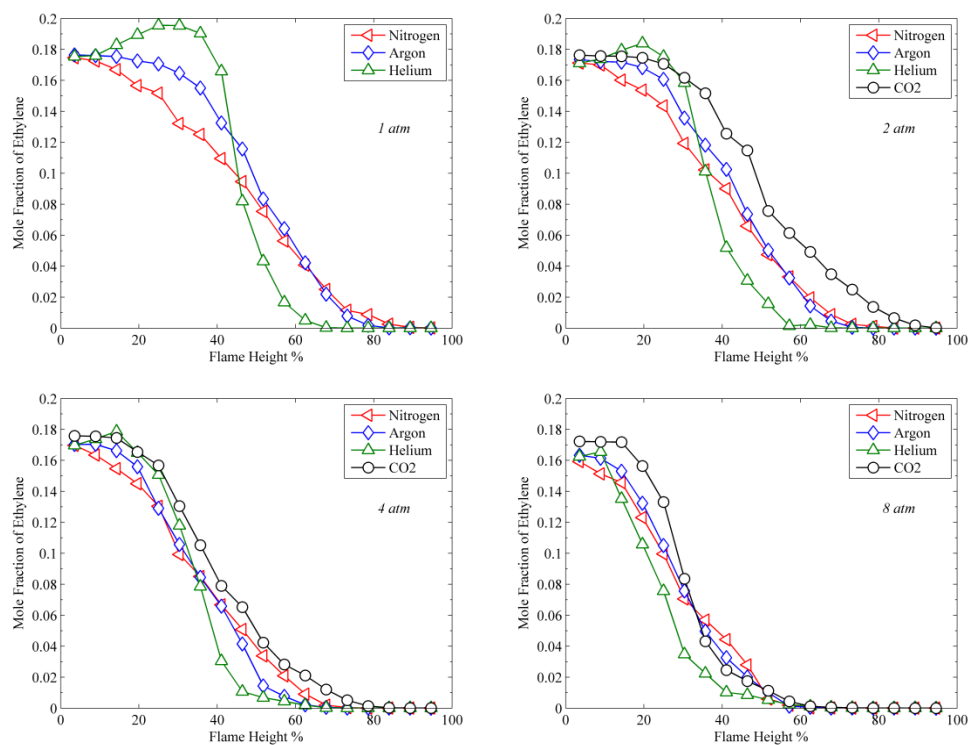


Figure 4.2.6. Mole fraction of ethylene as a function of diluent

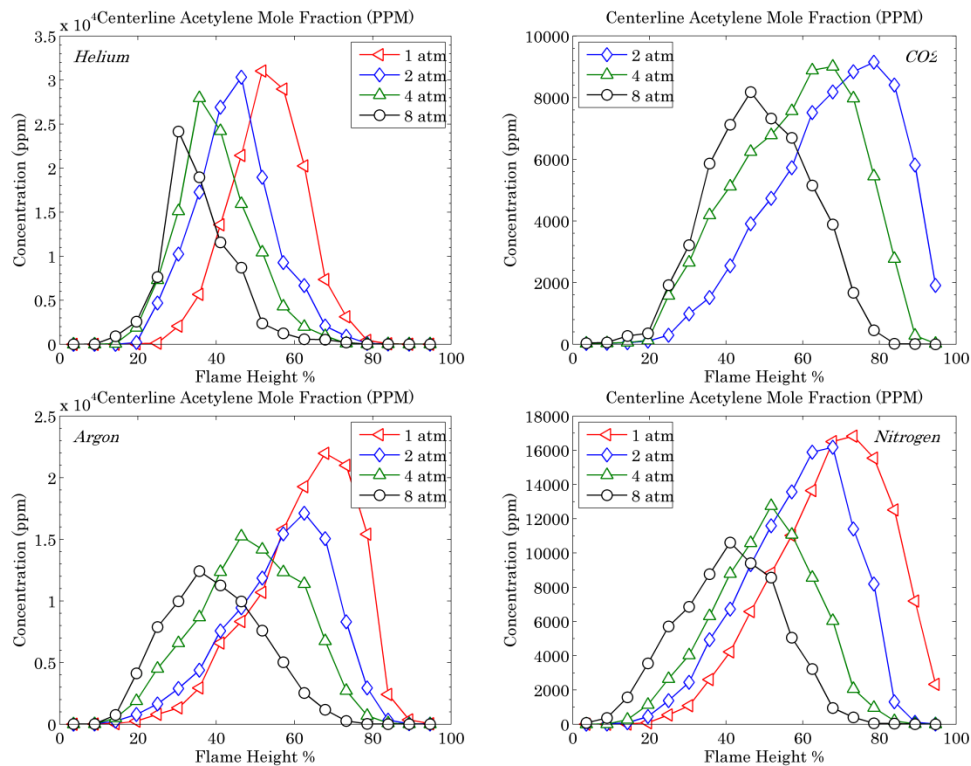


Figure 4.2.7. Concentrations of acetylene as a function of pressure

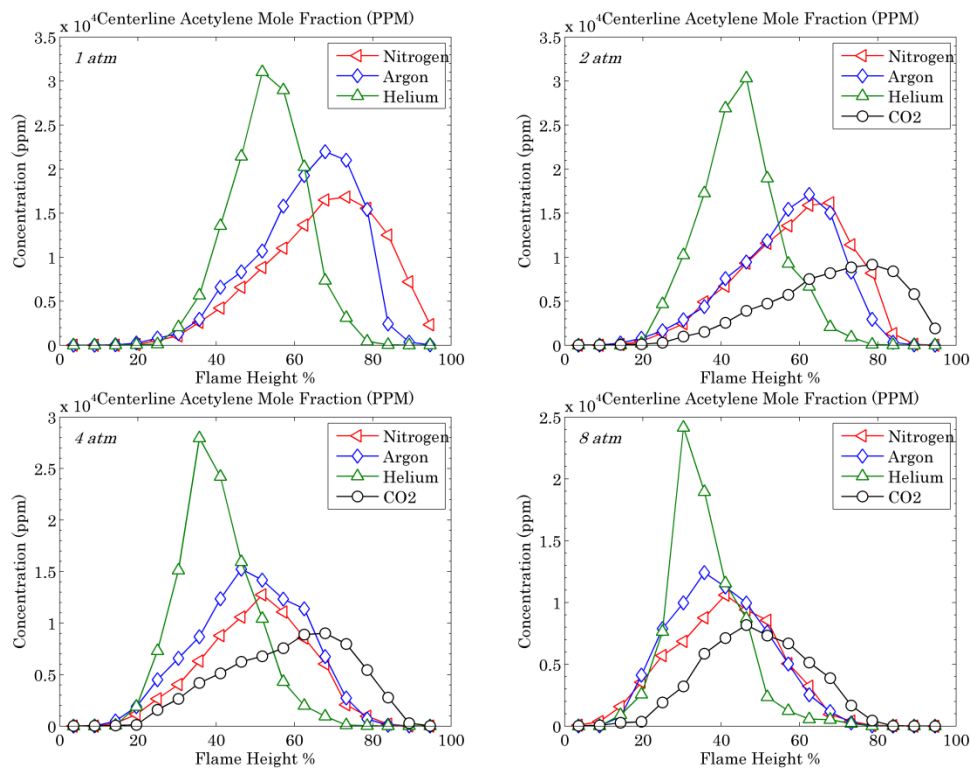


Figure 4.2.8. Concentrations of acetylene as a function of diluent

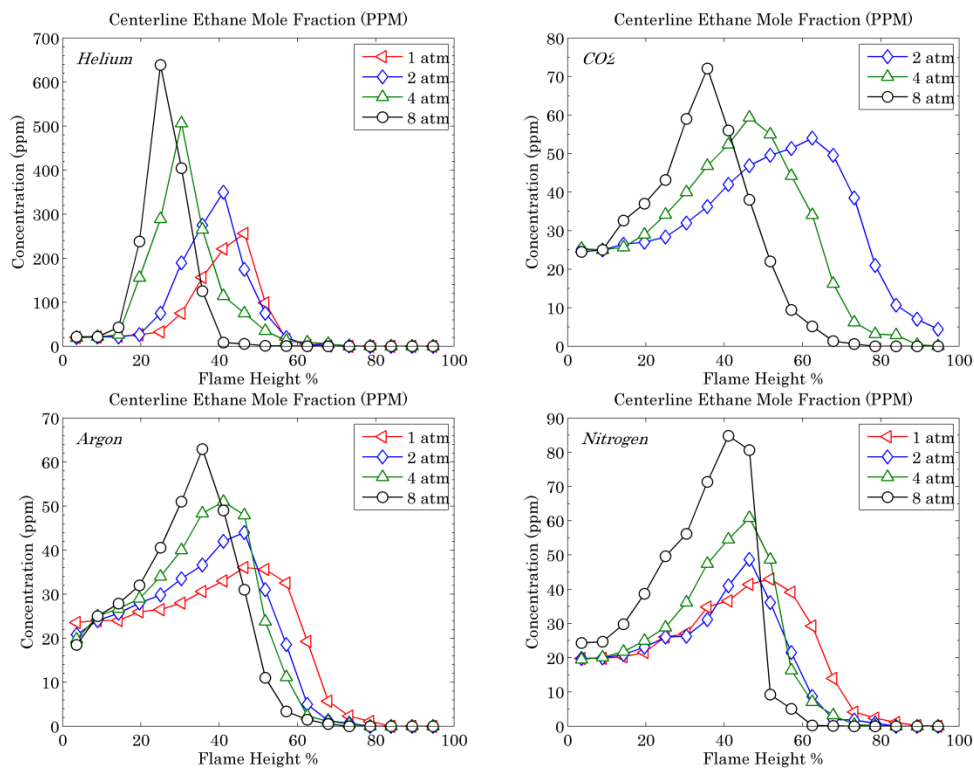


Figure 4.2.9. Concentrations of ethane as a function of pressure

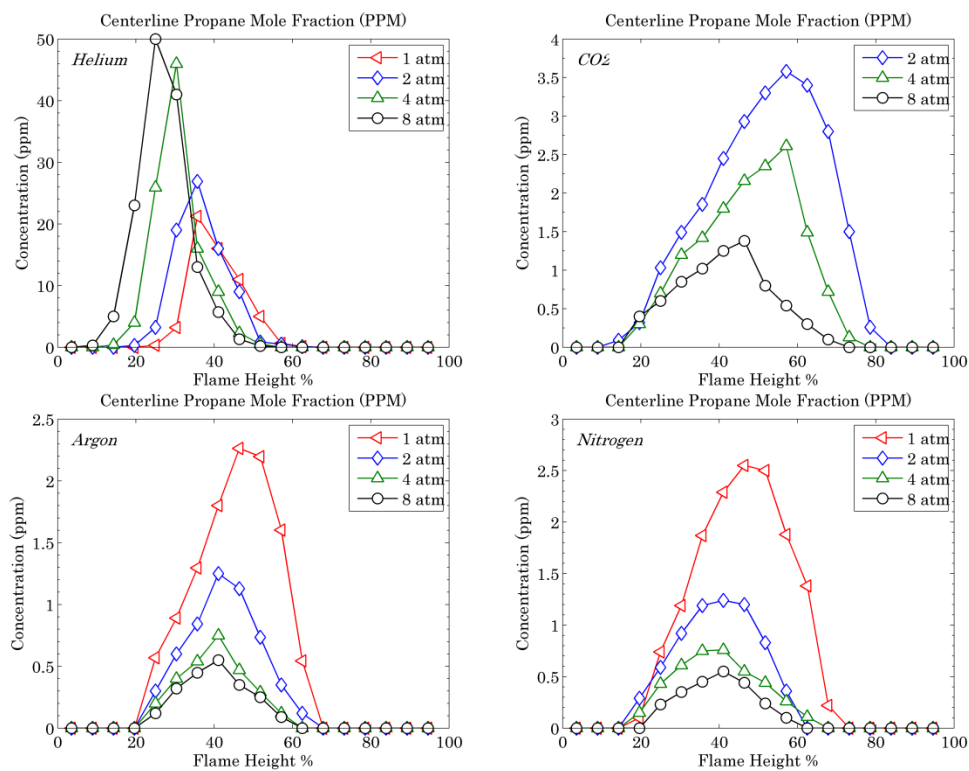


Figure 4.2.10. Concentrations of propane as a function of pressure

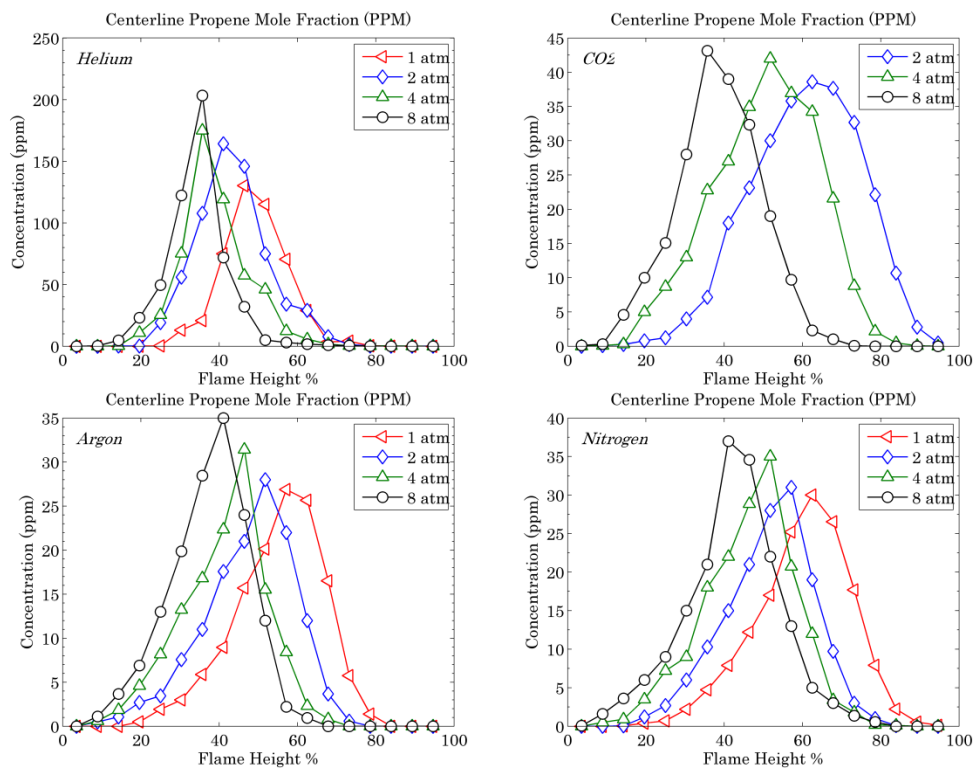


Figure 4.2.11. Concentrations of propene as a function of pressure

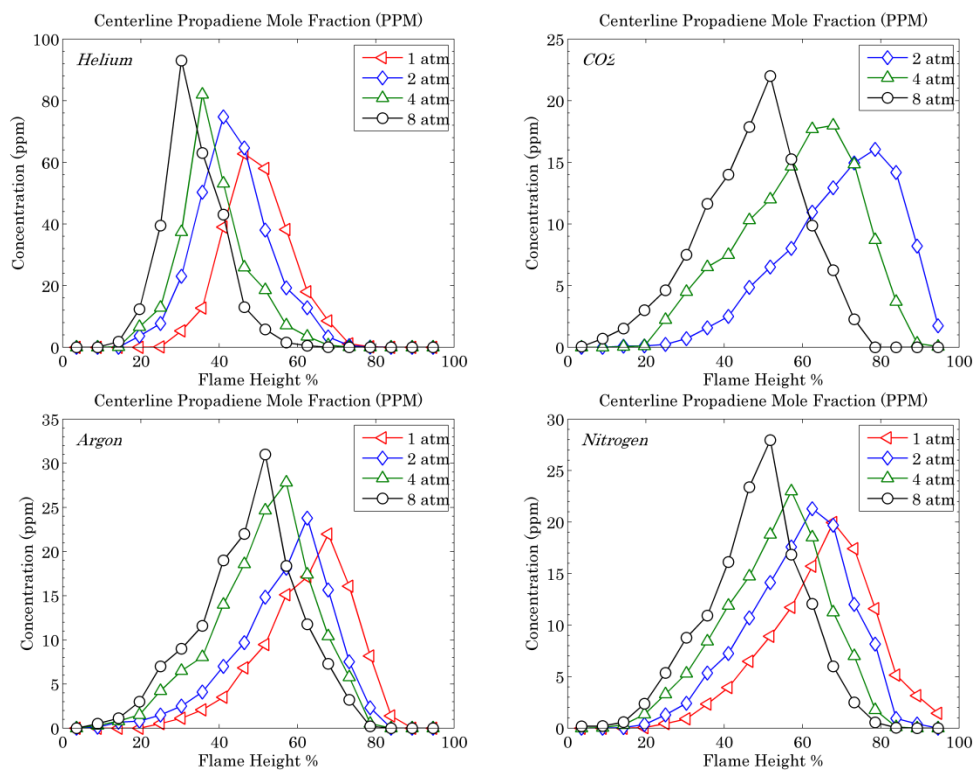


Figure 4.2.12. Concentrations of propadiene as a function of pressure

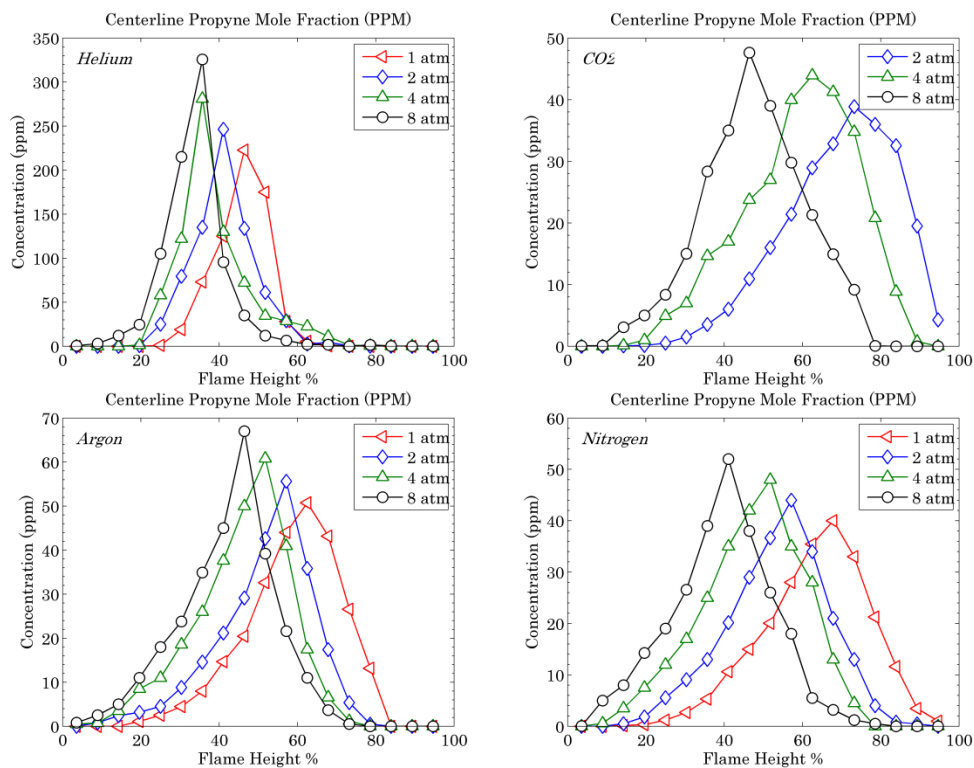


Figure 4.2.13. Concentrations of propyne as a function of pressure

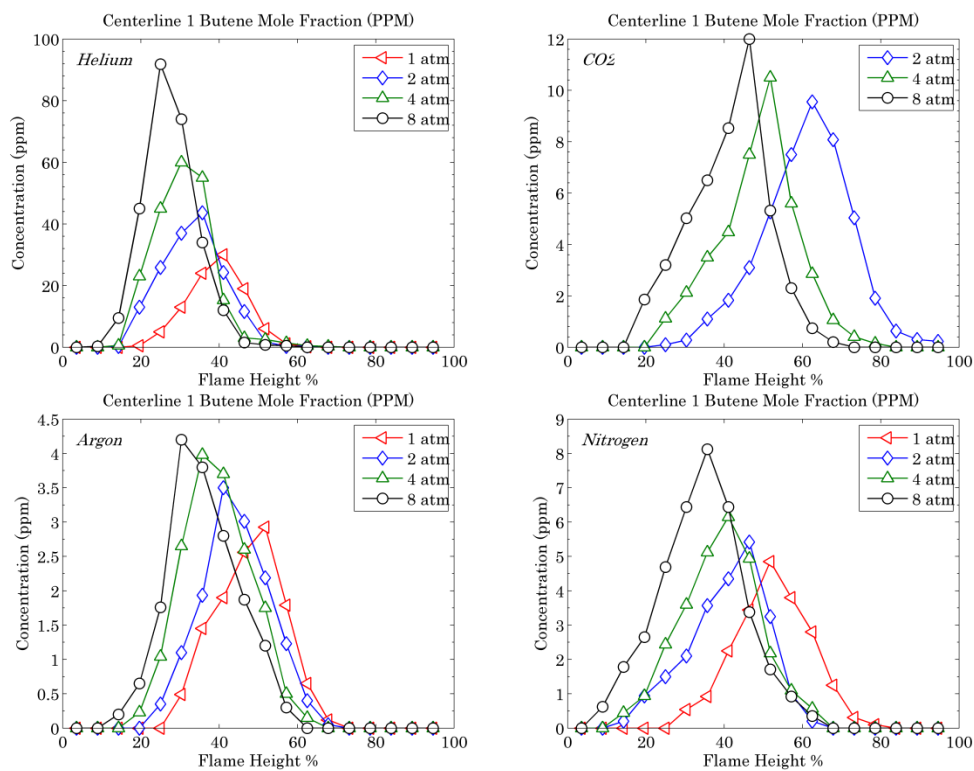


Figure 4.2.14. Concentrations of 1-butene as a function of pressure

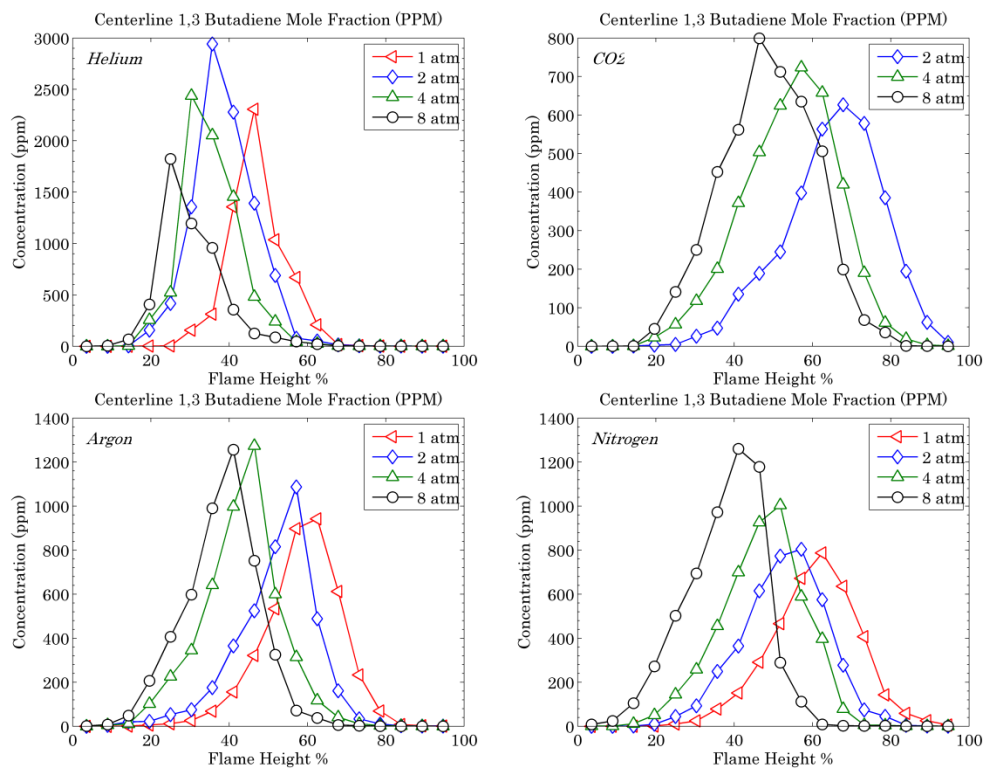


Figure 4.2.15. Concentrations of 1,3-butadiene as a function of pressure

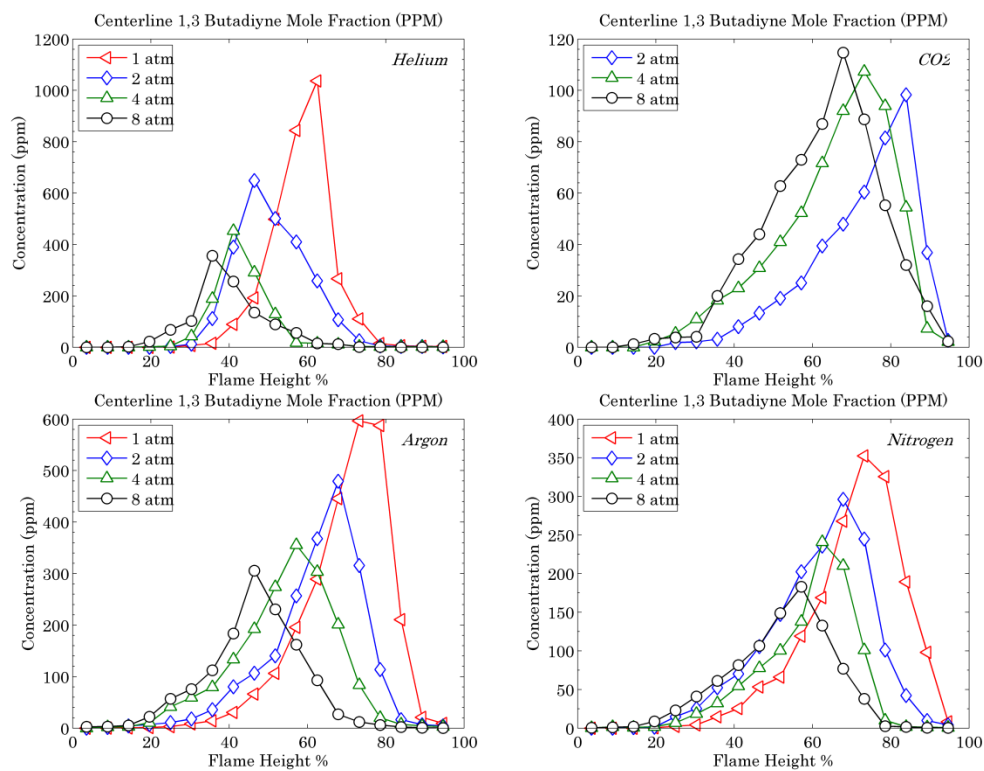


Figure 4.2.16. Concentrations of 1,3-butadiene as a function of pressure

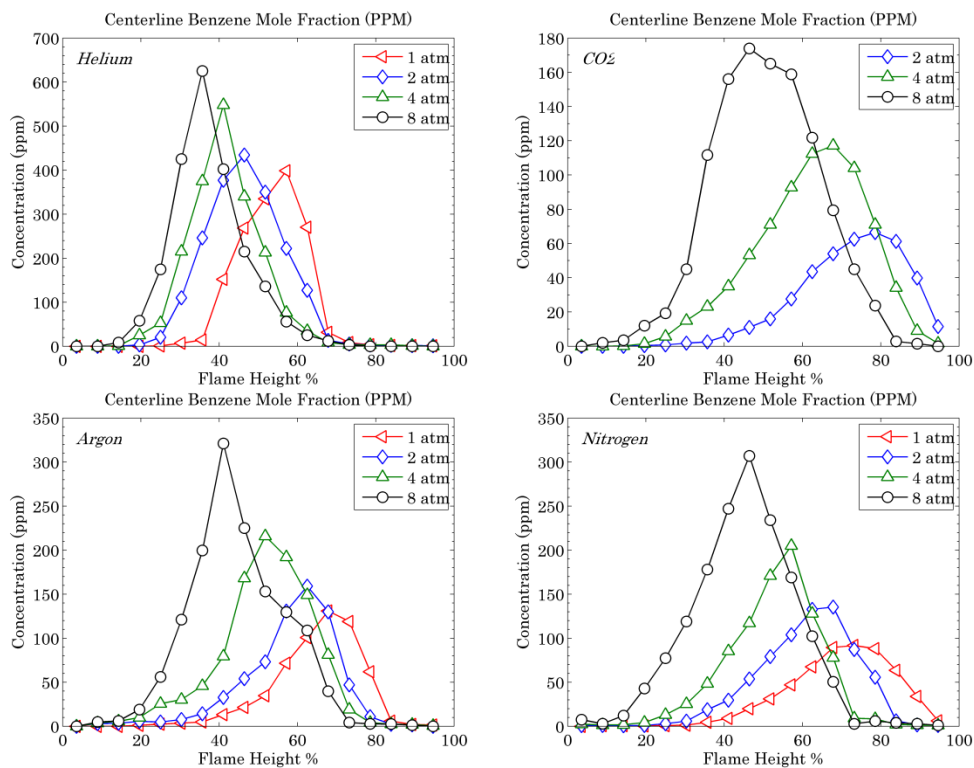


Figure 4.2.17. Concentrations of benzene as a function of pressure

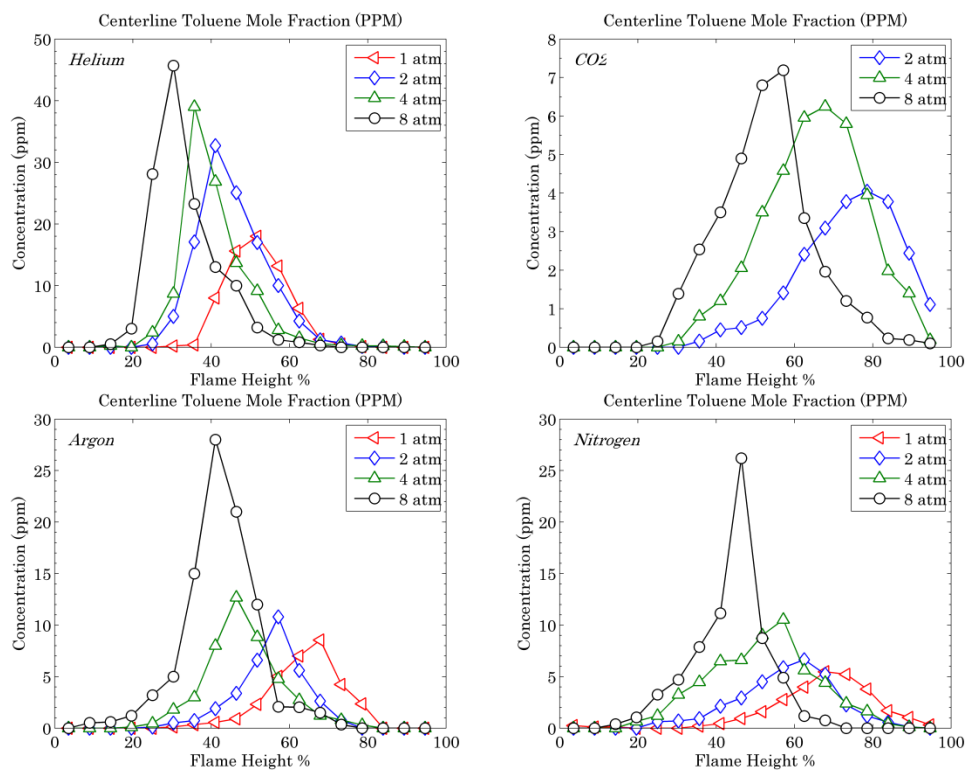


Figure 4.2.18. Concentrations of toluene as a function of pressure

4.3 Soot Surface Temperatures and Soot Volume Fractions in Ethylene Flames with Different Diluents with Two-color Pyrometry

The soot surface temperature results are presented first, followed by f_v results, for all flames. The trends in the various profiles will be examined in detail. There are no f_v measurements available in the published literature for an ethylene flame at this high of dilution level with the exception of Joo and Gülder (2011), who conducted experiments on an 83% nitrogen diluted ethylene diffusion flame, however, with fuel flow rate 1/5th of that used in this current study. They reported radially resolved f_v measurements. Their flames were 5.5 mm tall, which is roughly 1/5 the height measured in this study. The axes on the figures correspond to the pixel numbers of the figure. All flames are represented with reference to the fuel tube exit, which is denoted by a horizontal white line, and provides a physical frame of reference. The two-color temperature data are compared to the thermocouple temperature measurements from Abhinavam Kailasanathan *et al.* (2013b) for certain conditions. The peak f_v are expected to occur at the tip and move towards the wings of the flame with pressure, whereas lowest f_v should occur along the centerline of the flame. Since the reported results are line-of-sight averaged values, it cannot be discerned in the flames with low f_v , but appear at 8 atm where the f_v are highest for the respective diluents. This is consistent with many researchers (Santoro *et al.*, 1983; Santoro and Semerjian, 1984) and agrees with the theory that in diffusion flames soot forms near the fuel side of the reaction zone with the (nearly) soot free region extending along the centerline.

Figures 4.3.1-4.3.4 show temperature contours from 1 to 8 atmospheres for ethylene flames diluted with four diluents (helium, argon, nitrogen, carbon dioxide). The plots are arranged in order of increasing pressures moving from left to right. It should be noted again that the dilution level for carbon dioxide flames was 78%, whereas helium, argon and nitrogen flames were diluted 82.5 % by volume. We see that the soot surface temperatures decrease with an increase in pressure whereas the f_v are seen to increase with pressure.

The soot surface temperature in nitrogen diluted flames measured using two-color pyrometry has a peak value of 2110 K at 1 atmosphere (Fig. 4.3.1a). CET (Chemical equilibrium with transport properties) code (Gordon and McBride 1971) was used to calculate equilibrium adiabatic flame temperatures. Equilibrium calculation yields an adiabatic flame temperature of 2133 K, which is in good agreement for these low soot loadings. The adiabatic flame temperature at 8 atmosphere increases slightly to 2163 K. But the measured flame temperatures decrease to 1870 K, which is almost a 240 K difference. The measured flame temperatures are a direct function of the radiation intensity, which is related to the soot loading in flames. Since soot yield increases dramatically with pressure, the heat loss due to soot radiation also increases resulting in lower temperatures and this large discrepancy between adiabatic calculation and actual soot surface temperature is not surprising at the elevated pressures for flames with high f_v .

The measured peak soot surface temperature for argon diluted flames is about 2200 K, 100K higher than nitrogen at 1 atmosphere (Fig. 4.3.2). The measured temperatures at 2, 4 and 8 atmospheres are 2180 K, 2080 K and 1920 K, respectively. The soot surface temperatures of the helium diluted flames are shown in Fig. 4.3.3. It should be noted that the helium flames at the current dilution levels are lifted for all four pressures investigated. Given the fact that the binary diffusion coefficient of helium is the highest among the four diluents tested, the helium added to the fuel stream diffuses away rapidly as the mixture exits the fuel tube, leaving relatively higher concentrations of ethylene in the lifted region (Abhinavam Kailasanathan *et al.* 2013b). This is a

possible reason for the higher flame temperatures measured with helium, about 2300 K at 1 atmosphere, while the calculated adiabatic flame temperature is 2267 K, which is the highest recorded temperature of all the four flames. The corresponding measured temperature values at 2 and 4 atmospheres are 2270 K and 2190 K, respectively. At 8 atm, the radiation loss due to increased soot loading results in a temperature of about 2000 K, a reduction of 300 K compared with atmospheric pressure and the largest difference among the four diluents.

The carbon dioxide diluted flame is different from the other three flames in terms of dilution and fuel flow rates. Reactant flow rates similar to the previous three diluents yielded a blue flame with no significant flame luminosity even at 4 atmospheres, and is not amenable to the two-color technique due to the lack of sufficient signal strength. In order to obtain a flame with sufficient luminosity, the dilution level was reduced. With reduced level, the flame height also decreased (McEnally and Pfefferle, 2000). To compensate for this flame height reduction, the fuel flow was increased to 85 sccm, with a resulting diluent flow rate of 315 sccm, yielding a flame with a height similar to the other 3 diluents. Even at this dilution level, there was insufficient signal to noise to permit atmospheric pressure pyrometry, and only 2, 4, and 8 atm data is reported.

Figure 4.3.5 shows the peak flame temperatures of these diluted ethylene flames plotted as a function of pressure. The decrease in flame temperature due to heat loss from enhanced soot radiation is immediately apparent. To better understand the effects of the different diluents on flame temperature, the transport properties are plotted as a function of the measured soot surface temperature at 8 atm (Fig. 4.3.6). It is evident the flame temperatures increase as the molar specific heat capacity of the diluents decreases, as expected. Even though argon and helium (both chemically inert and monoatomic) share similar heat capacities, the fact that helium has significantly higher temperatures suggests that the large differences in the thermal diffusivity between these two inerts may be responsible.

Figure 4.3.7 shows the line of sight integrated f_v of the nitrogen diluted flame as a function of pressure. Note that the color scale is different for each image due to the large changes in peak values as a function of pressure. It can be clearly seen that there is almost no soot at one atm, with a calculated peak soot volume fraction of ~ 0.015 ppm at the tip of the flame. Results from Abhinavam Kailasanathan *et al.* (2013a) showed that the primary precursors essential for soot formation (benzene, acetylene) were still present in significant amounts at the tip, suggesting incompleteness of the reactions necessary for soot formation. At 2 atm, a gradual growth of the sooting region and an increase in peak soot volume fractions to 0.4 ppm is observed. Due to the growth in the luminous region, the measured temperature profiles also extend further down when compared to the one atm profiles. At 4 atmospheres, the sooting region is larger still and appreciable soot appears further down in the wings of the flame. The peak f_v is 1.8 ppm, significantly greater than the 2 atm case, and still occurs at the tip region. At 8 atm a peak f_v of 7 ppm is measured. This 8 atm flame result is roughly comparable to the results by Joo and Gülder (2011), who measured a local peak concentration of 8 ppm in much smaller ethylene diffusion flame at 10 atm using a line of sight soot spectral emission technique (SSE). Joo and Gülder (2011) report radially resolved data; so only peak values can be compared between the cases.

Soot volume fraction in both argon and helium diluted flames were measured at 1, 2, 4 and 8 atm, at conditions identical to flames used in previously reported (Abhinavam Kailasanathan *et al.*, 2013a) major hydrocarbon species measurements via sampling and GC/FID. Argon and nitrogen share similar physical properties even though one is diatomic and

the other is monoatomic, with nitrogen's specific heat capacity twice that of argon's. The previous hydrocarbon species measurements showed that even though they shared similar physical properties, the argon diluted flames produced significantly higher concentrations of all the major soot precursors. The result of these higher concentrations is higher soot loading, which is clearly evident when comparing f_v in argon (Fig. 4.3.8) and nitrogen diluted flames. At 1 atmosphere, the argon diluted flame has a peak f_v of 0.06 ppm as opposed to nitrogen with an almost negligible value of 0.015 ppm. The peak values of f_v occur at the tip, similar to nitrogen. At 2 atm in the argon diluted flame, the luminous region almost extends to the fuel tube exit. The peak f_v again occurs around the flame tip with a value of 0.7 ppm. The f_v increases to a peak value of 5.5 ppm at 4 atm, with larger quantities of soot occurring in the wing regions than the 2 atm case. Peak f_v occurs for the first time at the wings rather than at the flame tip. With increasing pressure, the peak f_v region migrates closer to the flame base. The f_v is 15.5 ppm at 8 atm, more than twice that of the nitrogen diluted flame at the same pressure. Furthermore, the luminous zone extends all the way to the fuel tube exit.

The f_v peaks at 1.4 ppm at 1 atm for the helium diluted flame, Fig. 4.3.9, which is the highest among the four diluents. In the helium diluted flame at 2 atm, the sooting region extends towards the flame base and soot concentration increases with a peak f_v of 4.2 ppm. The reduction in flame cross-sectional area is prominent at 4 atm as is the reduction of lift-off height with an increase in pressure. The peak f_v is 12.3 ppm. At 8 atm, the flame is still lifted with the lift-off height just about 3 mm. A maximum measured f_v of 53 ppm is observed in this case. There are two possible reasons for such high soot concentrations in these helium diluted flames. Firstly, there is an abundance of soot precursors formed due to a large concentration of fuel caused by the higher mobility of helium relative to fuel and thus an effective reduction in the dilution level. These elevated species levels were first reported in Abhinavam Kailasanathan *et al.*, (2013a). Secondly, McEnally and Pfefferle (2000) found that partial premixing increases soot formation due to the presence of O radical when they investigated the effects of premixing in ethylene and other hydrocarbon flames. The helium flame in this study, as it is lifted, inherently undergoes partial premixing resulting in higher soot concentrations.

Figure 4.3.10 shows the carbon dioxide diluted flame at 2, 4 and 8 atm, with the lowest f_v among all the diluents, even with the 20% increase in fuel flow rates, at 0.025 ppm at 2 atm. The f_v increases to approximately 1 ppm at 8 atm. These very low f_v values are due to both a thermodynamic effect of the high heat capacity and the role CO_2 plays in soot chemistry. Previous measurements of benzene, for example, in these flames showed that the peak concentration in the CO_2 -diluted flame was approximately $\frac{1}{2}$ that of both N_2 and Ar (160 ppm vs 300+ ppm respectively), while the peak f_v was approximately $\frac{1}{7^{\text{th}}}$ that of N_2 and $\frac{1}{15^{\text{th}}}$ of Ar. This would indicate that the lower f_v is due more to enhanced soot oxidation rather than suppressed formation.

Figure 4.3.11 shows the peak f_v in ppm measured alongside data from the undiluted ethylene flame of McCrain and Roberts (2005). f_v at 8 atmospheres for the helium diluted flame is $\frac{1}{3^{\text{rd}}}$ that of the peak f_v measured in the undiluted flame. The helium diluted flame has the highest peak f_v at all pressures whereas the carbon dioxide flame has the lowest peak f_v measured. When comparing peak f_v values between 4 and 8 atms, there is a dramatic difference in the slope between carbon dioxide and helium, indicating the soot suppressing tendencies of the diluents used. This trend is similar to the soot precursor concentrations presented in Abhinavam Kailasanathan *et al.* (2013b).

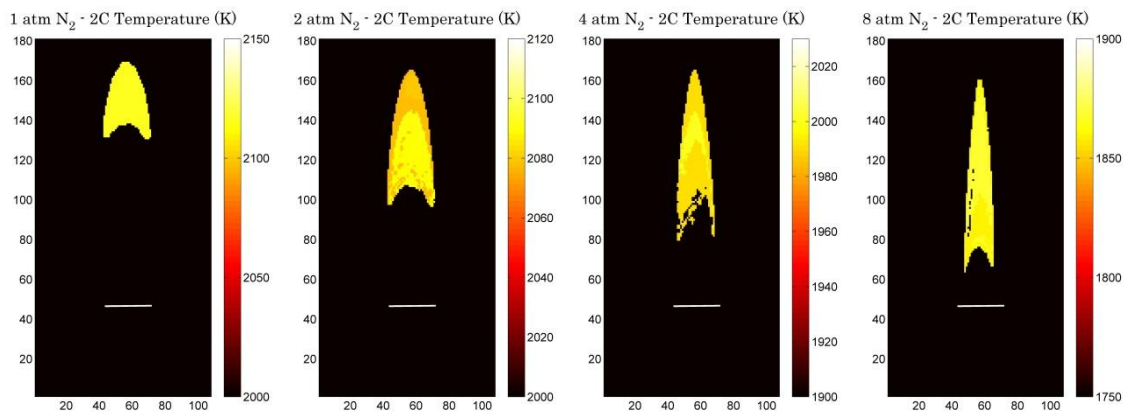


Figure 4.3.1: Two color temperature profiles for nitrogen diluted flames

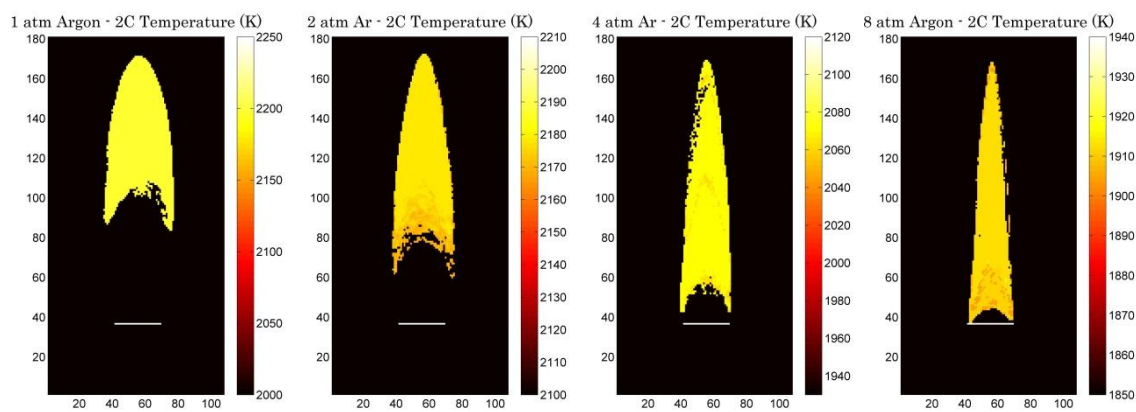


Figure 4.3.2: Two color temperature profiles for argon diluted flames

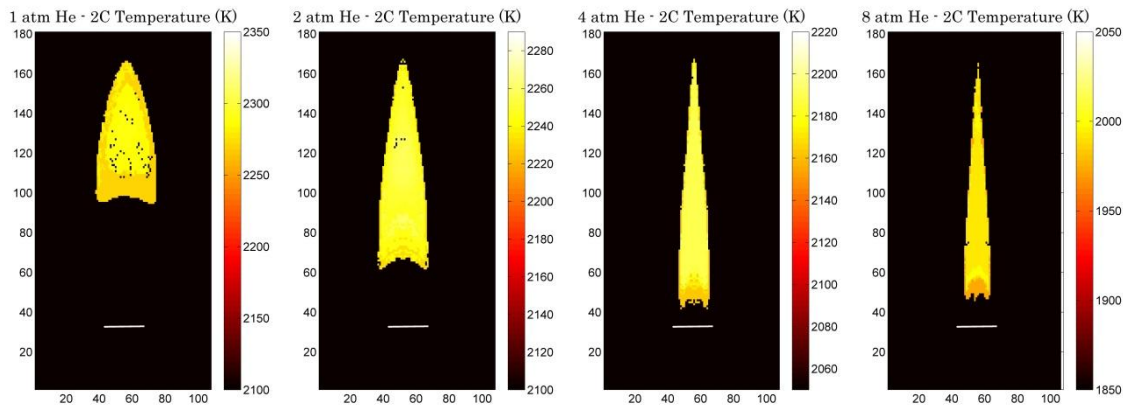


Figure 4.3.3: Two color temperature profiles for helium diluted flames

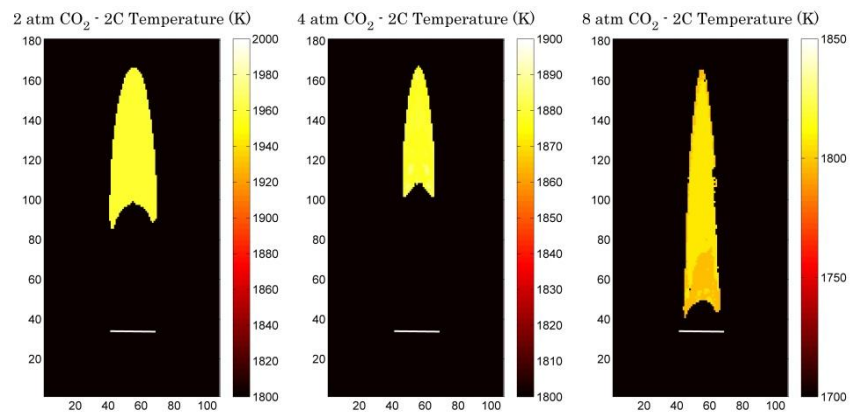


Figure 4.3.4: Two color temperature profiles for carbon dioxide diluted flames

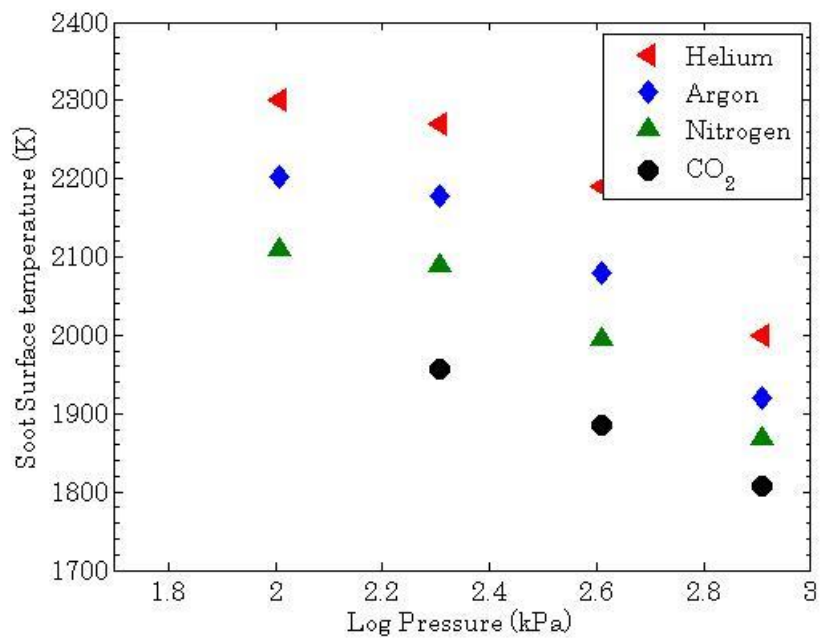


Figure 4.3.5: Peak soot surface temperatures as a function of pressure

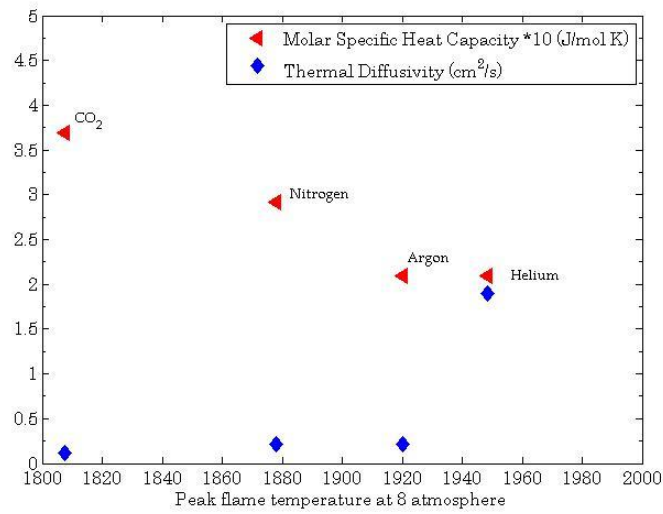


Figure 4.3.6: Peak soot surface temperatures plotted against transport properties

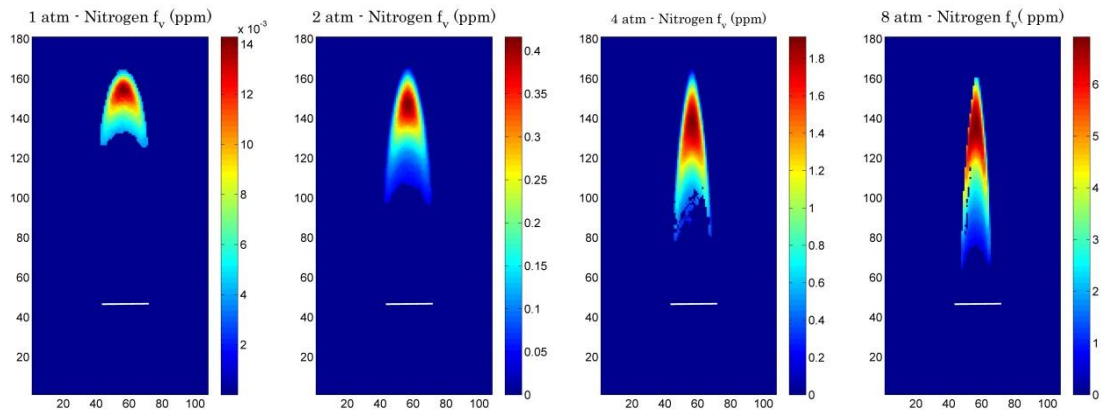


Figure 4.3.7: Soot volume fraction (ppm) profiles for nitrogen diluted flames

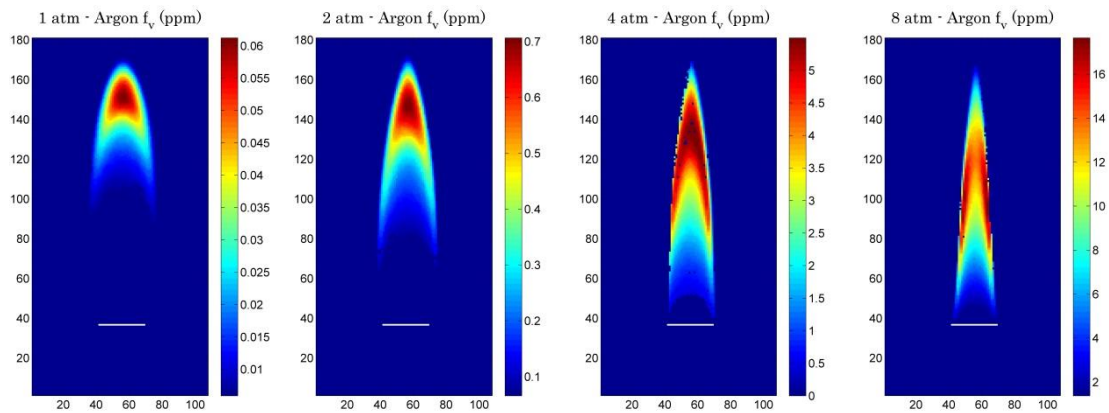


Figure 4.3.8: Soot volume fraction (ppm) profiles for argon diluted flames

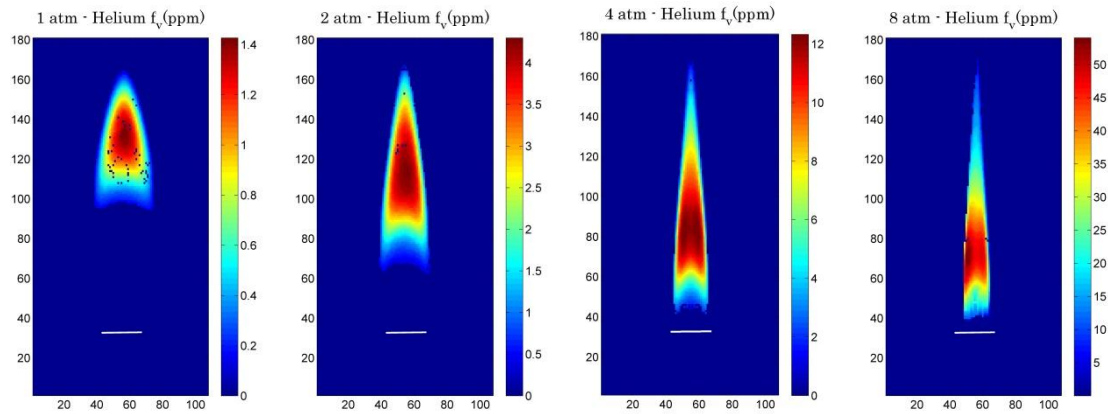


Figure 4.3.9: Soot volume fraction (ppm) profiles for helium diluted flames

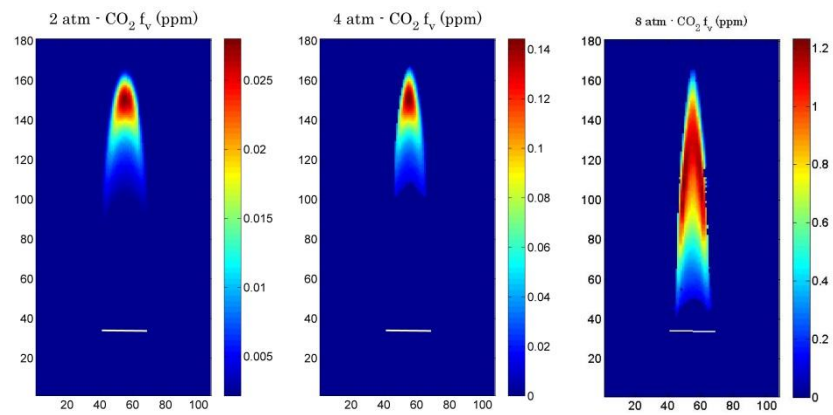


Figure 4.3.10: Soot volume fraction (ppm) profiles for carbon dioxide diluted flames

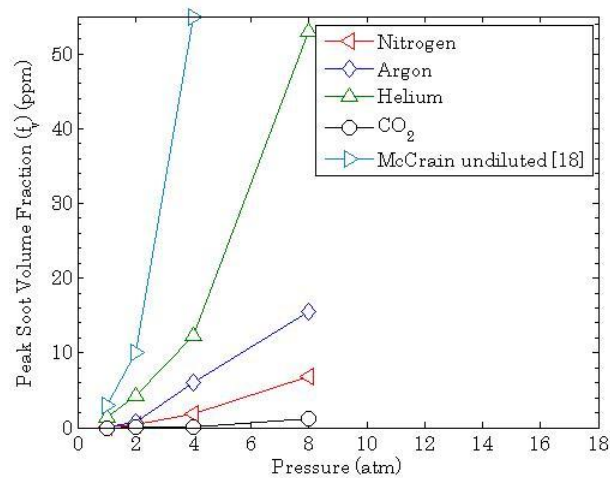


Figure 4.3.11: Peak soot volume fraction (ppm) versus pressure

4.4 Results of Laser Extinction and Scattering

4.4.1. Soot Volume Fraction

Transmission data was first smoothed and centered to account for slight angle of the flame or burner translation and to improve the stability of the Abel inversion. Transmissivity of the left and right halves of the flames are shown in Fig. 4.4.1.

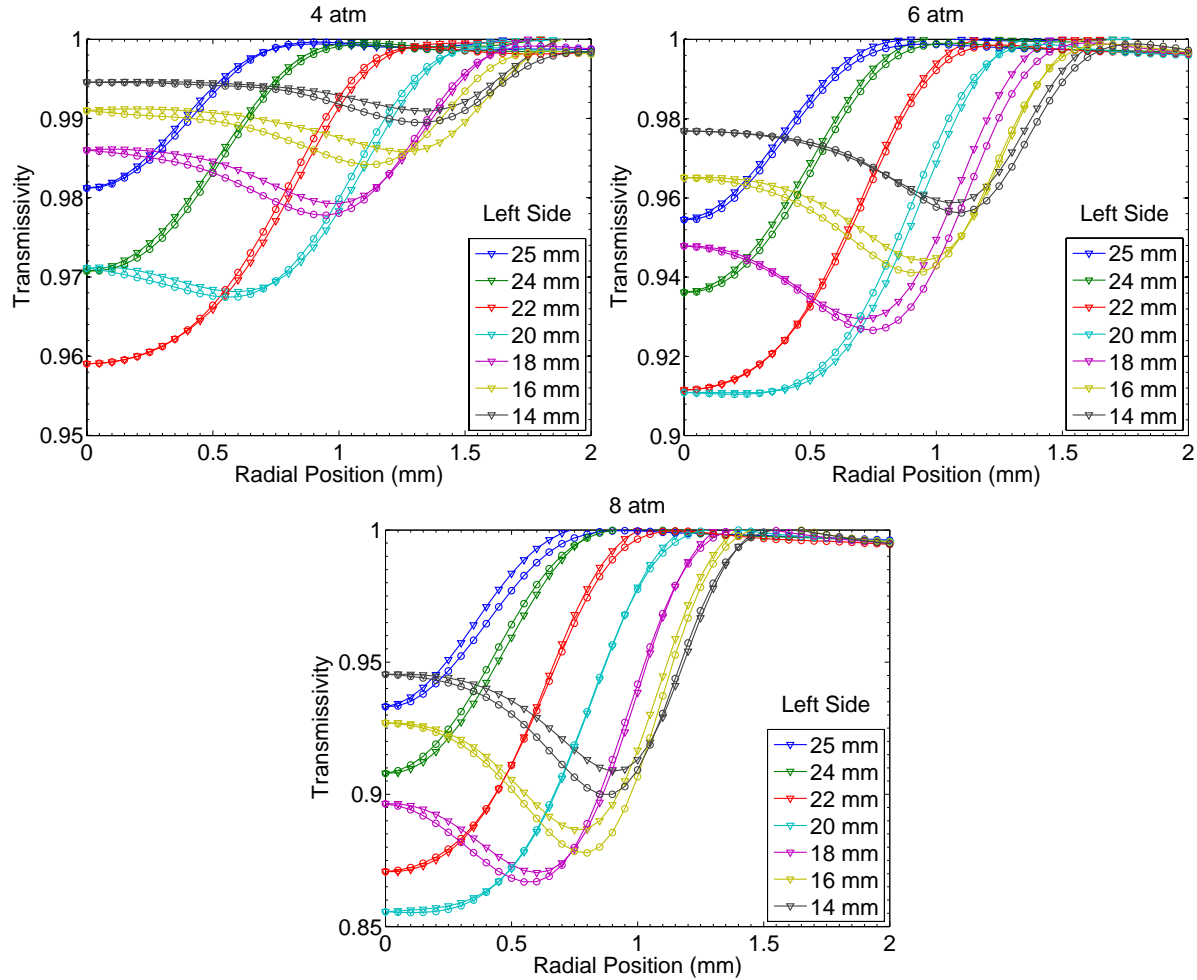


Figure 4.4.1: Transmissivity of left and right halves of flames at 4, 6, and 8 atm

They show good overall symmetry, which can also be seen in the contour plots of extinction ($-\ln(\tau)$), shown in Fig. 4.4.2.

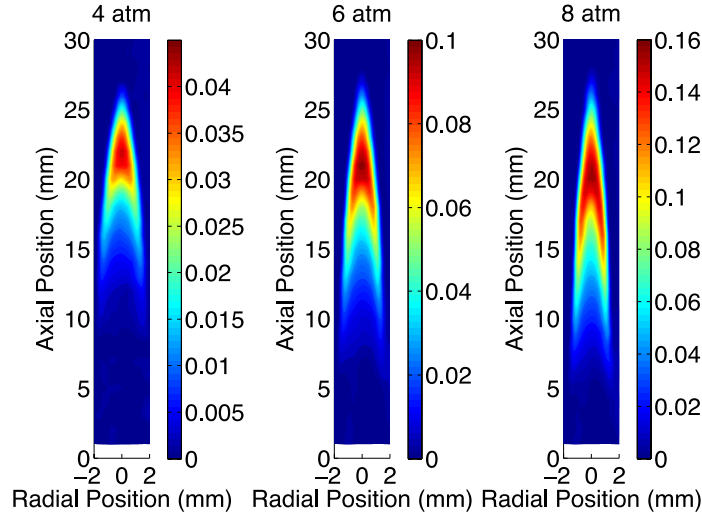


Figure 4.4.2: Extinction in flames at 4, 6, and 8 atm.

As is evident in the figures, the flame height remains constant as pressure increases, while it does narrow. From the integrated extinction measurements, integrated soot volume fraction can be calculated. Integrated f_v is shown for 4, 6, and 8 atm in Fig. 4.4.3.

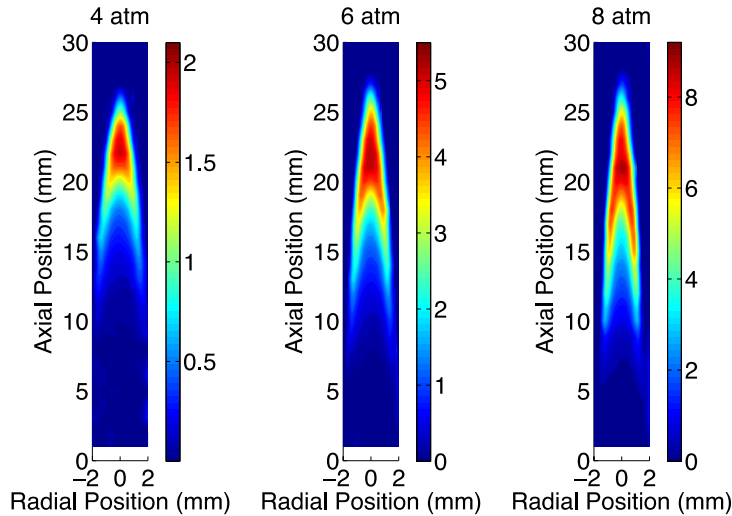


Figure 4.4.3: Integrated f_v at 4, 6, and 8 atm

Peak integrated soot volume fraction was seen to be 2.0 ppm at 4 atm, in good agreement with previous two-color measurements (1.8 ppm). At 8 atm, peak integrated f_v is measured as 8.9 ppm, about 25% higher than previous measurements. One reason for this could be the possibility of signal trapping in the two-color measurements. Peak extinction in the 8 atm flame was seen to be about 16%, meaning there is up to 16% signal trapped when measuring radiative flame emissions. This would result in two-color pyrometry underpredicting f_v . Additionally, the peak integrated f_v is much more localized in these LOSA measurements, the distribution of integrated f_v is much closer to those of the two-color measurements. Regardless, the differences in measurements are within experimental uncertainties, especially those resulting from difference in index of refraction. If this data is fitted with a power law, peak integrated f_v scales with pressure as $P^{2.2}$.

After performing an Abel inversion, the radial distribution of f_v was calculated. Since Abel error propagates towards flame centerline, concentrations separately calculated for the left

and right halves of the flame do not match at the center. The local f_v from the left and right halves of the flame are averaged and mirrored for better visualization. Contours of local f_v at 4, 6, and 8 atm are shown in Fig. 4.4.4.

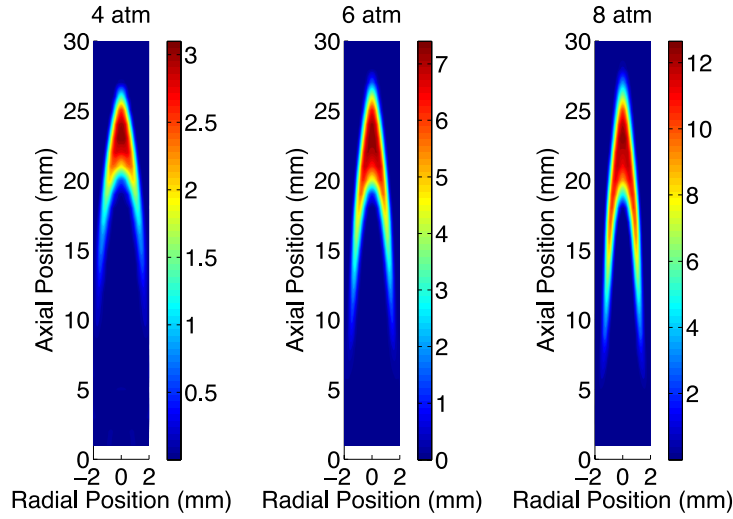


Figure 4.4.4: Local f_v contours at 4, 6, and 8 atm

The trends observed are similar to those observed by others. An increase in pressure results in narrowing of the flame, and a non-linear scaling of f_v . Local f_v peaks at 3.1, 7.3, and 12.6 ppm at 4, 6, and 8 atm, respectively. Soot also starts to appear in heavier relative concentrations lower in the flame, in the annulus. For a more detailed look at soot concentrations, local f_v is shown in radial profiles at different heights for 4, 6, and 8 atm in Fig. 4.4.5.

Error bars in these figures represent the combined uncertainties in each detector, the Abel inversion, averaging of left and right half profiles, and soot index of refraction. The results show the same trends as those observed by Joo and Gülder (2011). Starting near the flame base, the soot volume fraction slowly increases as the annulus diameter shrinks. At about 75% flame height, there is a rapid increase in f_v along the centerline, and profiles of f_v have a near constant slope above this height.

One method of visualizing the effect of pressure on soot formation is to determine the fraction of fuel carbon that is converted to soot as a function of axial position, z (Flower and Bowman, 1986; Thomson, 2004; Thomson *et al.*, 2005; Joo and Gülder 2011). In order to accomplish this, the mass flowrate of soot, m_s is determined from

$$\dot{m}_s = v_z(z) \rho_s \int 2\pi f_v(r, z) dr$$

where ρ_s is the density of soot, taken to be 1.8 g/cm^3 , and axial velocity, v_z , is reasonably approximated by

$$v_z(z) = \sqrt{2\alpha z}$$

as in (Thomson 2005; Thomson, 2005; Joo and Gülder 2011). The value of the acceleration constant, α , is taken to be 25 m/s^2 , but does not strongly affect the result of the approximation (Roper *et al.*, 1977). The soot carbon flowrate is then normalized by the fuel carbon flowrate at the fuel tube exit. Figure 4.4.6 shows the percent of fuel carbon converted to soot for 4, 6, and 8 atm.

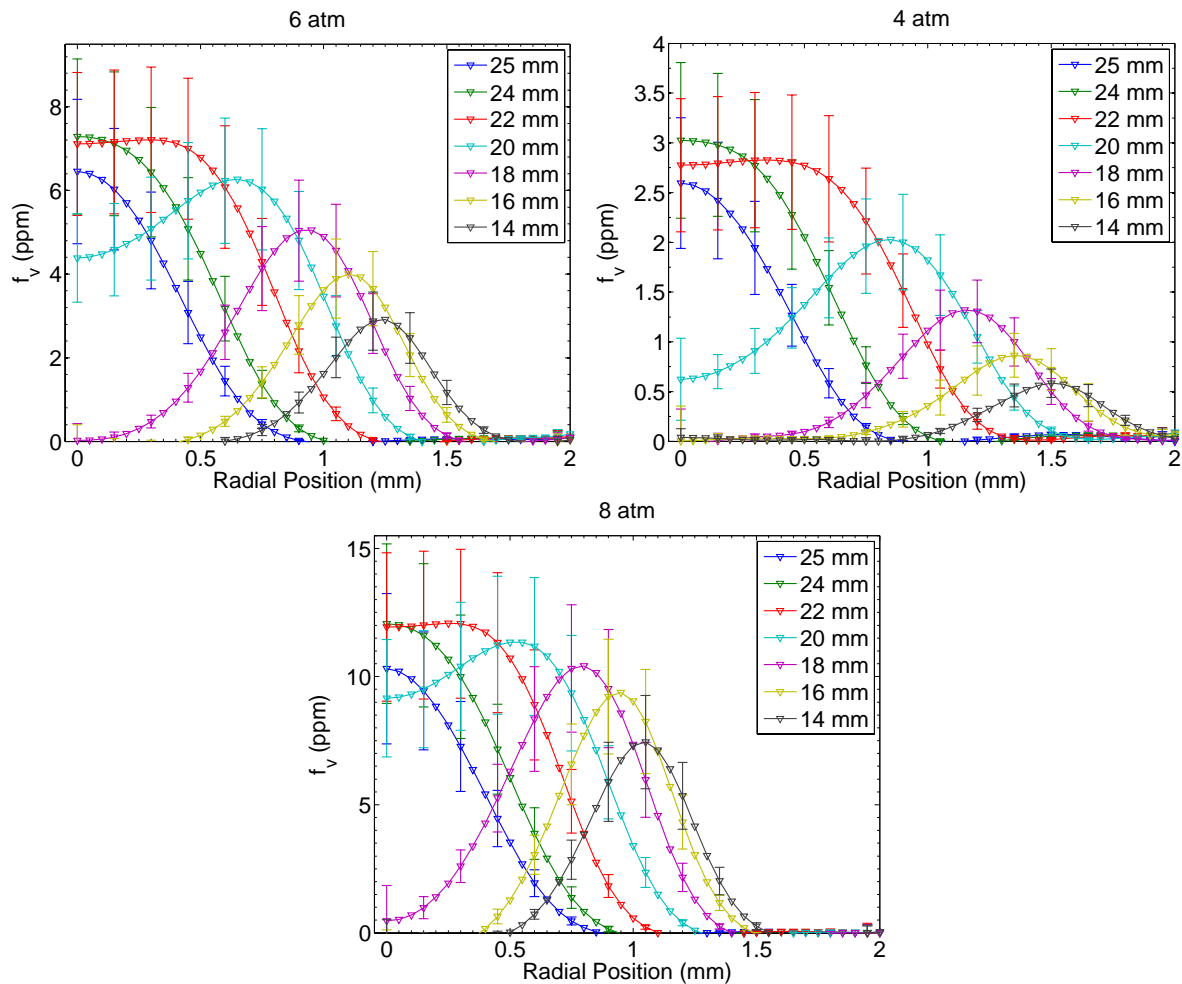


Figure 4.4.5: Local f_v profiles at 4, 6, and 8 atm

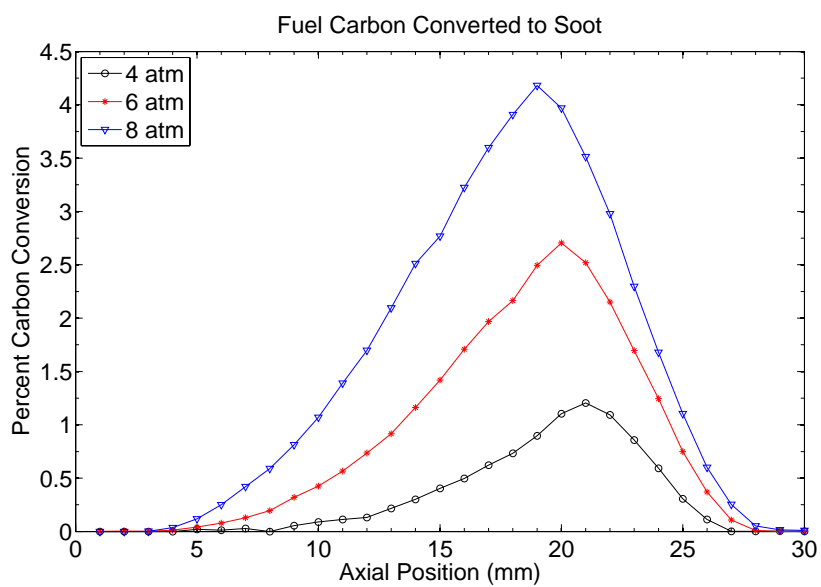


Figure 4.4.6: Percent of fuel carbon converted to soot

The peak carbon conversions are 1.2, 2.7, and 4.2% at 4, 6, and 8 atm, respectively. Fitting these values to a power law relationship, we find that peak conversion scales with pressure, $P^{1.8}$. Consider the difference in fuel mass flow rate, these results agree well with those of Joo and Gülder (2011). Joo and Gülder (2011) report a peak conversion of 1.5% at 10 atm with $\sim 1/5^{\text{th}}$ the fuel flow rate. Extrapolating our results to 10 atm, we calculate a conversion of 6.5%. Comparing those results and these, there appears to be a close to linear relationship between percent of carbon converted and fuel flow rate, though this will be further investigated. Joo and Gülder (2011) report the pressure dependence as $P^{1.36}$ in the range of 10-30 atm, though they have observed the reduction in the strength of this dependence as the critical pressure of the fuel mixture is reached, so stronger pressure dependence below 10 atm is reasonable.

4.4.2 Average Particle Diameter

To our knowledge, there are no reported results of scattering measurements in high-pressure laminar diffusion flames. Particle size measurements, of any kind, are lacking in flames under these conditions. Here we report the sixth-to-third moment ratio of the particle size probability function, D_{63} . Since this moment ratio is biased to larger diameters, we first report the raw vertically polarized differential scattering cross section (Q_{vv}) measured at 2, 4, 6, and 8 atm, shown in Fig. 4.4.7.

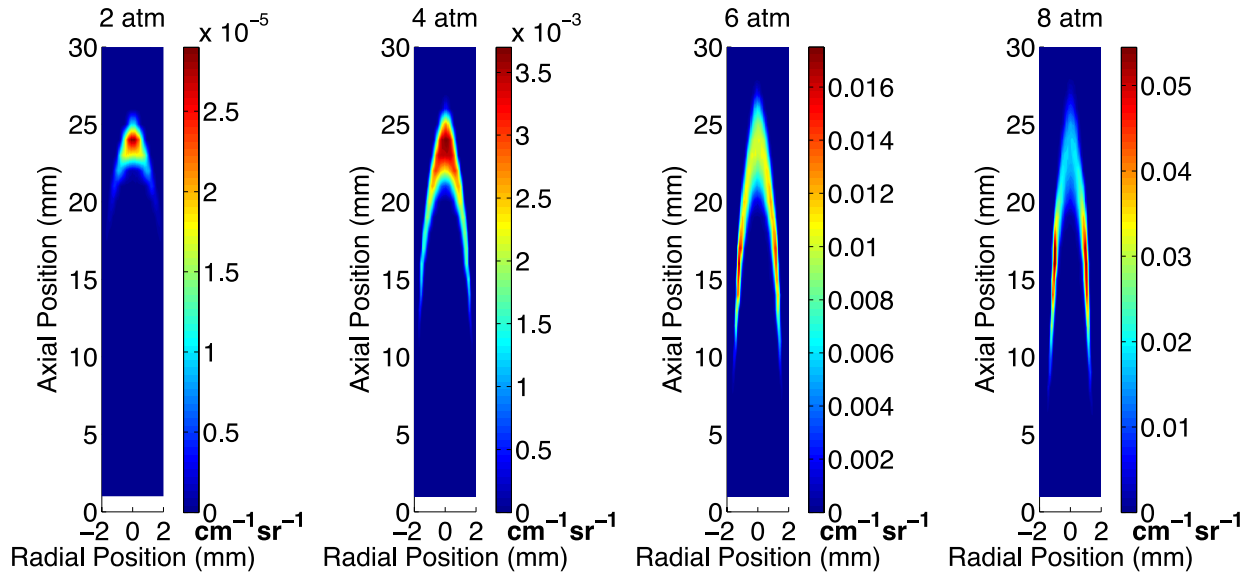


Figure 4.4.7: Q_{vv} contours at 2, 4, 6, and 8 atm

Although soot volume fraction cannot be resolved at 2 atm due to the low signal to noise ratio, scattering measurements have a large signal to noise ratio. Noting the difference in color scales between pressures in Fig. 4.4.7, we see that scattering intensity grows several orders of magnitude between 2 and 8 atm. We also see that the location of peak scattering intensity begins to shift away from the flame tip, and moves into the wings of the flame. This trend is similar to that in f_v , only it is much more pronounced here. Radial profiles of Q_{vv} are shown in Fig. 4.4.8 on a log scale.

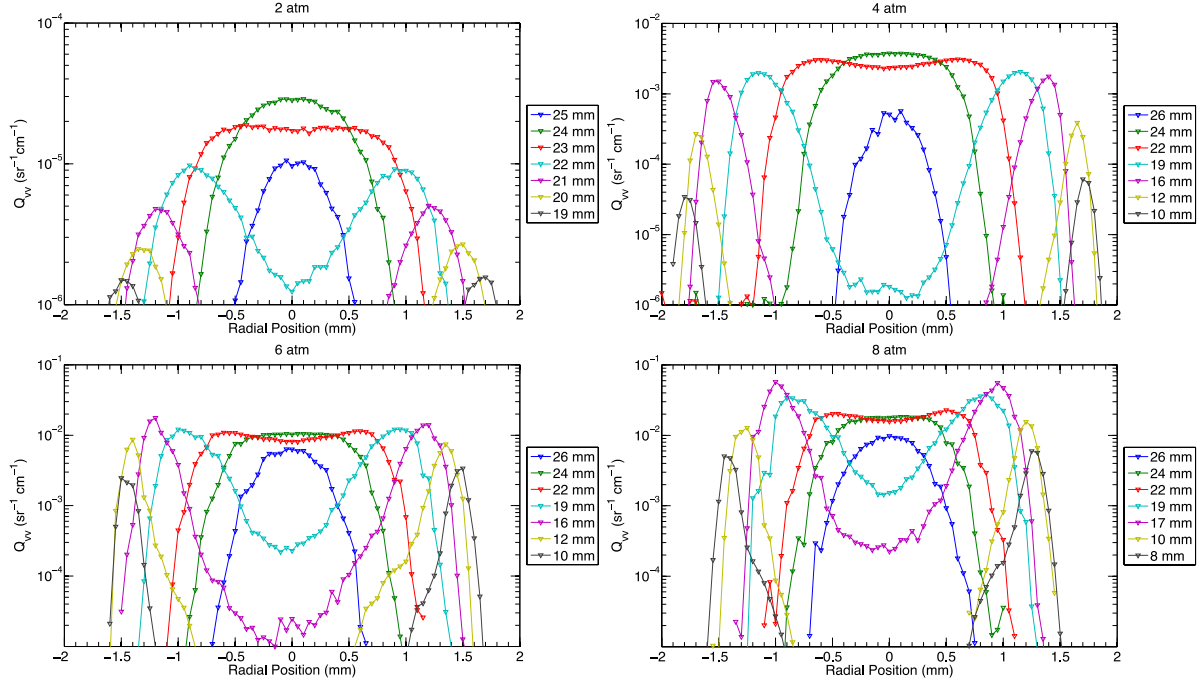


Figure 4.4.8: Q_{vv} profiles at 2, 4, 6, and 8 atm

Scattering measurements had high repeatability, and uncertainty in detectors was small enough that error bars were not necessary to include. From the figure we see that scattering intensity grows rapidly with increasing pressure, but grows much more rapidly in the annulus. Figure 4.4.9 shows radial profiles of D_{63} for 4, 6, and 8 atm.

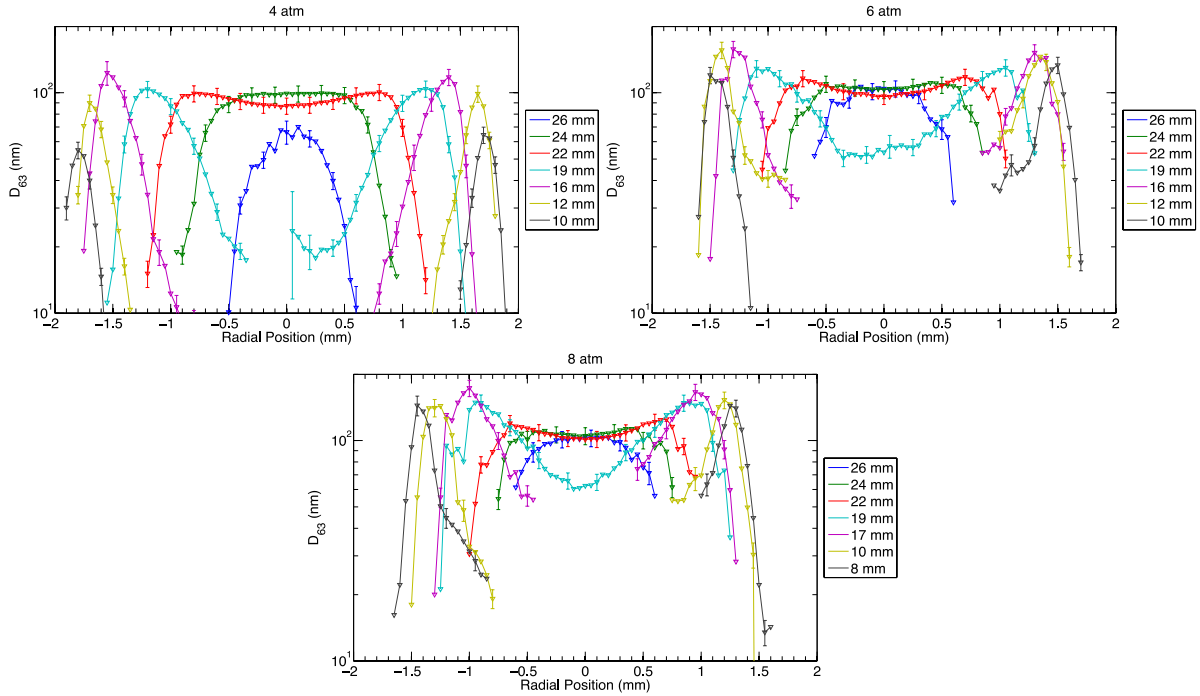


Figure 4.4.9: D_{63} profiles at 4, 6, and 8 atm

Although scattering measurements are possible at 2 atm, D_{63} cannot be calculated without f_v data. Error bars in this figure represents the combined uncertainty in detectors, f_v , and soot refractive index. Because of the strong scaling of Q_{vv} with particle diameter (D^6), relatively large uncertainties in Q_{vv} do not have a significant effect on calculated particle diameter. One thing to note is that D_{63} is representative of individual soot particles, not agglomerate sizes. We can see from the figure that particle diameters do not grow significantly near at the tip of the flame as pressure is increased. Particle diameters in the wings of the flame grow more rapidly. This trend is demonstrated more clearly in Fig. 4.4.10.

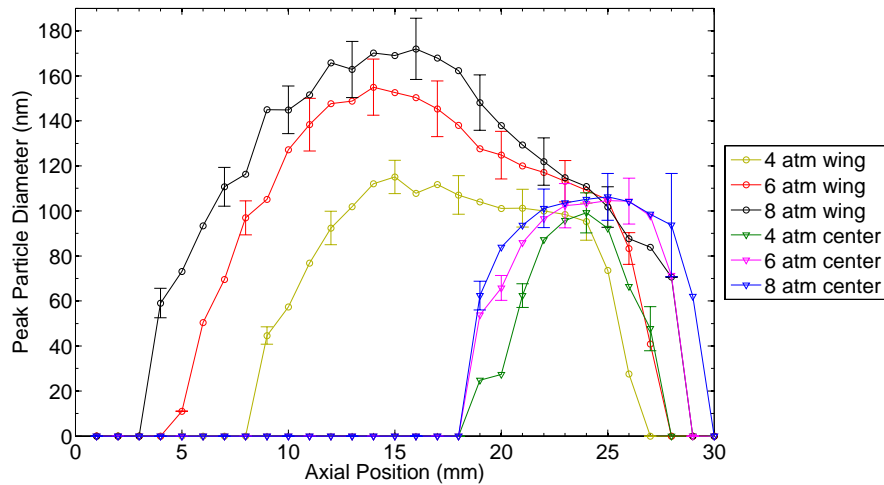


Figure 4.4.10: Peak average particle diameter (D_{63})

Figure 4.4.10 shows peak D_{63} as a function of axial flame height in one of two regimes: in the wings, and along the centerline. The boundary between these two is located approximately 1 mm from centerline. As seen from the “center” profiles, there is very little dependency on peak particle diameter along the centerline. Growth begins at around 18 mm height, and peaks near 25 mm. In the “wings” profiles, we see that with increasing pressure, growth begins lower in the flame, at about the same rate, but to much larger peak diameters. In fact, particles of the sizes observed in the wings at high pressure (160+ nm) may not be accurately described by the Raleigh approximation used in the analysis.

4.4.3 Number Density

Based on the exponential self-preserving assumption described earlier, number density of primary particles was calculated. The results for 4, 6, and 8 atm are shown in Fig. 4.4.11. A large number of primary particles exist far inside the flame front. As you look outward, a large number of particles conglomerate to form larger primary particles. In the flame, the particles are oxidized and break up into smaller particles again. These results are consistent with those of Santoro *et al.* (1983) for atmospheric conditions considering our soot volume fraction.

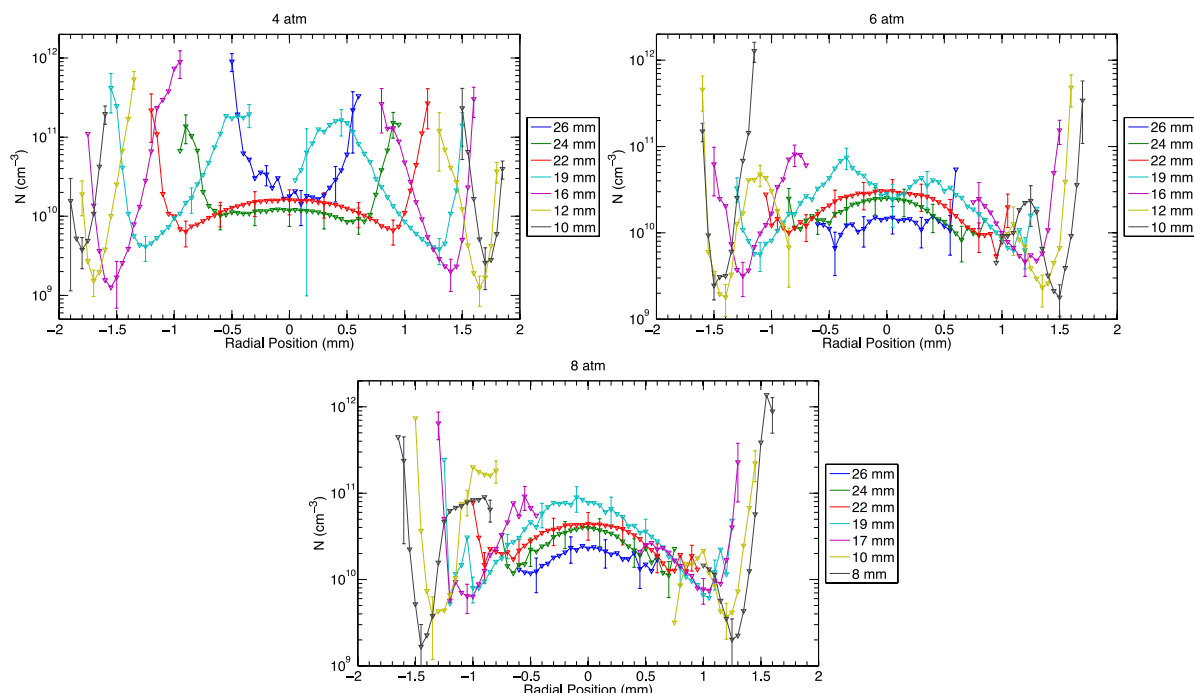


Figure 4.4.11: Number density of primary particles at 4, 6, and 8 atm

4.5 Results of Real Fuels

The custom electrospray will enable us to conduct further experiments with prevaporized liquid fuels. We are currently working to overcome the challenges associated with vaporizing heavy liquid fuels in high-pressure environments without coking.

5. Summary of Conclusions

5.1 Hydrocarbon Species Concentrations in Nitrogen-diluted Ethylene Flame

- 1) The visible flame height remains relatively constant at approximately 27 mm while pressure increases from 1 to 8 atmospheres. Furthermore, the cross-section area of the flame decreased linearly with pressure.
- 2) The concentrations of ethylene decrease faster along the axis of the flame from the base to tip with pressure, even though flame height does not change;
- 3) Peak concentrations of acetylene and propane are highest at 1 atmosphere, and decrease with pressure, indicating more efficient conversion to heavier compounds at higher pressures.
- 4) Concentrations of the various non-saturated C3 species increase with increase in pressure, suggesting larger concentrations of propargyl radicals at higher pressures resulting in increased benzene and PAH;
- 5) 1,3 butadiene concentrations increase 60% from 1 atmosphere to 8 atmospheres whereas the concentrations of diacetylene decrease 50% from 1 to 8 atm, with the profiles similar to acetylene. Therefore formation reactions involve acetylene as the parent molecule for diacetylene and are completely different to 1,3 butadiene formation reactions.

- 6) Peak concentrations of benzene and toluene increase with pressure, leading to higher soot yield;
- 7) Large quantities of non-fuel hydrocarbons in all the cases are present lower in the flame at higher pressures, due to an increase in transport of the measured species in the radial direction with increase in pressure.
- 8) Concentrations of the PAH also increase significantly with increase in pressure, with the peak concentrations moving closer to the base. PAH concentrations reach their peak concentrations at higher locations than the C2-C7 species for a given pressure.

5.2 Soot Precursor Formation and Temperature in Ethylene Flames with Different Diluents

- 1) The concentrations of ethylene increase first and then decrease with the helium-diluted flame as the helium flame is lifted at all the pressures measured, although the lift off height decreases with increasing pressure. Argon- and nitrogen-diluted flames show similar consumption rates of ethylene. Carbon dioxide enhances the consumption rate of ethylene at eight atmospheres due to the possible chemical reactions involving CO₂.
- 2) The soot suppressing qualities of carbon dioxide are greater than those of helium, which is evidenced by the levels of various soot precursors and flame luminosity. In the case of C₂H₂ and C₆H₆, two key soot precursors, helium-diluted flames have approximately 3 times the concentrations of C₆H₆ and 1.5 times the concentration of C₂H₂ when compared to the carbon dioxide-diluted flame at 8 atmospheres.
- 3) Helium and argon show marked differences in species concentration profiles even though both are mono-atomic inerts with differences in diffusivity between the two driving soot precursor formation mechanisms.
- 4) The effect of premixing in the lifted helium-diluted flame causes increased production of ethane, propane and 1-butene when compared to the other three diluents, due to the presence of oxygen radicals available for reactions.
- 5) At one atmosphere, the carbon dioxide-diluted flame is the coolest, with a peak temperature of 1760 K and the helium-diluted flame is the hottest, with a peak temperature of 2140K. Differences in heat capacities of the diluents drive the flame temperatures at one atmosphere.
- 6) The thermal effect of carbon dioxide is evident with lower flame temperatures, resulting in less soot precursors.
- 7) The levels of soot precursors produced in the diluted flames are attributed to the differences in the transport properties of the diluents, where the thermal diffusivities cause the temperature difference between the helium flame (hottest flame) and the carbon dioxide-diluted flame (coolest flame). Resulting in carbon dioxide flame being the better soot suppressant among the diluents tested.

5.3 Soot Surface Temperatures and Soot Volume Fractions in Ethylene Flames with Different Diluents with Two-color Pyrometry

- 1) Helium flame yields the highest soot surface temperatures, and carbon dioxide flame results in the lowest flame temperatures at all pressure ranges investigated. This result is consistent with flame temperature measurements made using thermocouples.
- 2) When comparing the peak soot volume fractions between argon and nitrogen, argon yields more soot than nitrogen, this corroborates results of soot precursor concentration measurements between the two diluents.

3) At low pressures peak soot volume fractions exist in the tip regions with all the diluents, but with the increase in pressure the peak soot volume fraction not only increases but also shifts to flame wings.

4) The flame temperature difference between the inerts could be attributed to their thermal diffusivities.

5) Carbon dioxide proves to be a superior soot suppressant among the four diluents tested by yielding the least soot volume fractions (~1ppm at 8 atmospheres).

5.4 Laser Extinction and Scattering Measurements

1) At lower pressures, peak soot volume fraction is at flame tip. With increasing pressure, the location of the peak moves towards the flame base and into the annulus. Peak integrated soot volume fraction scales with pressure as $P^{2.2}$.

2) As pressure increases, peak fuel carbon converted to soot increases with pressure as $P^{1.8}$, and the location of this peak moves closer to the flame base.

3) Peak average particle diameter is insensitive to pressure along the flame centerline.

4) Peak average particle diameter in the flame annulus increases with pressure, though to diameters not well described by Rayleigh theory.

5.5 Prevaporized Liquid Fuels

1) A custom electrospray prevaporizer has been built capable of prevaporizing multi-component liquid fuels at pressures up to 30 atm, work is ongoing.

Bibliography

- Abhinavam Kailasanathan, R. K., Book, E. K., Fang, T., Roberts, W. L., 'Hydrocarbon Species Concentrations in Nitrogen Diluted Ethylene-air Laminar Jet Diffusion Flames At Elevated Pressures,' Proceeding of the Combustion Institute, 34/11035-1043 (2013).
- Abhinavam Kailasanathan, R.K., Berry Yelverton, T.L., Fang, T. and Roberts, W.L. 'Effect of Diluents on Soot Precursor Formation and Temperature in Ethylene Laminar Diffusion Flames,' Combustion and Flame 160, 656–670 (2013).
- Agilent Technologies. Vapor volume calculations of common liquids and solvents.
- Acrivos, A. and Taylor, T.D. 'Heat and mass transfer from single spheres in stokes flow,' Physics of Fluids, 5(4):387-394, 1962.
- Bento, D.S., Thomson, K.A., Gulder, O.L., 'Soot formation and temperature fiel structure in laminar propane-air diffusion flames at elevated pressures,' Combust. Flame 145, 765-778 (2006).
- Boiarciuc, A., Foucher, F., Mounaim-Rousselle, C., 'Soot volume fractions and primary particle size estimate by means of the simultaneous two-color-time-resolved and 2D laser-induced incandescence,' Appl. Phys. B 83, 413-421 (2006).
- Bradley, D. and Entwistle, A.G., 'Measurement of high gas temperatures with fine wire thermocouples. Journal of mechanical engineering science,' 10(4):299-305, (1968).
- Castaldi, M.J., Marinov, N.M., Melius, C.F., Huang, J.M., Senkan, S.M., Pitz, W. J., and Westbrook, C.K., 'Experimental and modeling investigation of aromatic and polycyclic aromatic hydrocarbon formation in a premixed ethylene flame,' Proceeding of the Combustion Institute. 26 (1) 693–702 (1996).
- Chang, H. and Charalampopoulos, T.T., 'Determination of the wavelength dependence of refractive indices of flame soot,' Proc. R. Soc. Lond. 430, 577-591 (1990).
- Cignoli, F., DeIuliis, S., Manta, V., Zizak, G., 'Two-dimensional two-wavelength emission technique for soot diagnostics,' Applied Optics 40: 30, 5370-5378 (2001).
- D'Alessio, A., Beretta, F., Venitozzi, C., 'Optical investigations on soot forming methane-oxygen flames,' Combust. Sci. Tech. 5, 263 (1972).
- D'Anna, D. and Kent, J.H., 'Aromatic formation pathways in non-premixed methane flames,' Combustion and Flame, 132(4):715-722, 3 (2003).
- D'Anna, A., Kent, J.H., and Santoro, R.J. 'Investigation of species concentration and soot formation in a co-flowing diffusion flame of ethylene,' Combust. Sci. and Tech., 179: 355-369 (2007)
- Dalzell, W.H. and Sarofim, A.F., 'Optical constants of soot and their application to heat-flux calculations,' J. Heat Transfer 91, 100 (1969).
- DeIuliis, S., Barbini, S., Benecchi, F., Cignoli, F., Zizak, G., 'Determination of the soot volume fraction in an ethylene diffusion flame by multi-wavelength analysis of soot radiation,' Combust. Flame 115, 253-261 (1998).

- Dasch, C.J., 'One-dimensional tomography - a comparison of Abel, onion-peeling, and filtered backprojection methods,' *Applied Optics* 31 (10) 1146-1152 (1992).
- Drake, M.C., Correa, S.M., Pitz, R.W., Shyy, W., Fenimore, C.P., 'Superequilibrium and thermal nitric oxide formation in turbulent diffusion flames,' *Combust. Flame* 69, 347-365 (1987).
- Flower, W.L. and Bowman, C.T., 'Soot production in axisymmetric laminar diffusion flames at pressures from one to ten atmospheres,' *Proceeding of the Combustion Institute* 22/1115-1124 (1986).
- Frenklach, M., 'Reaction mechanism of soot formation in flames,' *Phys. Chem. Chem. Phys.* 4 2028-2037 (2002).
- Gordon, S., and McBride B., 'Computer Program for Calculation of Complex Chemical Equilibrium Compositions, Rocket Performance, Incident and Reflected Shocks, and Chapman-Jouguet Detonations (CET),' NASA SP-273, NASA Lewis Research Center, Cleveland, OH, March 1971.
- Guo, H., Liu, F., Smallwood, G.J., Gulder, O., 'A numerical investigation of thermal diffusion influence on soot formation in ethylene/air diffusion flames,' *Int. J. Comput. Fluid Dynam.* 18:2, 139-151 (2004).
- Guo, H., Liu, F., Smallwood, G.J., Gulder, O., 'A numerical study of the influence of transport properties of inert diluents on soot formation in a co-flow laminar ethylene/air diffusion flame,' *Proceeding of the Combustion Institute*, 29/2359-2365 (2002).
- Hamins, A., Gordon, A.S., Seshadri, K., Saito, K., 'The structure of coflowing, laminar C₂ hydrocarbon-air diffusion flames,' *Proceeding of the Combustion Institute* 21/1033-1045 (1988).
- Heidermann, T., Jander, H., Wagner, H.G., 'Soot particles in premixed C₂H₄-air flames at high pressures (P=30-70 bar),' *Phys. Chem. Chem. Phys.* 1, 3497-3502 (1999).
- Holman, J.P., Heat Transfer. McGraw-Hill, New York, 1983.
- Kadota, T., Hiroyasu, H., Farazandehmer, A., 'Soot formation by combustion of a fuel droplet in high pressure gaseous environments,' *Combust. Flame* 29, 67 (1977).
- Kennedy, I.M., Yam, C., Rapp, D.C., Santoro, R.J., 'Modeling and measurements of soot and species in laminar diffusion flames,' *Combust. Flame* 107, 368-382 (1996).
- Kim, C.H., El-Leathy, A.M., Xu, F., Faeth, G.M., 'Soot surface growth and oxidation in laminar diffusion flames at pressures of 0.1-1.0 atm,' *Combust. Flame* 136, 191-207 (2004).
- Kim, C.H., Xu, F., Faeth, G.M., 'Soot surface growth and oxidation at pressures up to 8.0 atm in laminar nonpremixed and partially premixed flames,' *Combust. Flame* 152, 301-316 (2008).
- Krishnan, S. S., K. C. Lin, and G. M. Faeth. 'Extinction and scattering of soot emitted from turbulent diffusion flames for wavelengths of 250-5200 nm,' 2000 National Heat Transfer Conference, Pittsburgh, PA. (2000).

- Li, Y., Applications of transient grating spectroscopy to determine temperature and transport properties measurements in high-pressure environments, Department of Mechanical and Aerospace Engineering, North Carolina State University, (2001).
- Manta, V., G. Zizak, F. Cignoli, S. De Iuliis, 'Two-dimensional two-wavelength emission technique for soot diagnostics,' *Applied Optics*, 40(30):5370–5378, (2001)
- McArragher, J.S. and Tan, K.J., 'Soot formation at high pressure: a literature review,' *Combust. Sci. Tech.* **5**, 257 (1972).
- McCrain, L.L. and Roberts, W.L., 'Soot volume fraction measurements in high pressure jet diffusion flames,' *Combust. Flame* 140, 60-69 (2005).
- McEnally, C.S., Koylu, U.O, Pfefferle, L.D., Rosner, D.E., 'Soot volume fraction and temperature measurements in laminar nonpremixed flames using thermocouples,' *Combustion and Flame*, 109(4):701-720, 6 (1997).
- McEnally, C.S. and Pfefferle, L.D., 'Comparison of non-fuel hydrocarbon concentrations measured in coflowing nonpremixed flames fueled with small hydrocarbons,' *Combust. Flame* 117, 362-372 (1999).
- McEnally, C.S., Pfefferle, L.D., Schaffer, A.M., Long, M.B., Mohammed, R.K., Smooke, M.D., Colket, M.B., 'Characterization of a coflowing methane/air non-premixed flame with computer modeling, Rayleigh-Raman imaging and on-line mass spectroscopy,' *Proceeding of the Combustion Institute*, 28/2063-2070 (2000).
- McEnally, C.S., Pfefferle, L.D., Atakan, B., Kohse-Hoinghaus, K. 'Studies of aromatic hydrocarbon formation mechanisms in flames: Progress towards closing the fuel gap,' *Prog. Energy Combust. Sci.* 32 (3) 247–294 (2006).
- McLintock, I.S., 'The effect of various diluents on soot production in laminar ethylene diffusion flames,' *Combust. Flame* 12, 217-225 (1968).
- Millberg, M.E., 'Carbon formation in an acetylene-air diffusion flame,' *J. Phys. Chem.* **63**, 578 (1959).
- Miller, I.M. and Maahs, H.G., 'High pressure flame system for pollution studies with results for methane-air diffusion flames,' *NASA Report No. TND-8407* (1977).
- Olten, N. and Senkan, S., 'Formation of polycyclic aromatic hydrocarbons in an atmospheric pressure ethylene diffusion flame,' *Combustion and Flame*, 118(3):500-507, 8 (1999).
- Quay, B., Lee, T-W., Ni, T., Santoro, R.J., 'Spatially resolved measurements of soot volume fraction using laser-induced incandescence,' *Combust. Flame* 97, 384-392 (1994).
- Rapp, D.C., 'Soot formation: species measurements and analysis in laminar co-annular diffusion flames,' *Penn. State Univ., Dissertation* (1996).
- Roper, F.G., Smith, C., Cunningham, A.C., 'Prediction of laminar jet diffusion flame sizes .2. Experimental-verification,' *Combust. Flame* 29 227–234 (1977).
- Santoro, R.J., Semerjian, H.G., Dobbins, R.A., 'Soot particle measurements in diffusion flames,' *Combust. Flame* 51 203-218 (1983).

- Santoro, R.J. and Semerjian, H.G. 'Soot Formation in Diffusion Flames: Flow Rate, Fuel Species, and Temperature Effects,' *Proceedings Combustion Institute* 20, 997–1006 (1984).
- Schalla, R.L. and McDonald, G.E., 'Mechanisms of soot formation in diffusion flames,' *Fifth Symposium (International) on Combustion*, The Combustion Institute, 316 (1955).
- Schug, K.P., Manheimer-Timnat, Y., Yaccarino, P., Glassman, I., 'Sooting behavior of gaseous hydrocarbon diffusion flames and the influence of additives,' *Combust. Sci. Tech.* 22, 235-250 (1980).
- Thomson, K.A., 'Soot Formation in Annular Non-Premixed Laminar Flames of Methane-Air of 0.1 to 4.0 MPa', PhD thesis, University of Waterloo, Waterloo, Ontario, Canada, 2004.
- Thomson, K.A., Ö.L. Gülder, E.J. Weckman, R.A. Fraser, G.J. Smallwood, D.R. Snelling, 'Soot concentration and temperature measurements in co-annular, nonpremixed CH₄/air laminar flames at pressures up to 4 MPa,' *Combust. Flame* 140 222-232 (2005).
- Wang, H., and Frenklach, M., 'A detailed kinetic modeling study of aromatics formation in laminar premixed acetylene and ethylene flames,' *Combust. Flame* 110 (1-2) 173–221 (1997).
- Zhang, J., W. Jing, W.L. Roberts, T. Fang, 'Soot Temperature and KL Factor for Biodiesel and Diesel Spray Combustion in a Constant Volume Combustion Chamber,' *Applied Energy*, vol. 107 52-65 (2013)
- Zhao, H. and Ladommatos, N., 'Optical diagnostics for soot and temperature measurement in diesel engines' *Progress in Energy and Combustion Science*, 24(3):221-255, (1998).